

1 LEVERAGING MULTI-MESSENGER ASTROPHYSICS FOR DARK MATTER SEARCHES

By

Daniel Nicholas Salazar-Gallegos

A DISSERTATION

Submitted to
Michigan State University
in partial fulfillment of the requirements
for the degree of

Physics—Doctor of Philosophy
Computational Mathematics in Science and Engineering—Dual Major

Today

ABSTRACT

3 I did Dark Matter with HAWC and IceCube. I also used Graph Neural Networks

⁴ Copyright by

⁵ DANIEL NICHOLAS SALAZAR-GALLEGOS

⁶ Today

ACKNOWLEDGMENTS

8 I love my friends. Thanks to everyone that helped me figure this out. Amazing thanks to the people
9 at LANL who supported me. Eames, etc Dinner Parties Jenny and her child Kaydince Kirsten, Pat,
10 Andrea Family. You're so far but so critical to my formation. Unconditional love. Roommate

TABLE OF CONTENTS

12	LIST OF TABLES	vii
13	LIST OF FIGURES	viii
14	LIST OF ABBREVIATIONS	xiv
15	CHAPTER 1 INTRODUCTION	1
16	CHAPTER 2 DARK MATTER IN THE COSMOS	2
17	2.1 Introduction	2
18	2.2 Dark Matter Basics	3
19	2.3 Evidence for Dark Matter	4
20	2.4 Searching for Dark Matter: Particle DM	11
21	2.5 Sources for Indirect Dark Matter Searches	16
22	2.6 Multi-Messenger Dark Matter	18
23	CHAPTER 3 MULTIMESSENGER ASTROPHYSICS: DETECTING HIGH EN-	
24	ERGY NEUTRAL MESSENGERS	21
25	3.1 Introduction	21
26	3.2 Charged Particles in a Medium	21
27	3.3 Photons (γ)	22
28	3.4 Neutrinos (ν)	22
29	3.5 Opportunities to Combine for Dark Matter	22
30	CHAPTER 4 HIGH ALTITUDE WATER CHERENKOV (HAWC) OBSERVATORY .	24
31	4.1 The Detector	24
32	4.2 Events Reconstruction and Data Acquisition	24
33	4.3 Remote Monitoring	24
34	CHAPTER 5 ICECUBE NEUTRINO OBSERVATORY	25
35	5.1 The Detector	25
36	5.2 Events Reconstruction and Data Acquisition	25
37	5.3 Northern Test Site	25
38	CHAPTER 6 GLORY DUCK: MULTI-WAVELENGTH SEARCH FOR DARK MATT-	
39	TER ANNIHILATION TOWARDS DWARF SPHEROIDAL GALAX-	
40	IES	26
41	6.1 Introduction	26
42	6.2 Dataset and Background	28
43	6.3 Analysis	29
44	6.4 Likelihood Methods	34
45	6.5 HAWC Results	40
46	6.6 Glory Duck Combined Results	43
47	6.7 HAWC Systematics	48

48	6.8 <i>J</i> -factor distributions	49
49	6.9 Discussion and Conclusions	55
50	CHAPTER 7 MULTITHREADING HAWC ANALYSES FOR DARK MATTER	
51	SEARCHES	59
52	7.1 Introduction	59
53	7.2 Dataset and Background	59
54	7.3 Analysis	60
55	7.4 Likelihood Methods	65
56	7.5 Computational Methods: Multithreading	65
57	CHAPTER 8 HEAVY DARK MATTER ANNIHILATION SEARCH WITH ICE-	
58	CUBE'S NORTH SKY TRACK DATA	67
59	CHAPTER 9 NU DUCK	68
60	APPENDIX A MULTI-EXPERIMENT SUPPLEMENTARY FIGURES	69
61	APPENDIX B MULTITHREADING SUPPLEMENTARY FIGURES	70
62	BIBLIOGRAPHY	71

LIST OF TABLES

<p>64 Table 6.1 Summary of the relevant properties of the dSphs used in the present work. 65 Column 1 lists the dSphs. Columns 2 and 3 present their heliocentric distance 66 and galactic coordinates, respectively. Columns 4 and 5 report the J-factors of 67 each source given from the \mathcal{GS} and \mathcal{B} independent studies and their estimated 68 $\pm 1\sigma$ uncertainties. The values $\log_{10} J$ (\mathcal{GS} set) [45] correspond to the mean 69 J-factor values for a source extension truncated at the outermost observed star. 70 The values $\log_{10} J$ (\mathcal{B} set) [47] are provided for a source extension at the tidal 71 radius of each dSph. Bolded sources are within HAWC's field of view and 72 provided to the Glory Duck analysis.</p> 34
<p>73 Table 6.2 Summary of dSph observations by each experiment used in this work. A 74 ‘-’ indicates the experiment did not observe the dSph for this study. For 75 Fermi-LAT, the exposure at 1 GeV is given. For HAWC, $\Delta\theta$ is the absolute 76 difference between the source declination and HAWC latitude. HAWC is more 77 sensitive to sources with smaller $\Delta\theta$. For IACTs, we show the zenith angle 78 range, the total exposure, the energy range, the angular radius θ of the signal or 79 ON region, the ratio of exposures between the background-control (OFF) and 80 signal (ON) regions (τ), and the significance of gamma-ray excess in standard 81 deviations, σ.</p> 35
<p>82 Table 7.1 Summary of the relevant properties of the dSphs used in the present work. 83 Column 1 lists the dSphs. Columns 2 and 3 present their heliocentric distance 84 and galactic coordinates, respectively. Column 4 reports the J-factors of each 85 source given from the \mathcal{LS} studies and estimated $\pm 1\sigma$ uncertainties. The 86 values $\log_{10} J$ (\mathcal{LS} set) [65] correspond to the mean J-factor values for a 87 source extension truncated at 0.5°.</p> 63
<p>88 Proof I know how to include</p>	

LIST OF FIGURES

90	Figure 2.1	Rotation curve fit to NGC 6503 from [7]. Dashed line is the contribution 91 from visible matter. Dotted curves are from gas. Dash-dot curves are from 92 dark matter (DM). Solid line is the composite contribution from all matter 93 and DM sources. Data are indicated with bold dots with error bars. Data 94 agree strongly with a matter + DM composite prediction.	5
95	Figure 2.2	Light from distant galaxy is bent in unique ways depending on the distribution 96 of mass between the galaxy and Earth. Yellow dashed lines indicate where 97 the light would have gone if the matter were not present [8].	7
98	Figure 2.3	(left) Optical image of galactic cluster 1E0657-558. (right) X-ray image of the 99 cluster with redder meaning hotter and higher baryon density. (both) Green 100 contours are reconstruction of gravity contours from weak lensing. White 101 rings are the best fit mass maxima at 68.3%, 95.5%, and 99.7% confidence. 102 The matter maxima of the clusters are clearly separated from x-ray maxima. [9]	8
103	Figure 2.4	Plank CMB sky. Sky map features small variations in temperature in primor- 104 dial light. These anisotropies are used to make inferences about the universe's 105 energy budget and developmental history. [10]	9
106	Figure 2.5	Observed Cosmic Microwave Background power spectrum as a function of 107 multipole moment from Plank [10]. Blue line is best fit model from Λ CDM. 108 Red points and lines are data and error, respectively.	10
109	Figure 2.6	Predicted power spectra of CMB for different $\Omega_m h^2$ values for fixed baryon 110 density from [11]. (left) Low $\Omega_m h^2$ increases the prominence of first and 111 second peaks. (middle) $\Omega_m h^2$ is most similar to the observed power spectrum. 112 The second and third peaks are similar in height. (right) $\Omega_m h^2$ is large which 113 suppresses the first peak and raises the prominence of the third peak.	10
114	Figure 2.7	The Standard Model (SM) of particle physics. Figure taken from http://www.quantumdiaries.org/2014/03/14/the-standard-model-a-beautiful-but-flawed-theory/	12
117	Figure 2.8	Simplified Feynman diagram demonstrating with different ways DM can 118 interact with SM particles. The 'X's refer to the DM particles whereas the 119 SM refer to fundamental particles in the SM. The large circle in the center 120 indicates the vertex of interaction and is purposely left vague. The colored 121 arrows refer to different directions of time as well as their respective labels. 122 The arrows indicate the initial and final state of the DM -SM interaction in time.	13

123	Figure 2.9 A single jet event in ATLAS detector from 2017 [16]. Jet momentum was 124 observed to be 1.9 TeV. Missing transverse momentum was observed to be 125 1.9 TeV compared to the initial transverse momentum of the event was 0. 126 Implied MET is traced by a red dashed line in event display.	14
127	Figure 2.10 More detailed pseudo-Feynman diagram of particle cascade from dark matter 128 annihilation into 2 quarks. The quarks hadronize and down to stable particles 129 like γ or the anti-proton (p^-). Diagram pulled from ICRC 2021 presentation 130 on DM annihilation search [17].	15
131	Figure 2.11 Dark Matter (DM) decay spectrum for $b\bar{b}$ initial state and γ final state. Redder 132 spectra are for larger DM masses. Bluer spectra are light DM masses. x is a 133 unitless factor defined as the ratio of the mass of DM, m_χ , and the final state 134 particle energy E_γ . Figure from [19].	17
135	Figure 2.12 Different dark matter density profiles compared. Some models produce ex- 136 ceptionally large densities at small r [20].	18
137	Figure 2.13 The Milky Way Galaxy in photons (γ) and neutrinos (ν) [22]. The Galactic 138 center is at $l=0^\circ$ and is the brightest region in all panels. (top) An Optical 139 color image of the Milky Way galaxy seen from Earth. Clouds of gas and dust 140 obscure some light from stars. (2nd down) Integrated flux of γ -rays observed 141 by the Fermi-LAT telescope [23]. (middle) Expected neutrino emission 142 that corresponds with Fermi-LAT observations. (2nd up) Expected neutrino 143 emission profile after considering detector systematics of IceCube. (bottom) 144 Observed neutrino emission from region of the galactic plane. Substantial 145 neutrino emission was detected.	19
146	Figure 2.14 Dark Matter annihilation spectra for different final state particle and standard 147 model annihilation channels [24]. Photons (red), e^\pm (green), \bar{p} (blue), ν (black).	20
148	Figure 3.1 TODO: Show a nuclear reactor with cherenkov radiation[NEEDS A SOURCE][FACT 149 CHECK THIS]	22
150	Figure 3.2 TODO: absorption spectrum of liquid and solid water[NEEDS A SOURCE][FACT 151 CHECK THIS]	23

152	Figure 6.1	Sensitivities of five gamma-ray experiments compared to percentages of the Crab nebula's emission and dark matter annihilation. Solid lines present estimated sensitivities to power law spectra [FACT CHECK THIS]for each experiment. Green lines are Fermi-LAT sensitivities where lighter green is the sensitivity to the galactic center and dark green is its sensitivity to higher declinations. Orange, red, and purple solid lines represent the MAGIC, HESS, and VERITAS 50 hour sensitivities respectively. The maroon and brown lines are the HAWC 1 year and 5 year sensitivities. Across four decades of gamma- ray energy, these experiments have similar sensitivities on the order 10^{-12} $\text{erg cm}^{-2}\text{s}^{-1}$. The dotted lines are estimated dark matter fluxes assuming $m_\chi = 5 \text{ TeV}$ DM annihilating to bottom quarks (red), tau leptons (blue), and W bosons (green). Faded gray lines outline percentage flux of the Crab nebula. Figure is an augmented version of [25]	27
165	Figure 6.2	Effect of Electroweak (EW) corrections on expected DM annihilation spec- trum for $\chi\chi \rightarrow W^-W^+$. Solid lines are spectral models that consider EW corrections. Dash-dot lines are spectral models without EW corrections. Red lines are models for $M_\chi = 1 \text{ TeV}$. Blue lines represent models for $M_\chi = 100$ TeV. All models are sourced from the PPPC4DMID [44].	31
170	Figure 6.3	$\frac{dJ}{d\Omega}$ maps for Segue1 (top) and Coma Berenices (bottom). Origin is centered on the specific dwarf spheroidal galaxies (dSph). X and Y axes are the angular separation from the center of the dwarf. Plots of the remaining 11 dSph HAWC studied are linked in Fig. A.1.	33
174	Figure 6.4	Illustration of the combination technique showing a comparison between $-2 \ln \lambda$ provided by four instruments (colored lines) from the observation of the same dSph without any J nuisance and their sum, <i>i.e.</i> the resulting combined likelihood (thin black line). According to the test statistics of Equation (6.6), the intersection of the likelihood profiles with the line $-2 \ln \lambda$ $= 2.71$ indicates the 95% C.L. upper limit on $\langle \sigma v \rangle$. The combined likelihood (thin black line) shows a smaller value of upper limit on $\langle \sigma v \rangle$ than those derived by individual instruments. We also show how the uncertainties on the J factor effects the combined likelihood and degrade the upper limit on $\langle \sigma v \rangle$ (thick black line). All likelihood profiles are normalized so that the global minimum $\widehat{\langle \sigma v \rangle}$ is 0. We note that each profile depends on the observational conditions in which a target object was observed. The sensitivity of a given instrument can be degraded and the upper limits less constraining if the observations are performed in non-optimal conditions such as a high zenith angle or a short exposure time.	38
189	Figure 6.5	HAWC upper limits at 95% confidence level on $\langle \sigma v \rangle$ versus DM mass for seven annihilation channels, using the set of J -factors from Ref. [53] The solid line represents the observed combined limit. Dashed lines represent limits from individual dSphs.	41

193	Figure 6.6 HAWC TS values for best fit $\langle\sigma v\rangle$ versus m_χ for seven SM annihilation channels with J factors from \mathcal{GS} . The solid black line shows the combined best fit TS values. The colored, dashed lines are the TS values for each of the 13 sources HAWC studied.	42
197	Figure 6.7 HAWC Brazil bands at 95% confidence level on $\langle\sigma v\rangle$ versus DM mass for seven annihilation channels with J -factors from \mathcal{GS} [53]. The solid line represents the combined limit from 13 dSphs. The dashed line is the expected limit. The green band is the 68% containment. The yellow band is the 95% containment.	43
202	Figure 6.8 Upper limits at 95% confidence level on $\langle\sigma v\rangle$ in function of the DM mass for eight annihilation channels, using the set of J factors from Ref. [53] (\mathcal{GS} set in Table 6.1). The black solid line represents the observed combined limit, the black dashed line is the median of the null hypothesis corresponding to the expected limit, while the green and yellow bands show the 68% and 95% containment bands. Combined upper limits for each individual detector are also indicated as solid, colored lines. The value of the thermal relic cross-section in function of the DM mass is given as the red dotted-dashed line [54].	44
211	Figure 6.9 Same as Fig. 6.8, using the set of J factors from Ref. [47, 55] (\mathcal{B} set in Table 6.1).	45
212	Figure 6.10 Comparisons of the combined limits at 95% confidence level for each of the eight annihilation channels when using the J factors from Ref. [53] (\mathcal{GS} set in Table 6.1), plain lines, and the J factor from Ref. [47, 55] (\mathcal{B} set in Table 6.1), dashed lines. The cross-section given by the thermal relic is also indicated [54].	47
216	Figure 6.11 Comparisons of the combined limits at 95% confidence level for a point source analysis and extended source using [53] \mathcal{GS} J-factor distributions and PPPC [44] annihilation spectra. Shown are the limits for Segue1 which will have the most significant impact on the combined limit. 6 of the 7 DM annihilation channels are shown. Solid lines are extended source studies. Dashed lines are point source studies. Overall, the extended source analysis improves the limit by a factor of 2.	49
223	Figure 6.12 Same as Fig. 6.11 on Coma Berenices. This dSph also contributes significantly to the limit. The limits are identical in this case.	50
225	Figure 6.13 Comparison of combined limits when correcting for HAWC's pointing systematic. All DM annihilation channels are shown. The solid black line is the ratio between published limit to the declination corrected limit. The blue solid line or "Combined_og" represented the limits computed for Glory Duck. The solid orange line or "Combined_ad" represented the limits computed after correcting for the pointing systematic.	51

231	Figure 6.14 Differential map of dJ/Ω from model built in Section 6.8.1 and profiles 232 provided directly from authors. (Top) Differential from Segue1. (bottom) 233 Differential from Coma Berenices. Note that their scales are not the same. 234 Segue1 shows the deepest discrepancies which is congruent with its large 235 uncertainties. Both models show anuli where unique models become apparent.	52
236	Figure 6.15 HAWC limits for Coma Berenices (top) and Segue1 (bottom) for two different 237 map sets. Blue lines are limits calculated on maps with poor model repre- 238 sentation. Orange lines are limits calculated on spatial profiles provided by 239 the authors of [45]. Black line is the ratio of the poor spatial model limits to 240 the corrected spatial models. The left y-axis measures $\langle\sigma v\rangle$ for the blue and 241 orange lines. The right y-axis measures the ratio and is unitless.	53
242	Figure 6.16 Comparisons between the J -factors versus the angular radius for the com- 243 putation of J factors from Ref. [53] (\mathcal{GS} set in Table 6.1) in blue and for 244 the computation from Ref. [47, 55] (\mathcal{B} set in Tab. 6.1) in orange. The solid 245 lines represent the central value of the J -factors while the shaded regions 246 correspond to the 1σ standard deviation.	56
247	Figure 6.17 Comparisons between the J -factors versus the angular radius for the com- 248 putation of J factors from Ref. [53] (\mathcal{GS} set in Tab. 6.1) in blue and for the 249 computation from Ref. [47, 55] (\mathcal{B} set in Tab. 6.1) in orange. The solid 250 lines represent the central value of the J -factors while the shaded regions 251 correspond to the 1σ standard deviation.	57
252	Figure 7.1 Difference between spectral hypotheses from PPPC [44] and HDM [64]. 253 Shown is the expected DM annihilation spectrum for $\chi\chi \rightarrow W^-W^+$. Solid 254 lines are spectral models with EW corrections from the PPPC. Dash-dot lines 255 are spectral models from HDM. Red lines are models for $M_\chi = 1$ TeV. Blue 256 lines represent models for $M_\chi = 100$ TeV.	62
257	Figure 7.2 Photon spectra for $\chi\chi \rightarrow \gamma\gamma$ (left) and $\chi\chi \rightarrow ZZ$ (right) after gaussian 258 convolution of line features. Both spectra have δ -features at photon energies 259 equal to the DM mass. Bluer lines are annihilation spectra with lower DM 260 mass. Redder lines are spectra from larger DM mass. All Spectral models are 261 sourced from the Heavy Dark Matter models [64]. Axes are drawn roughly 262 according to the energy sensitivity of HAWC.	63
263	Figure 7.3 $\frac{dJ}{d\Omega}$ maps for Coma Berenices, Draco, Segue1, and Sextans. Columns are 264 divided for the $\pm 1\sigma$ uncertainties in $dJ/d\Omega$ around the mean value from \mathcal{LS} 265 [65]. Origin is centered on the specific dwarf spheroidal galaxies (dSph). θ 266 and ϕ axes are the angular separation from the center of the dwarf	64

267	Figure 7.4 Infographic on how jobs and DM computation was organized in Section 6.3. Jobs were built for each permutation of CHANS and SOURCES shown by the left block in the figure. Each job, which took on the order 2 hrs to compute, had the following work flow: 1. Import HAWC analysis software, 2 min to run. 2. Load HAWC count maps, 5 min to run. 3. Load HAWC energy and spatial resolutions, 4 min. 5. Load DM spatial source templates and spectral models, less than 1 s. 6. Perform likelihood fit on data and model, about 8 min per DM mass. 7. Write results to file, less than 1s.	66
275	Figure A.1 Sister figure to Figure 6.3. Sources in the first row from left to right: Bootes I, Canes Venatici I, II. In second row: Draco, Hercules, Leo I. In the first row: Leo II, Leo IV, Sextans. In the final row: Ursa Major I, Ursa Major II.	69
278	Figure B.1 Sister figure to Figure 7.2 for remaining SM primary annihilation channels studied for this thesis. These did not require any post generation smoothing and so are directly pulled from [64] with a binning scheme most helpful for a HAWC analysis.	70

LIST OF ABBREVIATIONS

- 283 **MSU** Michigan State University
284 **LANL** Los Alamos National Laboratory
285 **DM** Dark Matter
286 **SM** Standard Model
287 **HAWC** High Altitude Water Cherenkov Observatory

288

CHAPTER 1

INTRODUCTION

289 Is the text not rendering right? Ah ok it knows im basically drafting the doc still

CHAPTER 2

290

DARK MATTER IN THE COSMOS

291 **2.1 Introduction**

292 The dark matter problem can be summarized in part by the following thought experiment.

293 Let us say you are the teacher for an elementary school classroom. You take them on a field
294 trip to your local science museum and among the exhibits is one for mass and weight. The exhibit
295 has a gigantic scale, and you come up with a fun problem for your class.

296 You ask your class, "What is the total weight of the classroom? Give your best estimation to
297 me in 30 minutes, and then we'll check your guess on the scale. If your guess is within 10% of the
298 right answer, we will stop for ice cream on the way back."

299 The students are ecstatic to hear this, and they get to work. The solution is some variation of
300 the following strategy. The students should give each other their weight or best guess if they do
301 not know. Then, all they must do is add each student's weight and get a grand total for the class.
302 The measurement on the giant scale should show the true weight of the class. When comparing
303 the measured weight to your estimation, multiply the measurement by 1.0 ± 0.1 to get the $\pm 10\%$
304 tolerances for your estimation.

305 Two of your students, Sandra and Mario, return to you with a solution.

306 They say, "We weren't sure of everyone's weight. We used 65 lbs. for the people we didn't
307 know and added everyone who does know. There are 30 of us, and we got 2,000 lbs.! That's a ton!"

308 You estimated 1,900 lbs. assuming the average weight of a student in your class was 60 lbs.
309 So, you are pleased with Sandra's and Mario's answer. You instruct your students to all gather on
310 the giant scale and read off the weight together. To all your surprise, the scale reads *10,000 lbs.*!
311 10,000 is significantly more than a 10% error from 2,000. In fact, it is approximately 5 times more
312 massive than either your or your students' estimates. You think to yourself and conclude there
313 must be something wrong with the scale. You ask an employee to check the scale and verify it is
314 well calibrated. They confirm that the scale is in working order. You weigh a couple of students
315 individually to assess that the scale is well calibrated. Sandra weighs 59 lbs., and Mario weighs

316 62 lbs., typical weights for their age. You then weigh each student individually and see that their
317 weights individually do not deviate greatly from 60 lbs. So, where does all the extra weight come
318 from?

319 This thought experiment serves as an analogy to the Dark Matter problem. The important
320 substitution to make however is to replace the students with stars and the classroom with a galaxy,
321 say the Milky Way. Individually the mass of stars is well measured and defined with the Sun as our
322 nearest test case. However, when we set out to measure the mass of a collection of stars as large as
323 galaxies, our well-motivated estimation is wildly incorrect. There simply is no way to account for
324 this discrepancy except without some unseen, or dark, contribution to mass and matter in galaxies.
325 I set out in my thesis to narrow the possibilities of what this Dark Matter could be.

326 This chapter is organized like the following... **TODO: Text should look like ... Chapter x has**
327 **blah blah blah.**

328 **2.2 Dark Matter Basics**

329 Presently, a more compelling theory of cosmology that includes Dark Matter (DM) in order
330 to explain a variety of observations is Λ Cold Dark Matter, or Λ CDM. I present the evidence
331 supporting Λ CDM in Section 2.3 yet discuss the conclusions of the Λ CDM model here. According
332 to Λ CDM fit to observations on the Cosmic Microwave Background (CMB), DM is 26.8% of the
333 universe's current energy budget. Baryonic matter, stuff like atoms, gas, and stars, contributes to
334 4.9% of the universe's current energy budget [1, 2, 3].

335 DM is dark; it does not interact readily with light at any wavelength. DM also does not interact
336 noticeably with the other standard model forces (Strong and Weak) at a rate that is readily observed
337 [3]. DM is cold, which is to say that the average velocity of DM is below relativistic speeds [1].
338 'Hot' DM would not likely manifest the dense structures we observe like galaxies, and instead
339 would produce much more diffuse galaxies than what is observed [3, 1]. DM is old; it played a
340 critical role in the formation of the universe and the structures within it [1, 2].

341 Observations of DM have so far been only gravitational. The parameter space available to what
342 DM could be therefore is extremely broad. The broad DM parameter space is iteratively tested in

343 DM searches by supposing a hypothesis that has not yet been ruled out and performing observations
344 to test them. When the observations yield a null result, the parameter space is constrained further.
345 I present some approaches for DM searches in Section 2.4.

346 **2.3 Evidence for Dark Matter**

347 Dark Matter (DM) has been a looming problem in physics for almost 100 years. Anomalies
348 have been observed by astrophysicists in galactic dynamics as early as 1933 when Fritz Zwicky
349 noticed unusually large velocity dispersion in the Coma cluster. Zwicky's measurement was the
350 first recorded to use the Virial theorem to measure the mass fraction of visible and invisible matter
351 in celestial bodies [4]. From Zwicky in [5], "*If this would be confirmed, we would get the surprising*
352 *result that dark matter is present in much greater amount than luminous matter.*" Zwicky's and
353 others' observation did not instigate a crisis in astrophysics because the measurements did not
354 entirely conflict with their understanding of galaxies [4]. In 1978, Rubin, Ford, and Norbert
355 measured rotation curves for ten spiral galaxies [6]. Rubin et al.'s 1978 publication presented a
356 major challenge to the conventional understanding of galaxies that could no longer be dismissed by
357 measurement uncertainties. Evidence has been mounting ever since for this exotic form of matter.
358 The following subsections provide three compelling pieces of evidence in support of the existence
359 of DM.

360 **2.3.1 First Clues: Stellar Velocities**

361 Zwicky, and later Rubin, measured the stellar velocities of various galaxies to estimate their
362 virial mass. The Virial Theorem upon which these observations are interpreted is written as

$$2T + V = 0. \quad (2.1)$$

363 Where T is the kinetic energy and V is the potential energy in a self-gravitating system. The
364 classical Newton's law of gravity from stars and gas was used for gravitational potential modeled in
365 the observed galaxies:

$$V = -\frac{1}{2} \sum_i \sum_{j \neq i} \frac{m_i m_j}{r_{ij}}. \quad (2.2)$$

366 Zwicky et al. measured just the velocities of stars apparent in optical wavelengths [5]. Rubin et al.
 367 added by measuring the velocity of the hydrogen gas via the 21 cm emission line of Hydrogen [6].
 368 The velocities of the stars and gas are used to infer the total mass of galaxies and galaxy clusters
 369 via Equation (2.1). An inferred mass is obtained from the luminosity of the selected sources. The
 370 two inferences are compared to each other as a luminosity to mass ratio which typically yielded [1]

$$\frac{M}{L} \sim 400 \frac{M_{\odot}}{L_{\odot}} \quad (2.3)$$

371 M_{\odot} and L_{\odot} referring to stellar mass and stellar luminosity, respectively. These ratios clearly indicate
 372 a discrepancy in apparent light and mass from stars and gas and their velocities.

373 Rubin et al. [6] demonstrated that the discrepancy was unlikely to be an underestimation of
 374 the mass of the stars and gas. The inferred "dark" mass was up to 5 times more than the luminous
 375 mass. This dark mass also needed to extend well beyond the extent of the luminous matter.

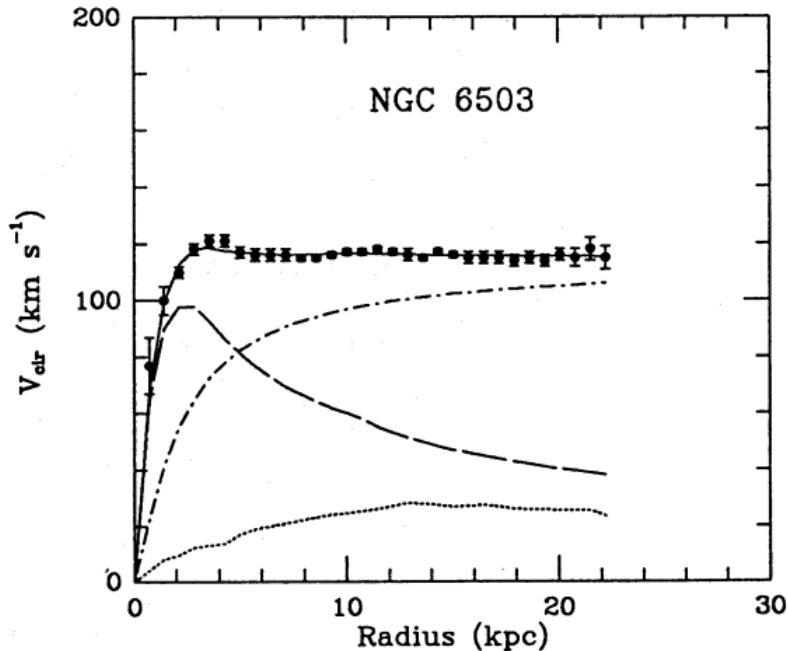


Figure 2.1 Rotation curve fit to NGC 6503 from [7]. Dashed line is the contribution from visible matter. Dotted curves are from gas. Dash-dot curves are from dark matter (DM). Solid line is the composite contribution from all matter and DM sources. Data are indicated with bold dots with error bars. Data agree strongly with a matter + DM composite prediction.

376 Figure 2.1 features one of many rotation curves plotted from the stellar velocities within galaxies.

377 The measured rotation curves mostly feature a flattening of velocities at higher radius which is not
378 expected if the gravity was only coming from gas and luminous matter. The extension of the
379 flat velocity region also indicates that the DM is distributed far from the center of the galaxy.
380 Modern velocity measurements include significantly larger objects, galactic clusters, and smaller
381 objects, dwarf galaxies. Yet, measurements along this regime are leveraging the Virial theorem
382 with Newtonian potential energies. We know Newtonian gravity is not a comprehensive description
383 of gravity. New observational techniques have been developed since 1978, and those are discussed
384 in the following sections.

385 **2.3.2 Evidence for Dark Matter: Gravitational Lensing**

386 Modern evidence for dark matter comes from new avenues beyond stellar velocities. Grav-
387 itational lensing from DM is a new channel from general relativity. General relativity predicts
388 aberrations in light caused by massive objects. In recent decades we have been able to measure the
389 lensing effects from compact objects and DM halos. Figure 2.2 shows how different massive ob-
390 jects change the final image of a faraway galaxy resulting from gravitational lensing. Gravitational
391 lensing developed our understanding of dark matter in two important ways.

392 Gravitational lensing provides additional compelling evidence for DM. The observation of two
393 merging galactic clusters in 2006, shown in Figure 2.3, provided a compelling argument for DM
394 outside the Standard Model. These clusters merged recently in astrophysical time scales. Galaxies
395 and star cluster have mostly passed by each other as the likelihood of their collision is low. Therefore,
396 these massive objects will mostly track the highest mass, dark and/or baryonic, density. Yet, the
397 intergalactic gas is responsible for the majority of the baryonic mass in the systems [4]. These gas
398 bodies will not phase through and will heat up as they collide together. The hot gas is located via
399 x-ray emission from the cluster. Two observations of the clusters were performed independently of
400 each other.

401 The first was the lensing of light around the galaxies due to their gravitational influences.
402 When celestial bodies are large enough, the gravity they exert bends space and time itself. The
403 warped space-time lenses light and will deflect in an analogous way to how glass lenses will bend

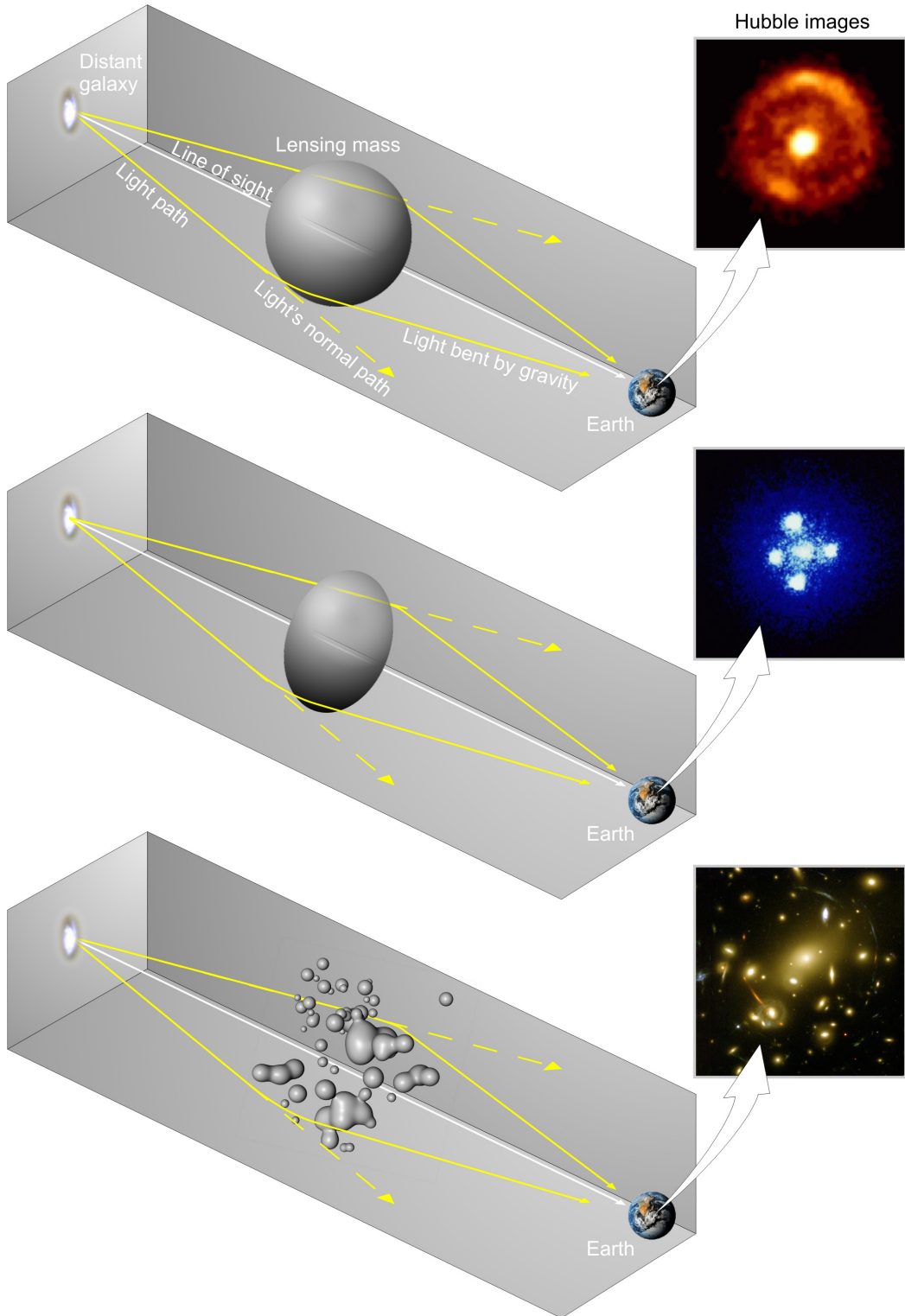


Figure 2.2 Light from distant galaxy is bent in unique ways depending on the distribution of mass between the galaxy and Earth. Yellow dashed lines indicate where the light would have gone if the matter were not present [8].

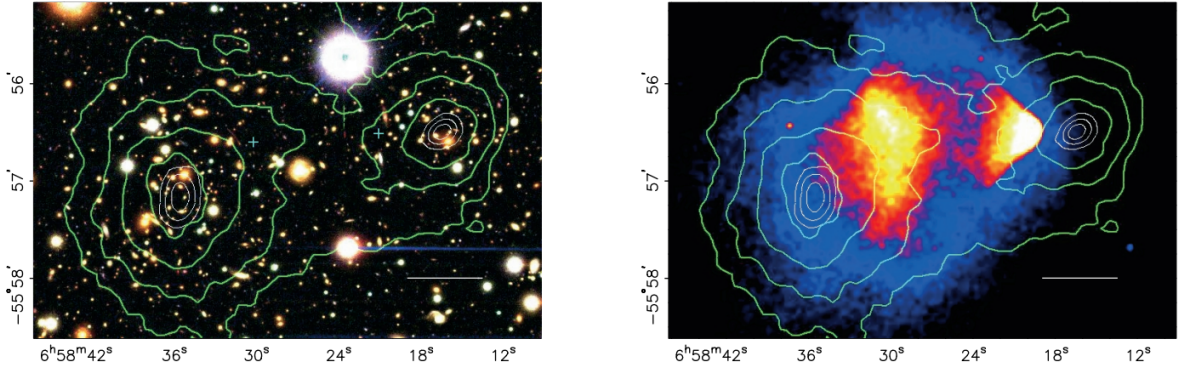


Figure 2.3 (left) Optical image of galactic cluster 1E0657-558. (right) X-ray image of the cluster with redder meaning hotter and higher baryon density. (both) Green contours are reconstruction of gravity contours from weak lensing. White rings are the best fit mass maxima at 68.3%, 95.5%, and 99.7% confidence. The matter maxima of the clusters are clearly separated from x-ray maxima. [9]

404 light, see Figure 2.2. With a sufficient understanding of light sources behind a massive object, we
 405 can reconstruct the contours of the gravitational lenses. The gradient of the contours shown in
 406 Figure 2.3 then indicates how dense the matter is and where it is.

407 The x-ray emission can then be observed from the clusters. Since these galaxies are mostly gas
 408 and are merging, then the gas should be getting hotter. If they are merging, the x-ray emissions
 409 should be the strongest where the gas is mostly moving through each other. Hence, X-ray emission
 410 maps out where the gas is in the merging galaxy cluster.

411 The lensing and x-ray observations were done on the Bullet cluster featured on Figure 2.3.
 412 The x-ray emissions do not align with the gravitational contours from lensing. The incongruence
 413 in mass density and baryon density suggests that there is a lot of matter somewhere that does
 414 not interact with light. Moreover, this dark matter cannot be baryonic [9]. The Bullet Cluster
 415 measurement did not really tell us what DM is exactly, but it did give the clue that DM also does
 416 not interact with itself very strongly. If DM did interact strongly with itself, then it would have been
 417 more aligned with the x-ray emission [9]. There have been follow-up studies of galaxy clusters with
 418 similar results. The Bullet Cluster and others like it provide a persuasive case against something
 419 possibly amiss in our gravitational theories.

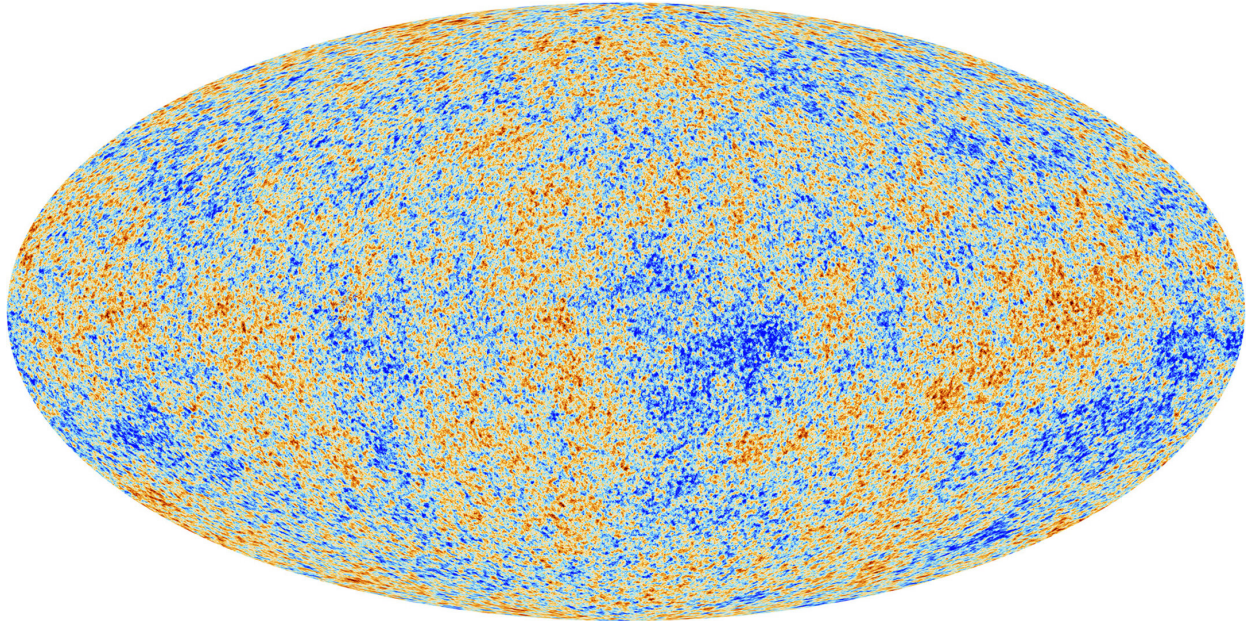


Figure 2.4 Plank CMB sky. Sky map features small variations in temperature in primordial light. These anisotropies are used to make inferences about the universe’s energy budget and developmental history. [10]

420 **2.3.3 Evidence for Dark Matter: Cosmic Microwave Background**

421 The Cosmic Microwave Background (CMB) is the primordial light from the early universe
422 when Hydrogen atoms formed from the free electron and proton soup in the early universe. The
423 CMB is the earliest light we can observe; released when the universe was about 380,000 years old.
424 Then we look at how the simulated universes look like compared to what we see. Figure 2.4 is the
425 most recent CMB image from the Plank satellite after subtracting the average value and masking the
426 galactic plane [10]. Redder regions indicate a slightly hotter region in the CMB, and blue indicates
427 colder. The intensity variations are on the order of 1 in 1000 with respect to the average value.

428 The Cosmic Microwave Background shows that the universe had DM in it from an incredibly
429 early stage. To measure the DM, Dark Energy, and matter fractions of the universe from the CMB,
430 the image is analyzed into a power spectrum, which shows the amplitude of the fluctuations as
431 a function of spherical multipole moments. Λ CDM provides the best fit to the power spectra of
432 the CMB as shown in Figure 2.5. The CMB power spectrum is quite sensitive to the fraction
433 of each energy contribution in the early universe. Low l modes are dominated by variations
434 in gravitational potential. Intermediate l emerge from oscillations in photon-baryon fluid from

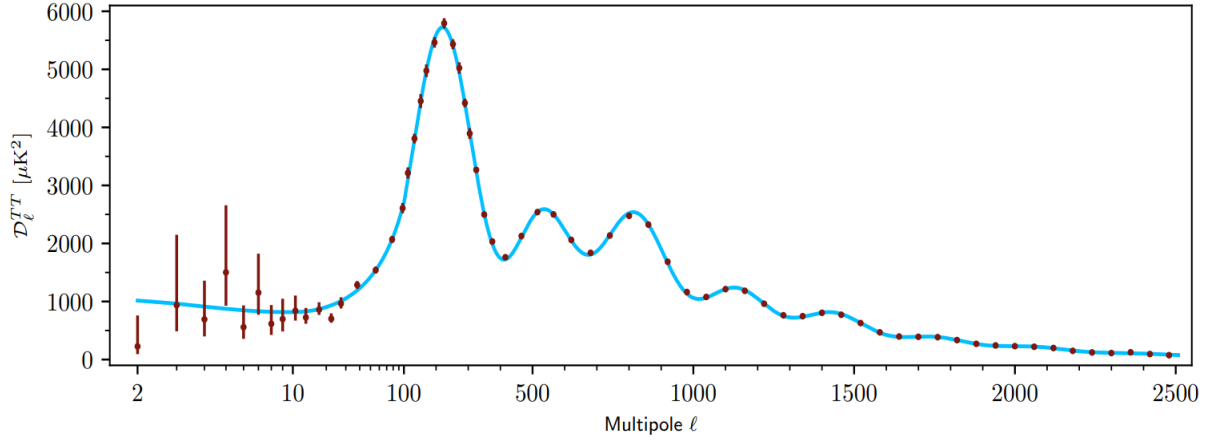


Figure 2.5 Observed Cosmic Microwave Background power spectrum as a function of multipole moment from Plank [10]. Blue line is best fit model from Λ CDM. Red points and lines are data and error, respectively.

435 competing baryon pressures and gravity. High l is a damped region from the diffusion of photons
 436 during electron-proton recombination. [1]

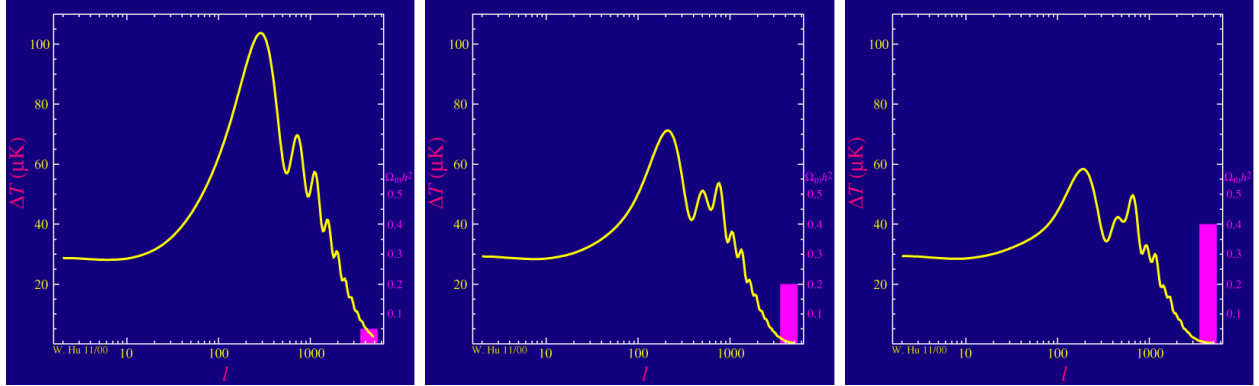


Figure 2.6 Predicted power spectra of CMB for different $\Omega_m h^2$ values for fixed baryon density from [11]. (left) Low $\Omega_m h^2$ increases the prominence of first and second peaks. (middle) $\Omega_m h^2$ is most similar to the observed power spectrum. The second and third peaks are similar in height. (right) $\Omega_m h^2$ is large which suppresses the first peak and raises the prominence of the third peak.

437 The harmonics would look quite different for a universe with less DM. Figure 2.6 demonstrates
 438 the effect $\Omega_m h^2$ has on the expected power spectrum for fixed baryon matter density. [11] Sweeping
 439 $\Omega_m h^2$ in this way clearly shows the effect dark matter has on the CMB power spectrum. The
 440 observations fit well with the Λ CDM model, and the derived fractions are as follows. The matter
 441 fraction: $\Omega_m = 0.3153$; and the baryon fraction: $\Omega_b = 0.04936$ [10]. Plank's observations also
 442 provide a measure of the Hubble constant, H_0 . H_0 especially has seen a growing tension in the

443 past decade that continues to deepened with observations from instruments like the James Webb
444 Telescope [12, 13]. As Hubble tensions deepen, we may find that perhaps Λ **CDM**, despite its
445 successes, is missing some critical physics.

446 Overall, the Newtonian motion of stars in galaxies, weak lensing from galactic clusters, and
447 power spectra from primordial light form a compelling body of research in favor of dark matter.
448 It takes another leap of theory and experimentation to make observations of DM that are non-
449 gravitational in nature. In Section 2.3, the evidence for DM implies strongly that the DM is matter
450 and not a lost parameter in the gravitational fields between massive objects. Finally, if we take one
451 axiom: that this matter has quantum behavior, such as being described by some Bohr wavelength
452 and abiding by some fermion or boson statistics; then we arrive at particle dark matter. One particle
453 DM hypothesis is the Weakly Interacting Massive Particle (WIMP). This DM candidate theory is
454 discussed further in the next section and is the focus of this thesis.

455 **2.4 Searching for Dark Matter: Particle DM**

456 Section 2.4 shows the Standard Model of particle physics and is currently the most accurate
457 model for the dynamics of fundamental particles like electrons and photons. The current status
458 of the SM does not have a viable DM candidate. When looking at the standard model, we can
459 immediately exclude any charged particle because charged particles interact strongly with light.
460 Specifically, this will rule out the following charged, fundamental particles: $e, \mu, \tau, W, u, d, s, c, t, b$
461 and their corresponding antiparticles. Recalling from Section 2.2 that DM must be long-lived and
462 stable over the age of the universe which excludes all SM particles with decay half-lives at or shorter
463 than the age of the universe. The lifetime constraint additionally eliminates the Z and H bosons.
464 Finally, the candidate DM needs to be somewhat massive. Recall from Section 2.2 that DM is cold
465 or not relativistic through the universe. This eliminates the remaining SM particles: $\nu_{e,\mu,\tau}, g, \gamma$ as
466 DM candidates. Because there are no DM candidates within the SM, the DM problem strongly
467 hints to physics beyond the SM (BSM).

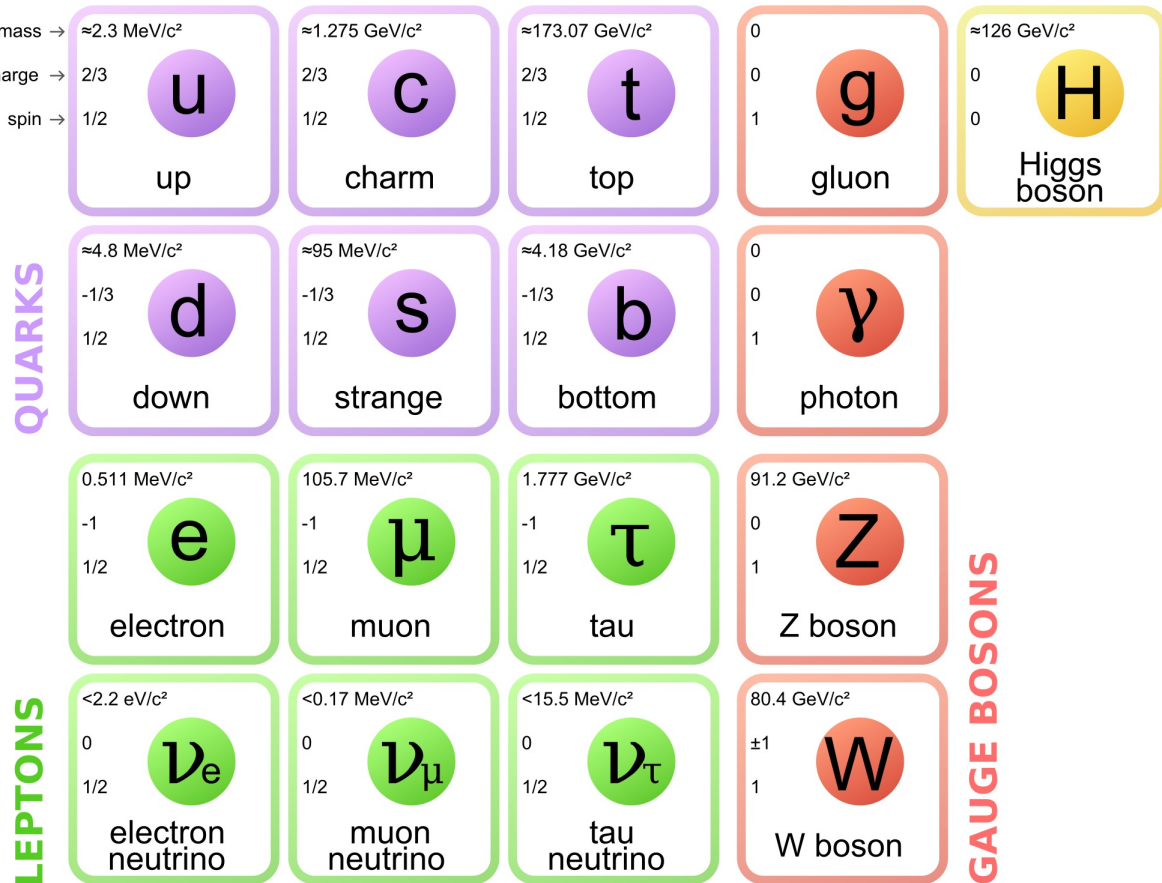


Figure 2.7 The Standard Model (SM) of particle physics. Figure taken from <http://www.quantumdiaries.org/2014/03/14/the-standard-model-a-beautiful-but-flawed-theory/>

468 2.4.1 Shake it, Break it, Make it

469 When considering DM that couples in some way with the SM, the interactions are roughly
 470 demonstrated by interaction demonstrated in Figure 2.8. The figure is a simplified Feynman
 471 diagram where the arrow of time represents the interaction modes of: **Shake it, Break it, Make it**.

472 **Shake it** refers to the direct detection of dark matter. Direct detection interactions start with
 473 a free DM particle and an SM particle. The DM and SM interact via elastic or inelastic collision
 474 and recoil away from each other. The DM remains in the dark sector and imparts some momentum
 475 onto the SM particle. The hope is that the momentum imparted onto the SM particle is sufficiently
 476 high enough to pick up with extremely sensitive instruments. Because we cannot create the DM in
 477 the lab, a direct detection experiment must wait until DM is incident on the detector. Most direct
 478 detection experiments are therefore placed in low-background environments with inert detection

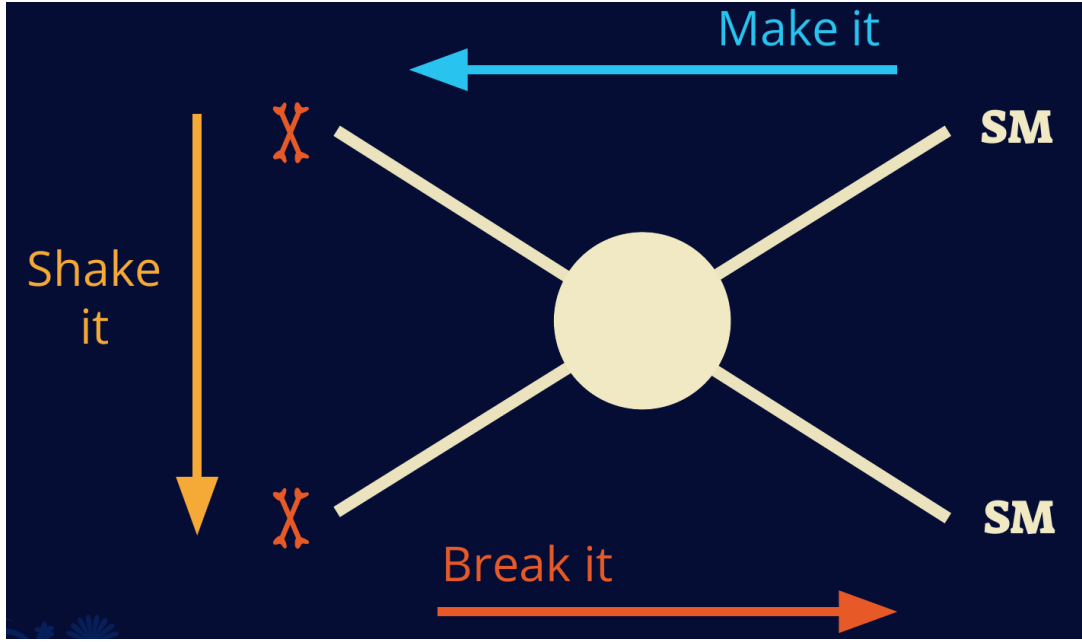


Figure 2.8 Simplified Feynman diagram demonstrating different ways DM can interact with SM particles. The 'X's refer to the DM particles whereas the SM refer to fundamental particles in the SM. The large circle in the center indicates the vertex of interaction and is purposely left vague. The colored arrows refer to different directions of time as well as their respective labels. The arrows indicate the initial and final state of the DM -SM interaction in time.

479 media like the noble gas Xenon. [14]

480 **Make it** refers to the production of DM from SM initial states. The experiment starts with
 481 particles in the SM. These SM particles are accelerated to incredibly high energies and then collide
 482 with each other. In the confluence of energy, DM hopefully emerges as a byproduct of the SM
 483 annihilation. Often it is the collider experiments that are energetic enough to hypothetically produce
 484 DM. These experiments include the world-wide collaborations ATLAS and CMS at CERN where
 485 proton collide together at extreme energies. The DM searches, however, are complex. DM likely
 486 does not interact with the detectors and lives long enough to escape the detection apparatus of
 487 CERN's colliders. This means any DM production experiment searches for an excess of events
 488 with missing momentum or energy in the events. An example event with missing transverse
 489 momentum is shown in Figure 2.9. The missing momentum with no particle tracks implies a
 490 neutral particle carried the energy out of the detector. However, there are other neutral particles
 491 in the SM, like neutrons or neutrinos, so any analysis has to account for SM signatures of missing

492 momentum. [15]

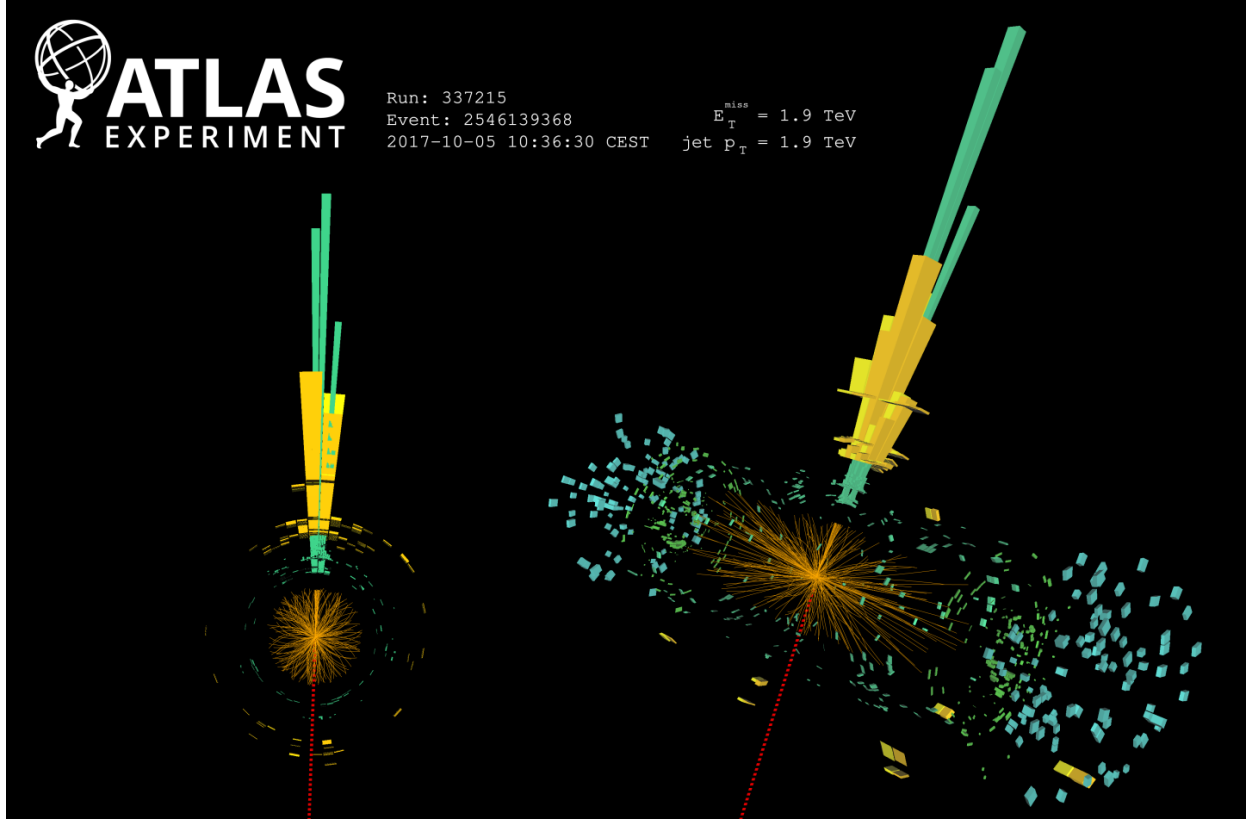


Figure 2.9 A single jet event in ATLAS detector from 2017 [16]. Jet momentum was observed to be 1.9 TeV. Missing transverse momentum was observed to be 1.9 TeV compared to the initial transverse momentum of the event was 0. Implied MET is traced by a red dashed line in event display.

493 **2.4.2 Break it: Standard Model Signatures of Dark Matter through Indirect Searches**

494 **Break it** refers to the creation of SM particles from the dark sector, and it is the primary focus
495 of this thesis. The interaction begins with DM or in the dark sector. The hypothesis is that this
496 DM will either annihilate with itself or decay and produce an SM byproduct. This method is
497 often referred to as the Indirect Detection of DM because we have no lab to directly control or
498 manipulate the DM. Therefore, most indirect DM searches are performed using observations of
499 known DM densities among the astrophysical sources. The strength is that we have the whole of the
500 universe and its 13.6-billion-year lifespan to use as a detector and particle accelerator. Additionally,
501 locations of dark matter are well cataloged since it was astrophysical observations that presented

502 the problem of DM in the first place.

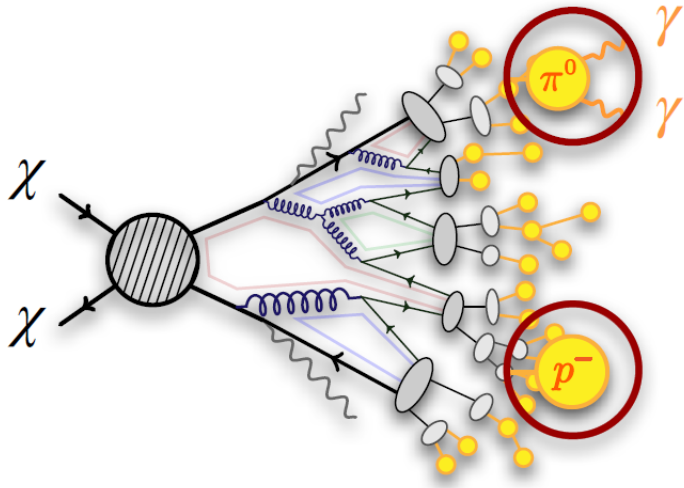


Figure 2.10 More detailed pseudo-Feynman diagram of particle cascade from dark matter annihilation into 2 quarks. The quarks hadronize and down to stable particles like γ or the anti-proton (p^-). Diagram pulled from ICRC 2021 presentation on DM annihilation search [17].

503 However, anything can happen in the universe. There are many difficult to deconvolve back-
504 grounds when searching for DM. One prominent example is the galactic center. We know the
505 galactic center has a large DM content because of stellar kinematics in our Milky Way and DM halo
506 simulations. Yet, any signal from the galactic center is challenging to parse apart from the extreme
507 environment of our supermassive black hole, unresolved sources, and diffuse emission from the
508 interstellar medium [18]. Despite the challenges, any DM model that yields evidence in the other
509 two observation methods, **Shake it or Make it** must be corroborated with indirect observations of
510 the known DM sources. Without corroborating evidence, DM observation in the lab is hard-pressed
511 to demonstrate that it is the model contributing to the DM seen at the universal scale.

512 In the case of WIMP DM, signals are described in terms of primary SM particles produced
513 from DM decay or annihilation. The SM initial state particles are then simulated down to stable
514 final states such as the γ , ν , p , or e which can traverse galactic lengths to reach Earth.

515 Figure 2.10 shows the quagmire of SM particles that emerges from SM initial states that are not
516 stable [17]. There are many SM particles with varying energies that can be produced in such an

517 interaction. For any arbitrary DM source and stable SM particle, the SM flux from DM annihilating
 518 to a neutral particle in the SM, ϕ , from a region in the sky is described by the following.

$$\frac{d\Phi_\phi}{dE_\phi} = \frac{\langle\sigma v\rangle}{8\pi m_\chi^2} \frac{dN_\phi}{dE_\phi} \times \int_{\text{source}} d\Omega \int_{l.o.s} \rho_\chi^2 dl(r, \theta') \quad (2.4)$$

519 In Equation (6.1), $\langle\sigma v\rangle$ is the velocity-weighted annihilation cross-section of DM to the SM. m_χ
 520 refers to the mass of DM, noted with Greek letter χ . $\frac{dN_\phi}{dE_\phi}$ is the N particle flux weighted by the
 521 particle energy. An example is provided in Figure 2.11 for the γ final state. The integrated terms
 522 are performed over the solid angle, $d\Omega$, and line of sight, l.o.s. ρ is the density of DM for a
 523 location (r, θ') in the sky. The terms left of the ' \times ' are often referred to as the particle physics
 524 component. The terms on the right are referred to as the astrophysical component. For decaying
 525 DM, the equation changes to...

$$\frac{d\Phi_\phi}{dE_\phi} = \frac{1}{4\pi\tau m_\chi} \frac{dN_\phi}{dE_\phi} \times \int_{\text{source}} d\Omega \int_{l.o.s} \rho_\chi dl(r, \theta') \quad (2.5)$$

526 In Equation (7.1), τ is the decay lifetime of the DM. Just as in Equation (6.1), the left and right
 527 terms are the particle physics and the astrophysical components respectively. The integrated
 528 astrophysical component of Equation (6.1) is often called the J-Factor. Whereas the integrated
 529 astrophysical component of Equation (7.1) is often called the D-Factor.

530 Exact DM $\text{DM} \rightarrow \text{SM SM}$ branching ratios are not known, so it is usually assumed to go 100%
 531 into an SM particle/anti-particle. Additionally, when a DM annihilation or decay produces one of
 532 the neutral, long-lived SM particles (ν or γ), the particle is traced back to a DM source. For DM
 533 above GeV energies, there are very few SM processes that can produce particles with such a high
 534 energy. Seeing such a signal would almost certainly be an indication of the presence of dark matter.
 535 Fortunately, the universe provides us with the largest volume and lifetime ever for a particle physics
 536 experiment.

537 2.5 Sources for Indirect Dark Matter Searches

538 The first detection of DM relied on optical observations. Since then, we have developed new
 539 techniques to find DM dense regions. As described in Section 2.3.1, many DM dense regions were
 540 through observing galactic rotation curves. Our Milky Way galaxy is among DM dense regions

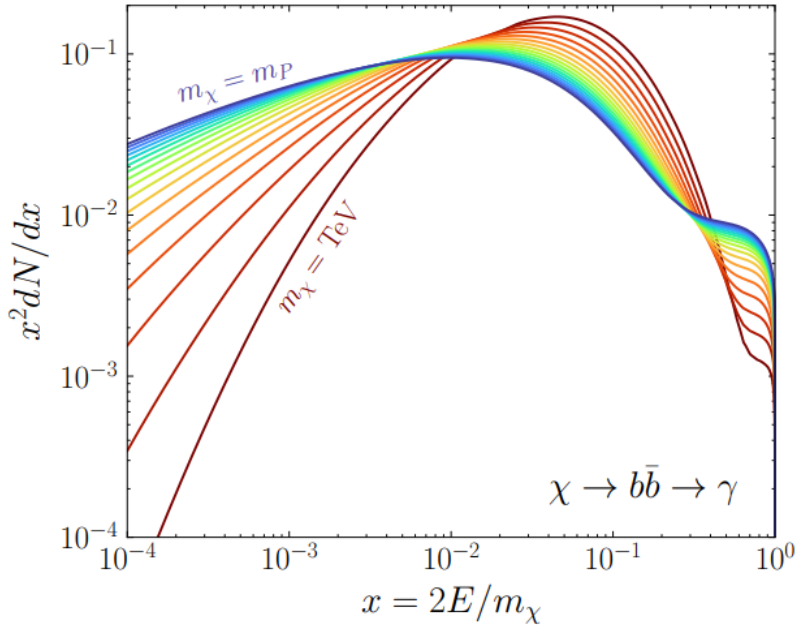


Figure 2.11 Dark Matter (DM) decay spectrum for $b\bar{b}$ initial state and γ final state. Redder spectra are for larger DM masses. Bluer spectra are light DM masses. x is a unitless factor defined as the ratio of the mass of DM, m_χ , and the final state particle energy E_γ . Figure from [19].

discovered, and it is the largest nearby DM dense region to look at. Additionally, the DM halo surrounding the Milky Way is clumpy [18]. There are regions in the DM halo of the Milky Way that have more DM than others that have captured gas over time. These sub-halos were dense enough to collapse gas and form stars. These apparent sub galaxies are known as dwarf spheroidal galaxies and are the main sources studied in this thesis. Each source type comes with different trade-offs. Galactic Center studies will be very sensitive to the assumed distribution of DM. The central DM density can vary substantially as demonstrated in Figure 2.12. At distances close to the center of the galaxy, or small r , the differences in DM densities can be 3-4 orders of magnitude. Searches toward the galactic center will therefore be quite sensitive to the assumed DM distribution.

Searches toward Dwarf Spheroidal Galaxies (dSph's) suffer from uncertainties in the DM density less than the galactic center studies. This is mostly from their diminutive size being smaller than the angular resolution of most γ -ray observatories [18]. The DM content dSph's are typically determined with the Virial theorem, Equation (2.1), and are usually majority DM [18] in mass. DSph's tend to be ideal sources to look at for DM searches. Their environments are quiet with little

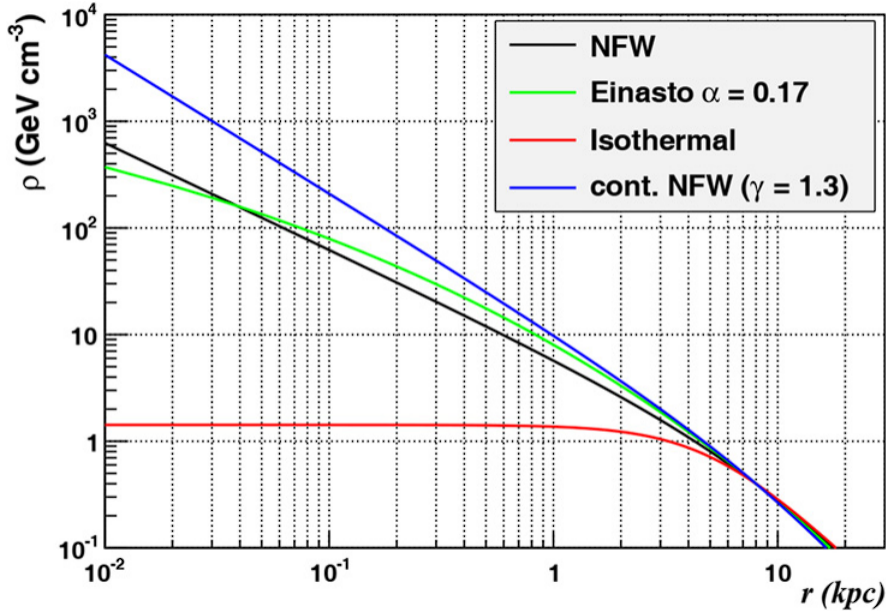


Figure 2.12 Different dark matter density profiles compared. Some models produce exceptionally large densities at small r [20].

555 astrophysical background. Unlike the galactic center, the most active components of dSph's are the
 556 stars within them versus a violent accretion disc around a black hole. All this together means that
 557 dSph's are among the best sources to look at for indirect DM searches. dSph's are the targets of
 558 focus for this thesis.

559 2.6 Multi-Messenger Dark Matter

560 Astrophysics entered a new phase in the past few decades that leverages our increasing sensitivity
 561 to SM channels and general relativity (GR). Up until the 21st century, astrophysical observations
 562 were performed with photons (γ) only. Astrophysics with this 'messenger' is fairly mature now.
 563 Novel observations of the universe have since only adjusted the sensitivity of the wavelength of
 564 light that is observed except at MeV energies. Gems like the CMB [10], and more have ultimately
 565 been observations of different wavelengths of light. Multi-messenger astrophysics proposes using
 566 other SM particles such the p^{+-} , or ν or gravitation waves predicted by general relativity.

567 The experiment LIGO had a revolutionary discovery in 2016 with the first detection of a binary
 568 black hole merger [21]. This opened the collective imagination to observing the universe through
 569 gravitational waves. There has also been a surge of interest in the neutrino (ν) sector. IceCube

570 demonstrated that we are sensitive to neutrinos in regions that correlate with significant photon
 571 emission like the galactic plane [22]. Neutrinos, like gravitational waves and light, travel mostly
 572 unimpeded from their source to our observatories. This makes pointing to the originating source
 573 of these messengers much easier than it is for cosmic rays which are deflected from their source by
 574 magnetic fields.

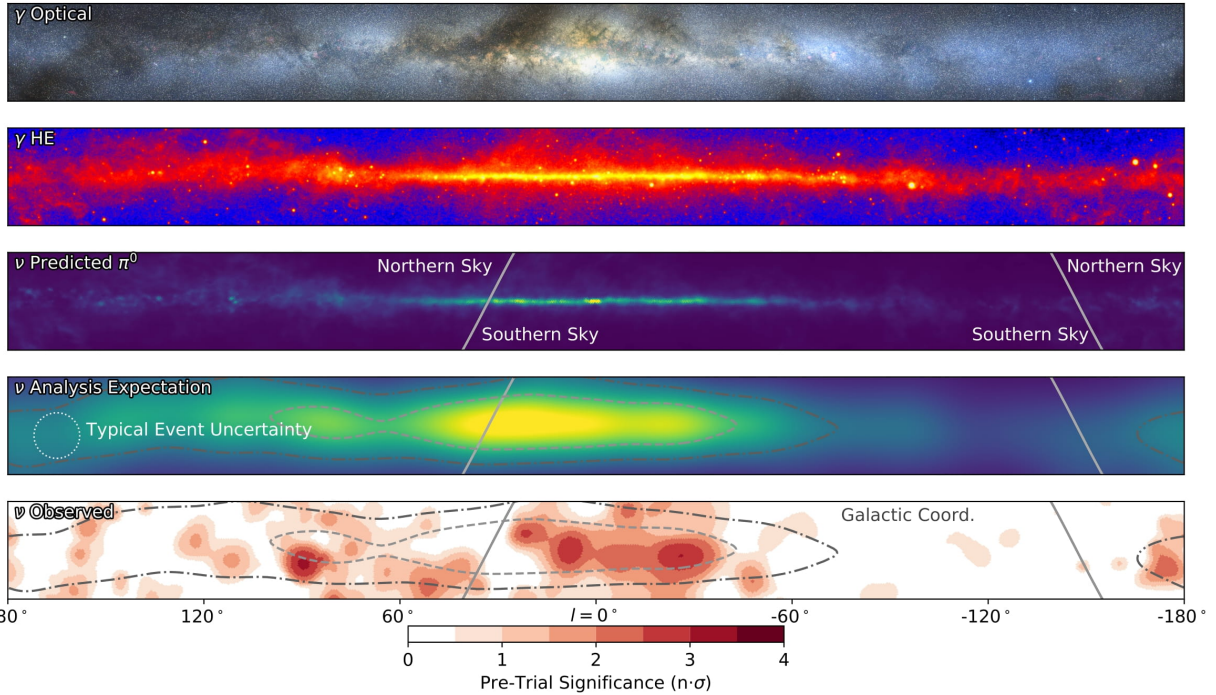


Figure 2.13 The Milky Way Galaxy in photons (γ) and neutrinos (ν) [22]. The Galactic center is at $l=0^\circ$ and is the brightest region in all panels. (top) An Optical color image of the Milky Way galaxy seen from Earth. Clouds of gas and dust obscure some light from stars. (2nd down) Integrated flux of γ -rays observed by the Fermi-LAT telescope [23]. (middle) Expected neutrino emission that corresponds with Fermi-LAT observations. (2nd up) Expected neutrino emission profile after considering detector systematics of IceCube. (bottom) Observed neutrino emission from region of the galactic plane. Substantial neutrino emission was detected.

575 The IceCube collaboration recently published a groundbreaking result of the Milky Way in
 576 neutrinos. The recent result from IceCube, shown in Figure 2.13, proves that we can make
 577 observations under different messenger regimes. The top two panels show the appearance of the
 578 galactic plane to different wavelengths of light. Some sources are more apparent in some panels,
 579 while others are not. This new channel is powerful because neutrinos are readily able to penetrate
 580 through gas and dust in the Milky Way. This new image also refines our understanding of how high

581 energy particles are produced. For example, the fit to IceCube data prefers neutrino production
 582 from the decay of π^0 [22].

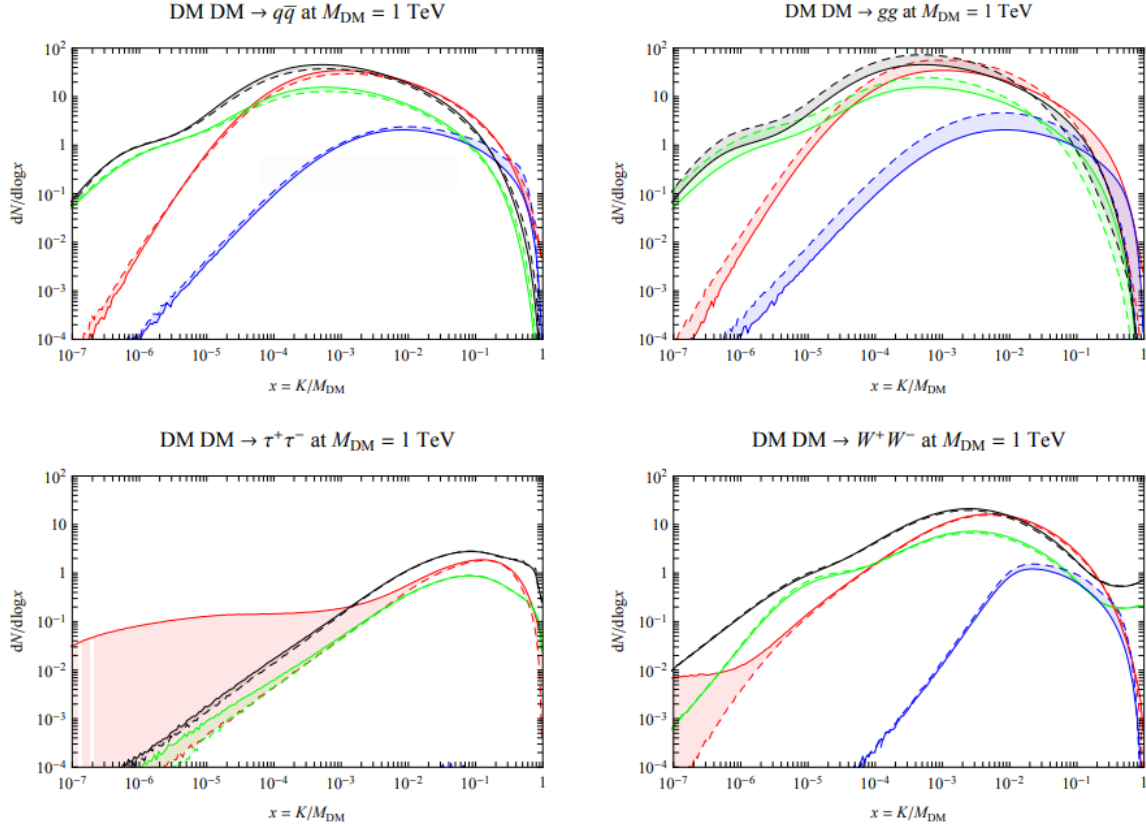


Figure 2.14 Dark Matter annihilation spectra for different final state particle and standard model annihilation channels [24]. Photons (red), e^\pm (green), \bar{p} (blue), ν (black).

583 Exposing our observations to more cosmic messengers greatly increases our sensitivity to
 584 rare processes. In the case of DM, Figure 2.14, there are many SM particles produced in DM
 585 annihilation. Among the final state fluxes are gammas and neutrinos. Charged particles are also
 586 produced however they would not likely make it to Earth since they will be deflected by magnetic
 587 fields between the source and Earth. This means observatories that can see the neutral messengers
 588 are especially good for DM searches and for combining data for a multi-messenger DM search.

CHAPTER 3

589 MULTIMESSENGER ASTROPHYSICS: DETECTING HIGH ENERGY NEUTRAL 590 MESSENGERS

591 3.1 Introduction

592 Before the 20th century, all astrophysics observations were optical in nature. We literally only
593 saw things with highly magnified optical observations. Then we discovered cosmic rays. cosmic
594 rays are charged particles, typically naked protons or H+. This was seen by Victor Hess in 19??.
595 Around the same time we discovered neutrinos from beta decay. Sometime around 1950 we started
596 to build neutrino detectors which were mostly sensitive to neutrinos from the sun. Finally, it was
597 theorized that compact objects like black holes and neutron stars would create waves in space-time
598 when they experience mergers or collisions.

599 In the 21st century, we have developed new observation techniques and detectors that are no only
600 sensitive to these four messengers - photons ([TODO: photon](#)), neutrinos ([TODO: nu](#)), Cosmic
601 Rays (CR), and Gravitational Wave (WV) - we're collect high energy versions of these events.
602 For the standad model particles, we're now sensitive to all messengers above the MeV eneryg
603 range. Additionally, the GW's were sensitive to are in the stellar mass black hole region and above
604 within our galactic neighborhood. This means were becoming sensitive to the fundamental physics
605 occuring within the universe and we can rely on the universe as a TeV+ particle accelerator. We
606 also have the abaility to correlate high energy events across messengers and gain new insights on
607 the processes that occur in our universe.

608 This thesis focuses on very high energy (VHE) gamma rays and neutrinos. These can both be
609 observed through the water cherenkov detection technique altho not exclusively. Methods on how
610 to detect and observe these neutral messengers are discussed Section 3.3 and Section 3.4

611 3.2 Charged Particles in a Medium

612 For high enery gamma-rays and neutrinos, we can exploit the same effect that charged particles
613 have with water. This effect is known as Cherenkov radiation. Cherenkov Radiation occurs when a
614 charged particle, usually electrons (e) or muons (μ), traverse a medium, like water, faster than the

615 speed of light in that medium. This is similar to sonic boom where an object moves through air
616 faster than the speed of sound in air. Cherenkov radiation can therefore be thought of as an 'optic
617 boom'. Many astro-particle physics experiments will use water as the medium as because water
618 has a unique set of properties ideal for charged particle tracking.



Figure 3.1 TODO: Show a nuclear reactor with cherenkov radiation[NEEDS A SOURCE][FACT CHECK THIS]

619 The frequency of light emitted due to cherenkov radiation follows the equation:

$$INSERT\ Cherenkov\ wavelength\ calc\ HERE. \quad (3.1)$$

620 The absorption spectra is shown in the following figure:

621 **3.3 Photons (γ)**

622 **3.4 Neutrinos (ν)**

623 **3.5 Opportunities to Combine for Dark Matter**



Figure 3.2 TODO: absorption spectrum of liquid and solid water[NEEDS A SOURCE][FACT CHECK THIS]

CHAPTER 4

624 **HIGH ALTITUDE WATER CHERENKOV (HAWC) OBSERVATORY**

625 **4.1 The Detector**

626 **4.2 Events Reconstruction and Data Acquisition**

627 **4.2.1 G/H Discrimination**

628 **4.2.2 Angle**

629 **4.2.3 Energy**

630 **4.3 Remote Monitoring**

631 **4.3.1 ATHENA Database**

632 **4.3.2 HOMER**

633

CHAPTER 5

ICECUBE NEUTRINO OBSERVATORY

634 **5.1 The Detector**

635 **5.2 Events Reconstruction and Data Acquisition**

636 **5.2.1 Angle**

637 **5.2.2 Energy**

638 **5.3 Northern Test Site**

639 **5.3.1 PIgeon remote dark rate testing**

640 **5.3.2 Bulkhead Construction**

CHAPTER 6

GLORY DUCK: MULTI-WAVELENGTH SEARCH FOR DARK MATTTER ANNIHILATION TOWARDS DWARF SPHEROIDAL GALAXIES

6.1 Introduction

The field of astrophysics now has several instruments and observatories sensitive to high energy gamma-rays. The energy sensitivity for the modern gamma-ray program spans many orders of magnitude. Figure 6.1 demonstrates these similar sensitivities across energies for the five experiments: Fermi-LAT, HAWC, HESS, MAGIC, and VERITAS.

Each of the five experiments featured in Figure 6.1 have independently searched for DM annihilation from dwarf spheroidal galaxies (dSph) and set limits. Intriguingly, there are regions of substantial overlap in their energy sensitivities. This clearly motivates an analysis that combines data from these five. Each experiment has unique gamma-ray detection methods and their weaknesses and strengths can be leveraged with each other. The HAWC gamma-ray observatory is extensively introduced in chapter 4, so it is not introduced here. A brief description of the remaining experiments are in the following paragraphs.

The Large Area Telescope (LAT) is a pair conversion telescope mounted on the NASA Fermi satellite in orbit \sim 550 km above the Earth [26]. LAT's field of view covers about 20% of the whole sky, and it sweeps the whole sky approximately every 3 hours. LAT's gamma-ray energy sensitivity ranges from 20 MeV up to 1 TeV. Previous DM searches towards dSphs using Fermi-LAT are published in [27] and [28]

The High Energy Spectroscopic System (HESS), Major Atmospheric Gamma Imaging Cherenkov (MAGIC), and Very Energetic Radiation Imaging Telescope Array System (VERITAS) are arrays of Imaging Atmospheric Cherenkov Telescopes (IACT). These telescopes observe the Cherenkov light emitted from gamma-ray showers in the Earth's atmosphere. The field of view for these telescopes is no larger than 5° with energy sensitivities ranging from 30 GeV up to 100 TeV [29, 30, 31]. IACTs are able to make precise observations in selected regions of the sky, however can only be operated in ideal dark conditions. HESS's observations of the dwarves

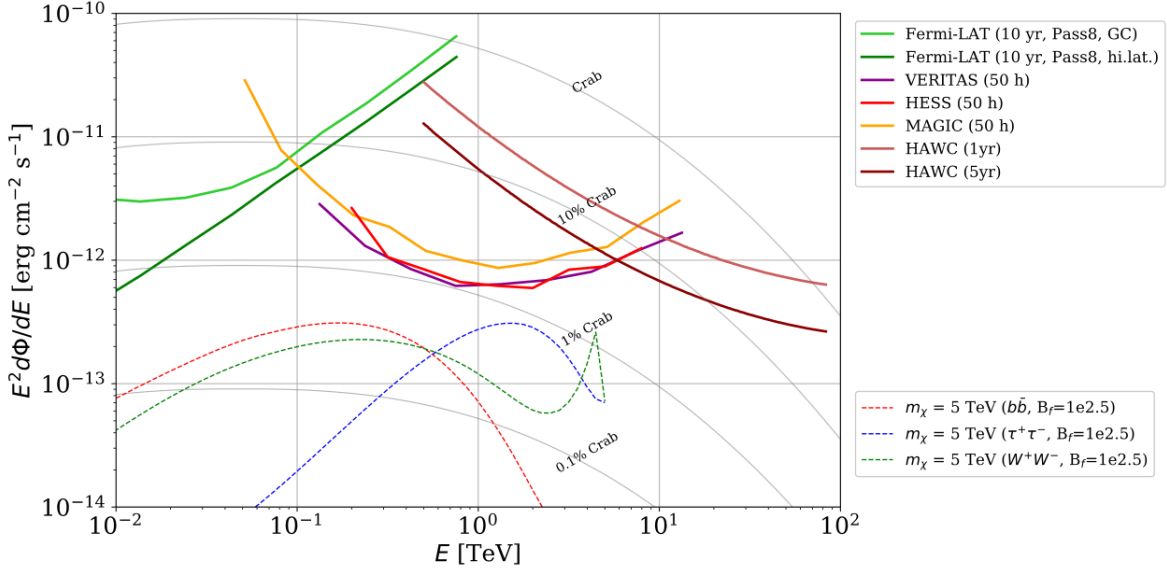


Figure 6.1 Sensitivities of five gamma-ray experiments compared to percentages of the Crab nebula’s emission and dark matter annihilation. Solid lines present estimated sensitivities to power law spectra [FACT CHECK THIS] for each experiment. Green lines are Fermi-LAT sensitivities where lighter green is the sensitivity to the galactic center and dark green is its sensitivity to higher declinations. Orange, red, and purple solid lines represent the MAGIC, HESS, and VERITAS 50 hour sensitivities respectively. The maroon and brown lines are the HAWC 1 year and 5 year sensitivities. Across four decades of gamma-ray energy, these experiments have similar sensitivities on the order 10^{-12} erg $\text{cm}^{-2}\text{s}^{-1}$. The dotted lines are estimated dark matter fluxes assuming $m_\chi = 5$ TeV DM annihilating to bottom quarks (red), tau leptons (blue), and W bosons (green). Faded gray lines outline percentage flux of the Crab nebula. Figure is an augmented version of [25]

667 Sculptor and Carina were between January 2008 and December 2009. HESS’s observations of
 668 Coma Berenices were from 2010 to 2013, and Fornax was observed in 2010 [32, 33, 34]. MAGIC
 669 provided deep observations of Segue1 between 2011 and 2013 [35]. MAGIC also provides data
 670 for three dwarves: Coma Berenices, Draco, and Ursa Major II where observations were made
 671 in: January - June 2019 [36], March - September 2018 [36], and 2014 - 2016 [37] respectively.
 672 VERITAS provided data for Boötes I, Draco, Segue 1, and Ursa Minor from 2009 to 2016 [38].

673 This chapter presents the Glory Duck analysis, the name given for the search for dark matter
 674 annihilation from dSph by combining data from the five gamma-ray observatories: Fermi-LAT,
 675 HAWC, HESS, MAGIC, and VERITAS. Specifically, the methods in analysis and modeling are
 676 presented for the HAWC gamma-ray observatory. This work was published to the Journal of
 677 Cosmology and Astroparticle Physics and presented at the International Cosmic Ray Conference

678 in 2019, 2021, and 2023 [39, 40, 41] and others.

679 **6.2 Dataset and Background**

680 This section enumerates the data and background methods used for HAWC’s study of dSphs.
681 Section 6.2.1 and Section 6.2.2 are most useful for fellow HAWC collaborators looking to replicate
682 the Glory Duck analysis.

683 **6.2.1 Itemized HAWC files**

- 684 • Detector Resolution: `response_aerie_svn_27754_systematics_best_mc_test_no`
685 `broadpulse_10pctlogchargesmearing_0.63qe_25kHzNoise_run5481_curvatu`
686 `re0_index3.root`
- 687 • Data Map: `maps-20180119/liff/maptree_1024.root`
- 688 • Spectral Dictionary: `DM_CirrelliSpectrum_dict_gammas.npy`
- 689 • Analysis wiki: https://private.hawc-observatory.org/wiki/index.php/Glory_Duck_Multi-Experiment_Dark_Matter_Search

691 **6.2.2 Software Tools and Development**

692 This analysis was performed using HAL and 3ML [42, 43] in Python version 2. I built software
693 to implement the *A Poor Particle Physicist Cookbook for Dark Matter Indirect Detection* (PPPC)
694 [44] DM spectral model and dSphs spatial model from [45] for HAWC analysis. A NumPy version
695 of this dictionary was made for both Py2 and Py3. The code base for creating this dictionary is
696 linked on my GitLab sandbox:

- 697 • Py2: [Dictionary Generator \(Deprecated\)](#)
- 698 • Py3: [PPPC2Dict](#)

699 The analysis was performed using the f_{hit} framework performed in the HAWC Crab paper
700 [42]. The Python2 NumPy dictionary file for gamma-ray final states is `dmCirSpecDict.npy`. The
701 corresponding Python3 file is `DM_CirrelliSpectrum_dict_gammas.npy`. These files can also

702 be used for decay channels and the PPPC describes how [44]. All other software used for data
703 analysis, DM profile generation, and job submission to SLURM are also kept in my sandbox for
704 [the Glory Duck](#) project.

705 **6.2.3 Data Set and Background Description**

706 The HAWC data maps used for this analysis contain 1017 days of data between runs 2104
707 (2014-11-26) and 7476 (2017-12-20). They were generated from pass 4.0 reconstruction. The
708 analysis is performed using the f_{hit} energy binning scheme with bins (1-9) similar to what was done
709 for the Crab and previous HAWC dSph analysis [42, 46]. Bin 0 was excluded as it has substantial
710 hadronic contamination and poor angular resolution.

711 This analysis was done on dSphs because of their large DM mass content relative to baryonic
712 mass. We consider the following to estimate the background to this study.

- 713 • The dSphs are small in HAWC’s field of view, so the analysis is not sensitive to large or small
714 scale anisotropies.
- 715 • The dSphs used in this analysis are off the galactic plane.
- 716 • The dSphs are baryonically faint relative to their expected dark matter content and are not
717 expected to contain high energy gamma-ray sources.

718 Therefor we make no additional assumptions on the background from our sources and use
719 HAWC’s standard direct integration method for background estimation [42]. It is possible for
720 gamma rays from DM annihilation to scatter in transit to HAWC via Inverse Compton Scattering
721 (ICS). This was investigated and its impact on the flux is basically zero. Supporting information
722 on this is in Section 6.7.1

723 **6.3 Analysis**

724 The expected differential photon flux from DM-DM annihilation to standard model particles,
725 $d\Phi_\gamma/dE_\gamma$, over solid angle, Ω is described by the familiar equation.

$$\frac{d\Phi_\gamma}{dE_\gamma} = \frac{\langle\sigma v\rangle}{8\pi m_\chi^2} \frac{dN_\gamma}{dE_\gamma} \times \int_{\text{source}} d\Omega \int_{l.o.s} \rho_\chi^2 dl(r, \theta') \quad (6.1)$$

726 Where $\langle \sigma v \rangle$ is the velocity weighted annihilation cross-section. $\frac{dN}{dE}$ is the expected differential
 727 number of photons produced at each energy per annihilation. m_χ is the rest mass of the supposed
 728 DM particle. ρ_χ is the DM density. J is the astrophysical J-factor and is defined as

$$J = \int d\Omega \int_{l.o.s} dl \rho_\chi^2(r, \theta') \quad (6.2)$$

729 l is the distance to the source from Earth. r is the radial distance from the center of the source. θ' is
 730 the half angle defining a cone containing the DM source. How each component is synthesized and
 731 considered for HAWC's analysis is presented in the following sections. Section 6.3.1 presents the
 732 particle physics model for DM annihilation. Section 6.3.2 presents the spatial distributions built
 733 for each dSph.

734 6.3.1 $\frac{dN_\gamma}{dE_\gamma}$ - Particle Physics Component

735 For these spectra, we import the PPPC with Electroweak (EW) corrections [44]. The spectrum
 736 is implemented as a model script in astromodels for 3ML. The EW corrections were previously not
 737 considered for HAWC and are significant for DM annihilating to EW coupled SM particles such
 738 as all leptons, and the γ , Z , and W bosons [46]. Figure 6.2 demonstrates the significance of EW
 739 corrections for W boson annihilation. Across EW SM channels, the gamma-ray spectra become
 740 harder than spectra without EW corrections. Tables from the PPPC were reformatted into Python
 741 NumPy dictionaries for collaboration-wide use. A class in astromodels was developed to include
 742 the EW correction from the PPPC and is aptly named `PPPCSpectra` within `DM_models.py`.

743 6.3.2 J - Astrophysical Component

744 The J-factor profiles for each source are imported from Geringer-Sameth (referred to with \mathcal{GS})
 745 [45]. These were pulled from the publication as $J(\theta)$, where θ is the angular separation from the
 746 center of the source. HAWC requires maps in terms of $\frac{dJ}{d\Omega}$, so the conversion from the maps was
 747 done in the following way...

748 First, convert the angular distances to solid angles

$$\Omega = 2 \cdot \pi(1 - \cos(\theta)) \quad (6.3)$$

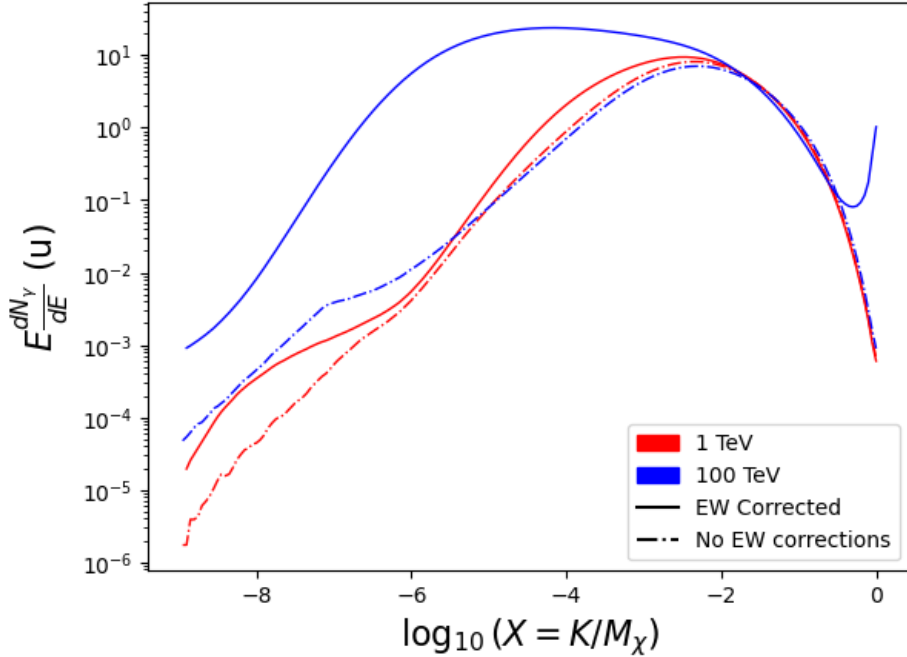


Figure 6.2 Effect of Electroweak (EW) corrections on expected DM annihilation spectrum for $\chi\chi \rightarrow W^-W^+$. Solid lines are spectral models that consider EW corrections. Dash-dot lines are spectral models without EW corrections. Red lines are models for $M_\chi = 1$ TeV. Blue lines represent models for $M_\chi = 100$ TeV. All models are sourced from the PPPC4DMID [44].

749 which reduces with a small angle approximation to $\pi\theta^2$. Next, the central difference for both the
 750 ΔJ and $\Delta\Omega$ value were calculated from the discretized $J(\theta)$ with the central difference stencil:

$$\Delta\phi_i = \phi_{i+1} - \phi_{i-1} \quad (6.4)$$

751 Where ϕ is either Ω or J . These were done separately in case the grid spacing in θ was not uniform.
 752 Finally, these lists are divided so that we are left with an approximation of the $dJ/d\Omega$ profile that
 753 is a function of θ . Admittedly, this is an approximation method for the map which introduces small
 754 errors compared to the true profile estimate. This was checked as a systematic against the author's
 755 profiling of the spatial distribution and is documented in Section 6.8.1.

756 With $\frac{dJ}{d\Omega}(\theta)$, a map is generated, first by filling in the north-east quadrant of the map. This
 757 quadrant is then reflected twice, vertically then horizontally, to fill the full map. Maps are then
 758 normalized by dividing the discrete 2D integral of the map. The 2D integral was a simple height

759 of bins, Newton's integral:

$$p^2 \cdot \sum_{i,j=0}^{N,M} \frac{dJ}{d\Omega}(\theta_{i,j}, \phi_{i,j}) \quad (6.5)$$

760 These maps are HEALpix maps with NSIDE 16384 and saved in the `.fits` format.

761 Another DM spatial distribution model from Bonnivard (\mathcal{B}) [47] was used for the Glory Duck
762 study. However, to save computational time, limits from \mathcal{GS} were scaled to \mathcal{B} instead of each
763 experiment performing a full study a second time. How these models compare is demonstrated
764 for each dSph in Figure 6.16 and Figure 6.17 Plots of these maps are provided for each source
765 in chapter A Examples of the two most impactful dSphs derived from \mathcal{GS} , Segue1 and Coma
766 Berenices are featured in Figure 6.3

767 6.3.3 Source Selection and Annihilation Channels

768 We use many of the dSphs presented in HAWC's previous dSph DM search [46]. HAWC's
769 sources for Glory Duck include Boötes I, Coma Berenices, Canes Venatici I + II, Draco, Hercules,
770 Leo I, II, + IV, Segue 1, Sextans, and Ursa Major I + II. A full description of all sources used
771 in Glory Duck is found in Table 6.1. Triangulum II was excluded from the Glory Duck analysis
772 because of large uncertainties in its J factor. Ursa Minor was excluded from HAWC's contribution
773 to the combination because the source extension model extended Ursa Minor beyond HAWC's field
774 of view. Ursa Minor was not expected to contribute significantly to the combined limit, so work
775 was not invested in a solution to include Ursa Minor.

776 This analysis improves on the previous HAWC dSph paper [46] in the following ways. Pre-
777 viously, the dSphs were treated and implemented as point sources. For this analysis, dSphs are
778 modeled and treated as extended source. The impact of this change with respect to the upper limit
779 is source dependent and is explored in Section 6.7.2. Previously, the particle physics model used for
780 gamma-ray spectra from DM annihilation did not have EW corrections where the PPPC includes
781 them. Finally, the gamma-ray ray dataset is much larger. The study performed here analyzes over
782 1000 days of data compared to 507.

783 The SM annihilation channels probed for the Glory Duck combination include $b\bar{b}$, $e\bar{e}$, $\mu\bar{\mu}$, $\tau\bar{\tau}$,
784 $t\bar{t}$, W^+W^- , and ZZ . A summary of all sources, with a description of each experiments' sensitivity

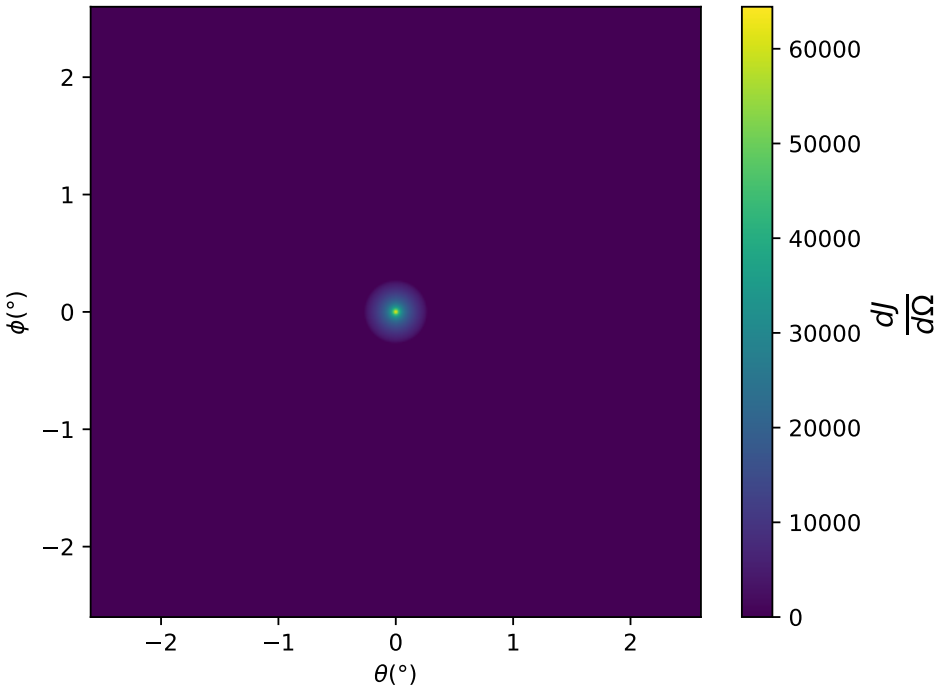
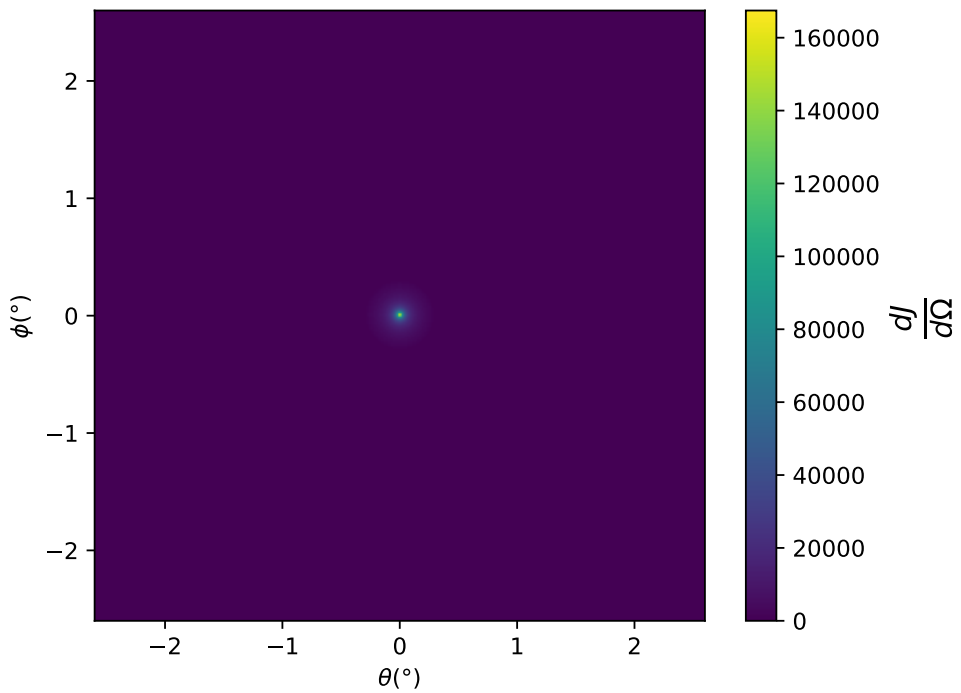


Figure 6.3 $\frac{dJ}{d\Omega}$ maps for Segue1 (top) and Coma Berenices (bottom). Origin is centered on the specific dwarf spheroidal galaxies (dSph). X and Y axes are the angular separation from the center of the dwarf. Plots of the remaining 11 dSph HAWC studied are linked in Fig. A.1.

Table 6.1 Summary of the relevant properties of the dSphs used in the present work. Column 1 lists the dSphs. Columns 2 and 3 present their heliocentric distance and galactic coordinates, respectively. Columns 4 and 5 report the J -factors of each source given from the \mathcal{GS} and \mathcal{B} independent studies and their estimated $\pm 1\sigma$ uncertainties. The values $\log_{10} J$ (\mathcal{GS} set) [45] correspond to the mean J -factor values for a source extension truncated at the outermost observed star. The values $\log_{10} J$ (\mathcal{B} set) [47] are provided for a source extension at the tidal radius of each dSph. **Bolded sources are within HAWC's field of view and provided to the Glory Duck analysis.**

Name	Distance (kpc)	l, b ($^{\circ}$)	$\log_{10} J$ (\mathcal{GS} set) $\log_{10}(\text{GeV}^2 \text{cm}^{-5} \text{sr})$	$\log_{10} J$ (\mathcal{B} set) $\log_{10}(\text{GeV}^2 \text{cm}^{-5} \text{sr})$
Boötes I	66	358.08, 69.62	$18.24^{+0.40}_{-0.37}$	$18.85^{+1.10}_{-0.61}$
Canes Venatici I	218	74.31, 79.82	$17.44^{+0.37}_{-0.28}$	$17.63^{+0.50}_{-0.20}$
Canes Venatici II	160	113.58, 82.70	$17.65^{+0.45}_{-0.43}$	$18.67^{+1.54}_{-0.97}$
Carina	105	260.11, -22.22	$17.92^{+0.19}_{-0.11}$	$18.02^{+0.36}_{-0.15}$
Coma Berenices	44	241.89, 83.61	$19.02^{+0.37}_{-0.41}$	$20.13^{+1.56}_{-1.08}$
Draco	76	86.37, 34.72	$19.05^{+0.22}_{-0.21}$	$19.42^{+0.92}_{-0.47}$
Fornax	147	237.10, -65.65	$17.84^{+0.11}_{-0.06}$	$17.85^{+0.11}_{-0.08}$
Hercules	132	28.73, 36.87	$16.86^{+0.74}_{-0.68}$	$17.70^{+1.08}_{-0.73}$
Leo I	254	225.99, 49.11	$17.84^{+0.20}_{-0.16}$	$17.93^{+0.65}_{-0.25}$
Leo II	233	220.17, 67.23	$17.97^{+0.20}_{-0.18}$	$18.11^{+0.71}_{-0.25}$
Leo IV	154	265.44, 56.51	$16.32^{+1.06}_{-1.70}$	$16.36^{+1.44}_{-1.65}$
Leo V	178	261.86, 58.54	$16.37^{+0.94}_{-0.87}$	$16.30^{+1.33}_{-1.16}$
Leo T	417	214.85, 43.66	$17.11^{+0.44}_{-0.39}$	$17.67^{+1.01}_{-0.56}$
Sculptor	86	287.53, -83.16	$18.57^{+0.07}_{-0.05}$	$18.63^{+0.14}_{-0.08}$
Segue I	23	220.48, 50.43	$19.36^{+0.32}_{-0.35}$	$17.52^{+2.54}_{-2.65}$
Segue II	35	149.43, -38.14	$16.21^{+1.06}_{-0.98}$	$19.50^{+1.82}_{-1.48}$
Sextans	86	243.50, 42.27	$17.92^{+0.35}_{-0.29}$	$18.04^{+0.50}_{-0.28}$
Ursa Major I	97	159.43, 54.41	$17.87^{+0.56}_{-0.33}$	$18.84^{+0.97}_{-0.43}$
Ursa Major II	32	152.46, 37.44	$19.42^{+0.44}_{-0.42}$	$20.60^{+1.46}_{-0.95}$
Ursa Minor	76	104.97, 44.80	$18.95^{+0.26}_{-0.18}$	$19.08^{+0.21}_{-0.13}$

785 to the source, is provided in Table 6.2.

786 6.4 Likelihood Methods

787 6.4.1 HAWC Likelihoods

788 For every analysis bin in energy, f_{hit} bins (1-9), and location, we can expect N signal events and
 789 B background events. The expected number of excess signal events from dark matter annihilation,

Table 6.2 Summary of dSph observations by each experiment used in this work. A ‘-’ indicates the experiment did not observe the dSph for this study. For Fermi-LAT, the exposure at 1 GeV is given. For HAWC, $|\Delta\theta|$ is the absolute difference between the source declination and HAWC latitude. HAWC is more sensitive to sources with smaller $|\Delta\theta|$. For IACTs, we show the zenith angle range, the total exposure, the energy range, the angular radius θ of the signal or ON region, the ratio of exposures between the background-control (OFF) and signal (ON) regions (τ), and the significance of gamma-ray excess in standard deviations, σ .

Source name	Fermi-LAT	HAWC	H.E.S.S, MAGIC, VERITAS						
	Exposure (10^{11} s m 2)	$ \Delta\theta $ (°)	IACT	Zenith (°)	Exposure (h)	Energy range (GeV)	θ (°)	τ	S (σ)
Boötes I	2.6	4.5	VERITAS	15 – 30	14.0	100–41000	0.10	8.6	-1.0
Canes Venatici I	2.9	14.6	–	–	–	–	–	–	–
Canes Venatici II	2.9	15.3	–	–	–	–	–	–	–
Carina	3.1	–	H.E.S.S.	27 – 46	23.7	310 – 70000	0.10	18.0	-0.3
Coma Berenices	2.7	4.9	H.E.S.S.	47 – 49	11.4	550 – 70000	0.10	14.4	-0.4
Draco	3.8	38.1	MAGIC	5 – 37	49.5	60 – 10000	0.17	1.0	–
			MAGIC	29 – 45	52.1	70 – 10000	0.22	1.0	–
			VERITAS	25 – 40	49.8	120 – 70000	0.10	9.0	-1.0
Fornax	2.7	–	H.E.S.S.	11 – 25	6.8	230 – 70000	0.10	45.5	-1.5
Hercules	2.8	6.3	–	–	–	–	–	–	–
Leo I	2.5	6.7	–	–	–	–	–	–	–
Leo II	2.6	3.1	–	–	–	–	–	–	–
Leo IV	2.4	19.5	–	–	–	–	–	–	–
Leo V	2.4	–	–	–	–	–	–	–	–
Leo T	2.6	–	–	–	–	–	–	–	–
Sculptor	2.7	–	H.E.S.S.	10 – 46	11.8	200 – 70000	0.10	19.8	-2.2
Segue I	2.5	2.9	MAGIC	13 – 37	158.0	60 – 10000	0.12	1.0	-0.5
			VERITAS	15 – 35	92.0	80 – 50000	0.10	7.6	0.7
Segue II	2.7	–	–	–	–	–	–	–	–
Sextans	2.4	20.6	–	–	–	–	–	–	–
Ursa Major I	3.4	32.9	–	–	–	–	–	–	–
Ursa Major II	4.0	44.1	MAGIC	35 – 45	94.8	120 – 10000	0.30	1.0	-2.1
Ursa Minor	4.1	–	VERITAS	35 – 45	60.4	160 – 93000	0.10	8.4	-0.1

790 S , is estimated by convolving Equation (6.1) with HAWC's energy response and pixel point spread
 791 functions. I then compute the test statistic (TS) with the log-likelihood ratio test,

$$\text{TS} = -2 \ln \left(\frac{\mathcal{L}_0}{\mathcal{L}^{\max}} \right) \quad (6.6)$$

793 where \mathcal{L}_0 is the null hypothesis, or no DM emission, likelihood. \mathcal{L}^{\max} is the best fit signal
 794 hypothesis where $\langle \sigma v \rangle$ maximizes the likelihood. We calculate the likelihood of each source and
 795 model, assuming events are Poisson distributed, with

$$\mathcal{L} = \prod_i \frac{(B_i + S_i)^{N_i} e^{-(B_i + S_i)}}{N_i!} \quad (6.7)$$

796 where S_i is the sum of expected number of signal counts. B_i is the number of background counts
 797 observed. N_i is the total number of counts.

798 I also calculate an upper limit on $\langle \sigma v \rangle$ by calculating the 95% confidence level (CL). For the
 799 CL, we define a parameter, TS_{95} , as

$$\text{TS}_{95} \equiv \sum_{\text{bins}} \left[2N \ln \left(1 + \frac{\epsilon S_{\text{ref}}}{B} \right) - 2\epsilon S_{\text{ref}} \right] \quad (6.8)$$

800 where the expected signal counts from a dSph is scaled by ϵ . S_{ref} is the expected number of excess
 801 counts in a bin from DM emission from a dSph with a corresponding annihilation cross-section,
 802 $\langle \sigma v \rangle$. We scan ϵ such that

$$2.71 = \text{TS}_{\max} - \text{TS}_{95} \quad (6.9)$$

803 6.4.2 Glory Duck Joint Likelihood

804 The joint likelihood for the 5-experiment combination was done similarly as Section 6.4.1. We
 805 calculate upper limits on $\langle \sigma v \rangle$ from the TS, Eq. (6.6), and define the likelihood ratio more generally

$$\lambda(\langle \sigma v \rangle | \mathcal{D}_{\text{dSphs}}) = \frac{\mathcal{L}(\langle \sigma v \rangle; \hat{\nu} | \mathcal{D}_{\text{dSphs}})}{\mathcal{L}(\widehat{\langle \sigma v \rangle}; \hat{\nu} | \mathcal{D}_{\text{dSphs}})} \quad (6.10)$$

806 $\mathcal{D}_{\text{dSphs}}$ is the totality of observations across experiments and dSphs. ν are the nuisance parameters
 807 which are the J factors in this study. $\widehat{\langle \sigma v \rangle}$ and $\hat{\nu}$ are the respective estimate that maximize \mathcal{L}
 808 globally. Finally, $\hat{\nu}$ is the set of nuisance parameters that maximize \mathcal{L} for a fixed value of $\langle \sigma v \rangle$.

809 The *complete* joint likelihood, \mathcal{L} that encompasses all observations from all instruments and
 810 dSphs can be factorized into *partial* functions for each dSph l (with $\mathcal{L}_{\text{dSph},l}$) and its J factor (\mathcal{J}_l):

$$\mathcal{L} (\langle \sigma v \rangle; \nu | \mathcal{D}_{\text{dSphs}}) = \prod_{l=1}^{N_{\text{dSphs}}} \mathcal{L}_{\text{dSph},l} (\langle \sigma v \rangle; J_l, \nu_l | \mathcal{D}_l) \times \mathcal{J}_l (J_l | J_{l,\text{obs}}, \sigma_{\log J_l}). \quad (6.11)$$

811 For this study, $N_{\text{dSphs}} = 20$ is the number of dSphs studied. \mathcal{D}_l are the gamma-ray observations
 812 of dSph, l . ν_l are the nuisance parameters modifying the gamma-ray observations of dSph, l ,
 813 but excludes \mathcal{J}_l . \mathcal{J}_l is the J factor for dSph, l , as defined in Equation (6.2), and it is a nuisance
 814 parameter whose value is unknown. $\log_{10} J_{l,\text{obs}}$ and $\sigma_{\log J_l}$ are obtained from fitting a log-normal
 815 function of $J_{l,\text{obs}}$ to the posterior distribution of J_l [48]. $\log_{10} J_{l,\text{obs}}$ and $\sigma_{\log J_l}$ values are provided
 816 in Table 6.1. The term \mathcal{J}_l constraining J_l is written as:

$$\mathcal{J}_l (J_l | J_{l,\text{obs}}, \sigma_{\log J_l}) = \frac{1}{\ln(10) J_{l,\text{obs}} \sqrt{2\pi} \sigma_{\log J_l}} \exp\left(-\frac{(\log_{10} J_l - \log_{10} J_{l,\text{obs}})^2}{2\sigma_{\log J_l}^2}\right). \quad (6.12)$$

817 Both the \mathcal{GS} and \mathcal{B} , displayed in Table 6.1, sets of J factors are used in this analysis. Equation (6.12)
 818 is also normalized, so it can also be interpreted as a probability density function (PDF) for $J_{l,\text{obs}}$.
 819 From Equation (6.1), we can also see that $\langle \sigma v \rangle$ and J_l are degenerate when computing $\mathcal{L}_{\text{dSph},l}$.
 820 Therefore, as noted in [49], it is sufficient to compute $\mathcal{L}_{\text{dSph},l}$ versus $\langle \sigma v \rangle$ for a fixed value of J_l .
 821 We used $J_{l,\text{obs}}(\mathcal{GS})$ reported in Tab. 6.1, in order to perform the profile of \mathcal{L} with respect to J_l .
 822 The degeneracy implies that for any $J'_l \neq J_{l,\text{obs}}$ (in practice in our case we used $J'_l = J_{l,\text{obs}}(\mathcal{B})$ to
 823 compute results from a different set of J factors):

$$\mathcal{L}_{\text{dSph},l} (\langle \sigma v \rangle; J'_l, \nu_l | \mathcal{D}_l) = \mathcal{L}_{\text{dSph},l} \left(\frac{J'_l}{J_{l,\text{obs}}} \langle \sigma v \rangle; J_{l,\text{obs}}, \nu_l | \mathcal{D}_l \right), \quad (6.13)$$

824 which is a straightforward rescaling operation that reduces the computational needs of the profiling
 825 operation since:

$$\mathcal{L} (\langle \sigma v \rangle; \hat{\nu} | \mathcal{D}_{\text{dSphs}}) = \prod_{l=1}^{N_{\text{dSphs}}} \max_{J_l} \left[\mathcal{L}_{\text{dSph},l} (\langle \sigma v \rangle; J_l, \hat{\nu}_l | \mathcal{D}_l) \times \mathcal{J}_l (J_l | J_{l,\text{obs}}, \sigma_{\log J_l}) \right]. \quad (6.14)$$

826 In addition, Eq. (6.13) enables the combination of data from different gamma-ray instruments and
 827 observed dSphs via tabulated values of $\mathcal{L}_{\text{dSph},l}$, or equivalently of λ from Eq. (6.10) as was done in

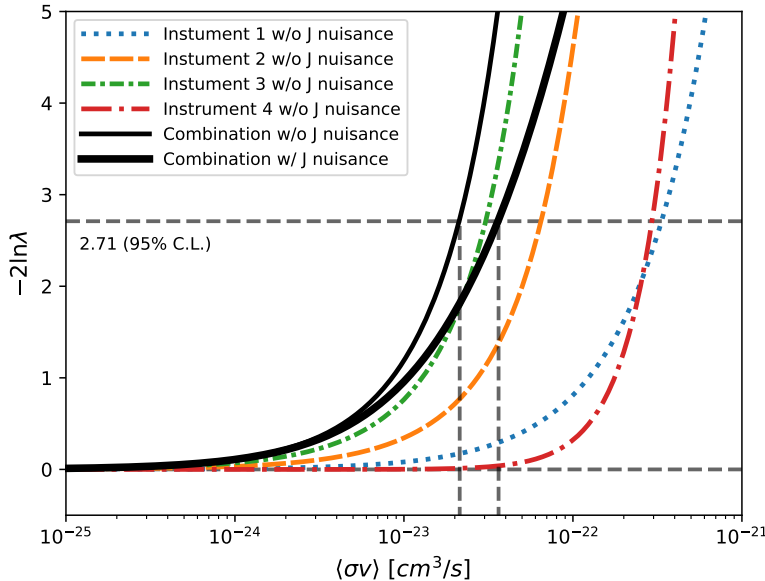


Figure 6.4 Illustration of the combination technique showing a comparison between $-2 \ln \lambda$ provided by four instruments (colored lines) from the observation of the same dSph without any J nuisance and their sum, *i.e.* the resulting combined likelihood (thin black line). According to the test statistics of Equation (6.6), the intersection of the likelihood profiles with the line $-2 \ln \lambda = 2.71$ indicates the 95% C.L. upper limit on $\langle \sigma v \rangle$. The combined likelihood (thin black line) shows a smaller value of upper limit on $\langle \sigma v \rangle$ than those derived by individual instruments. We also show how the uncertainties on the J factor effects the combined likelihood and degrade the upper limit on $\langle \sigma v \rangle$ (thick black line). All likelihood profiles are normalized so that the global minimum $\widehat{\langle \sigma v \rangle}$ is 0. We note that each profile depends on the observational conditions in which a target object was observed. The sensitivity of a given instrument can be degraded and the upper limits less constraining if the observations are performed in non-optimal conditions such as a high zenith angle or a short exposure time.

828 this work, versus $\langle \sigma v \rangle$. $\mathcal{L}_{dSph,l}$ is computed for a fixed value of J_l and profiled with respect to all
 829 instrumental nuisance parameters ν_l , these nuisance parameters are discussed in more detail below.
 830 These values are produced by each detector independently and therefore there is no need to share
 831 sensitive low-level information used to produce them, such as event lists. Figure 6.4 illustrates the
 832 multi-instrument combination technique used in this study with a comparison of the upper limit
 833 on $\langle \sigma v \rangle$ obtained from the combination of the observations of four experiments towards one dSph
 834 versus the upper limit from individual instruments. It also shows graphically the effect of the
 835 J -factor uncertainty on the combined observations.

836 The *partial* joint likelihood function for gamma-ray observations of each dSph ($\mathcal{L}_{dSph,l}$) is

written as the product of the likelihood terms describing the $N_{\text{exp},l}$ observations performed with any of our observatories:

$$\mathcal{L}_{\text{dSph},l} (\langle \sigma v \rangle; J_l, \nu_l | \mathcal{D}_l) = \prod_{k=1}^{N_{\text{exp},l}} \mathcal{L}_{lk} (\langle \sigma v \rangle; J_l, \nu_{lk} | \mathcal{D}_{lk}), \quad (6.15)$$

where each \mathcal{L}_{lk} term refers to an observation of the l -th dSph with associated k -th instrument responses. $N_{\text{exp},l}$ varies from dSph to dSph and can be inferred from Table 6.2.

Each collaboration separately analyzes their data for \mathcal{D}_{lk} corresponding to dSph l and gamma-ray detector k , using as many common assumptions as possible in the analysis. HAWC’s treatment was described earlier in Section 6.4.1 whereas the specifics of the remaining experiments is left to the publication. We compute the values for the likelihood functions \mathcal{L}_{lk} (see Eq. (6.15)) for a fixed value of J_l and profile over the rest of the nuisance parameters ν_{lk} . Then, values of λ from Eq. (6.10) are computed as a function of $\langle \sigma v \rangle$, and shared using a common format. Results are computed for seven annihilation channels, W^+W^- , ZZ , $b\bar{b}$, $t\bar{t}$, e^+e^- , $\mu^+\mu^-$, and $\tau^+\tau^-$ over 62 m_χ values between 5 GeV and 100 TeV provided in [44]. The $\langle \sigma v \rangle$ range is defined between 10^{-28} and $10^{-18} \text{cm}^3 \cdot \text{s}^{-1}$, with 1001 logarithmically spaced values. The likelihood combination, i.e. Equation (6.11), and profile over the J -factor to compute the profile likelihood ratio λ , Equation (6.10), are carried out with two different public analysis software packages, namely `gLike` [50] and `LklCom` [51], that provide the same results [52].

As mentioned previously, each experiment computes the \mathcal{L}_{lk} from Equation (6.10) differently. The remainder of this section highlights the differences in this calculation across the experiments. Four experiments, namely *Fermi*-LAT, H.E.S.S., HAWC and MAGIC, use a binned likelihood to compute the \mathcal{L}_{lk} . For these experiments, for each observation \mathcal{D}_{lk} of a given dSph l carried out using a given gamma-ray detector k , the binned likelihood function is:

$$\mathcal{L}_{lk} (\langle \sigma v \rangle; J_l, \nu_{lk} | \mathcal{D}_{lk}) = \prod_{i=1}^{N_E} \prod_{j=1}^{N_P} \left[\mathcal{P}(s_{lk,ij}(\langle \sigma v \rangle, J_l, \nu_{lk}) + b_{lk,ij}(\nu_{lk}) | N_{lk,ij}) \right] \times \mathcal{L}_{lk,\nu} (\nu_{lk} | \mathcal{D}_{\nu_{lk}}) \quad (6.16)$$

where N_E and N_P are the number of considered bins in reconstructed energy and arrival direction, respectively; \mathcal{P} represents a Poisson PDF for the number of gamma-ray candidate events $N_{lk,ij}$

860 observed in the i -th bin in energy and j -th bin in arrival direction, when the expected number is
 861 the sum of the expected mean number of signal events s_{ij} (produced by DM annihilation) and of
 862 background events b_{ij} ; $\mathcal{L}_{lk,\nu}$ is the likelihood term for the extra ν_{lk} nuisance parameters that vary
 863 from one instrument k to another. The expected counts for signal events s_{ij} for a given dSph l and
 864 detector k is given by:

$$s_{ij}(\langle\sigma\nu\rangle, J) = \int_{E'_{\min,i}}^{E'_{\max,i}} dE' \int_{P'_{\min,j}}^{P'_{\max,j}} d\Omega' \int_0^\infty dE \int_{\Delta\Omega_{tot}} d\Omega \int_0^{T_{\text{obs}}} dt \frac{d^2\Phi(\langle\sigma\nu\rangle, J)}{dEd\Omega} \text{IRF}(E', P' | E, P, t) \quad (6.17)$$

865 where E' and E are the reconstructed and true energies, P' and P the reconstructed and true
 866 arrival directions; $E'_{\min,i}$, $P'_{\min,j}$, $E'_{\max,i}$, and $P'_{\max,j}$ are their lower and upper limits of the i -th
 867 energy bin and the j -th arrival direction bin; T_{obs} is the (dead-time corrected) total observation
 868 time; t is the time along the observations; $d^2\Phi/dEd\Omega$ is the DM flux in the source region (see
 869 Equation (6.1)); and $\text{IRF}(E', P' | E, P, t)$ is the IRF, which can be factorized as the product of the
 870 effective collection area of the detector $A_{\text{eff}}(E, P, t)$, the PDFs for the energy estimator $f_E(E' | E, t)$,
 871 and arrival direction $f_P(P' | E, P, t)$ estimators. Note that for Fermi-LAT, HAWC, MAGIC, and
 872 VERITAS the effect of the finite angular resolution is taken into account through the convolution
 873 of $d\Phi/dEd\Omega$ with f_P in Equation (6.17), whereas in the cases of H.E.S.S. f_P is approximated by a
 874 delta function. This approximation has been made in order to maintain compatibility of the result
 875 with what has been previously published. The difference introduced by this approximation is $< 5\%$
 876 for all considered dSphs. A more comprehensive review of the differences between the analyses of
 877 different instruments can be found in [25].

878 6.5 HAWC Results

879 13 of the 20 dSphs considered for the Glory Duck analysis are within HAWC's field of view.
 880 These dSph are analyzed for emission from DM annihilation according to the likelihood method
 881 described in Section 6.4. The 13 likelihood profiles are then stacked to synthesize a combined
 882 limit on the dark matter cross-section, $\langle\sigma\nu\rangle$. This combination is done for the 7 SM annihilation
 883 channels used in the Glory Duck analysis. Figure 6.5 shows the combined limit for all annihilation
 884 channels with HAWC only observations. We also perform 300 studies of Poisson trials on the

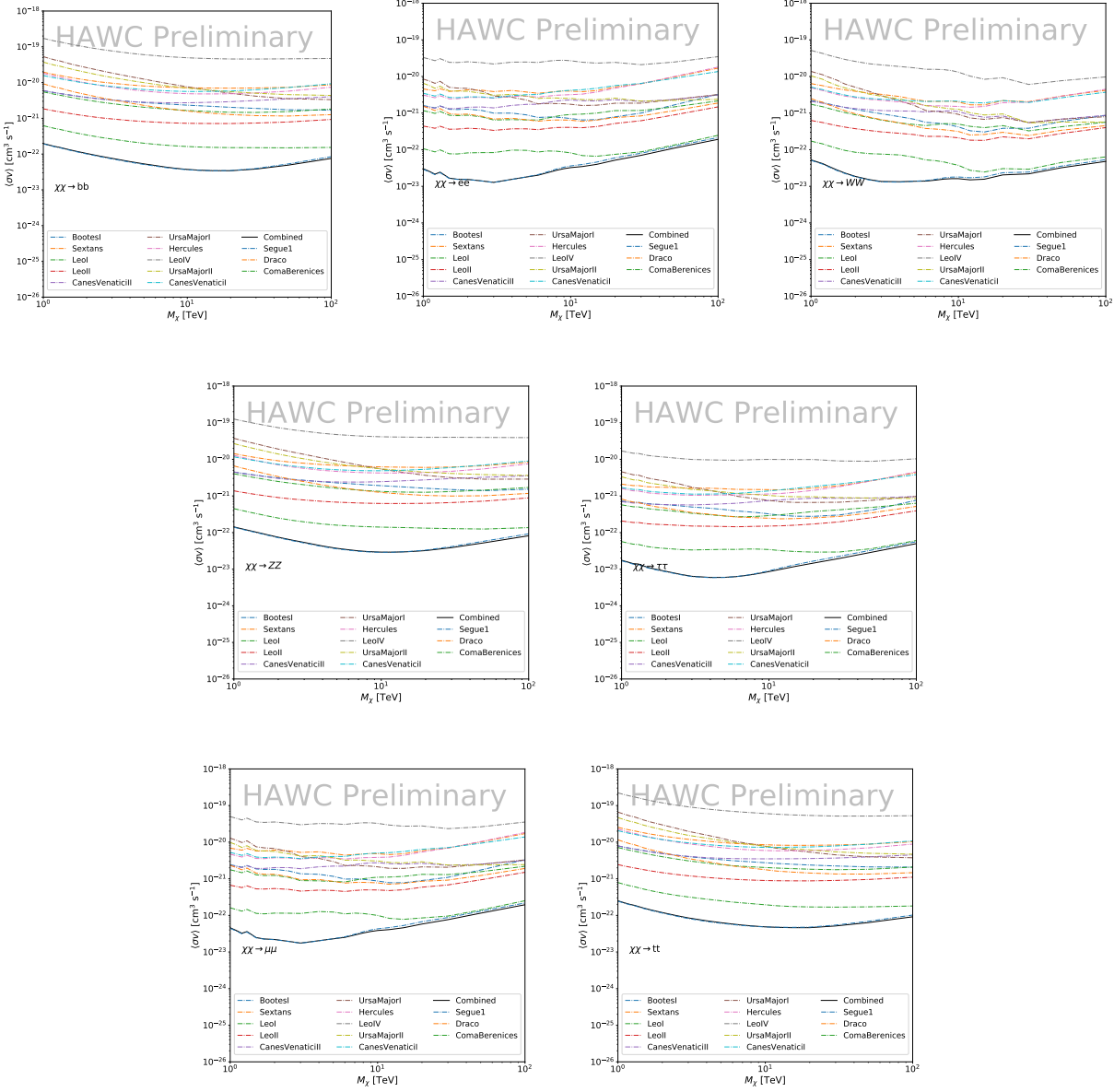


Figure 6.5 HAWC upper limits at 95% confidence level on $\langle\sigma v\rangle$ versus DM mass for seven annihilation channels, using the set of J -factors from Ref. [53]. The solid line represents the observed combined limit. Dashed lines represent limits from individual dSphs.

background. These trials are used to produce HAWC Brazil bands which were shared with the other collaborators for combined Brazil Bands. The results on fitting to HAWC's Poisson trials of the DM hypothesis is shown in Figure 6.7 for all the DM annihilation channels studied for Glory Duck.

No DM was found in HAWC observations. HAWC's limits are dominated by the dSphs Segue1

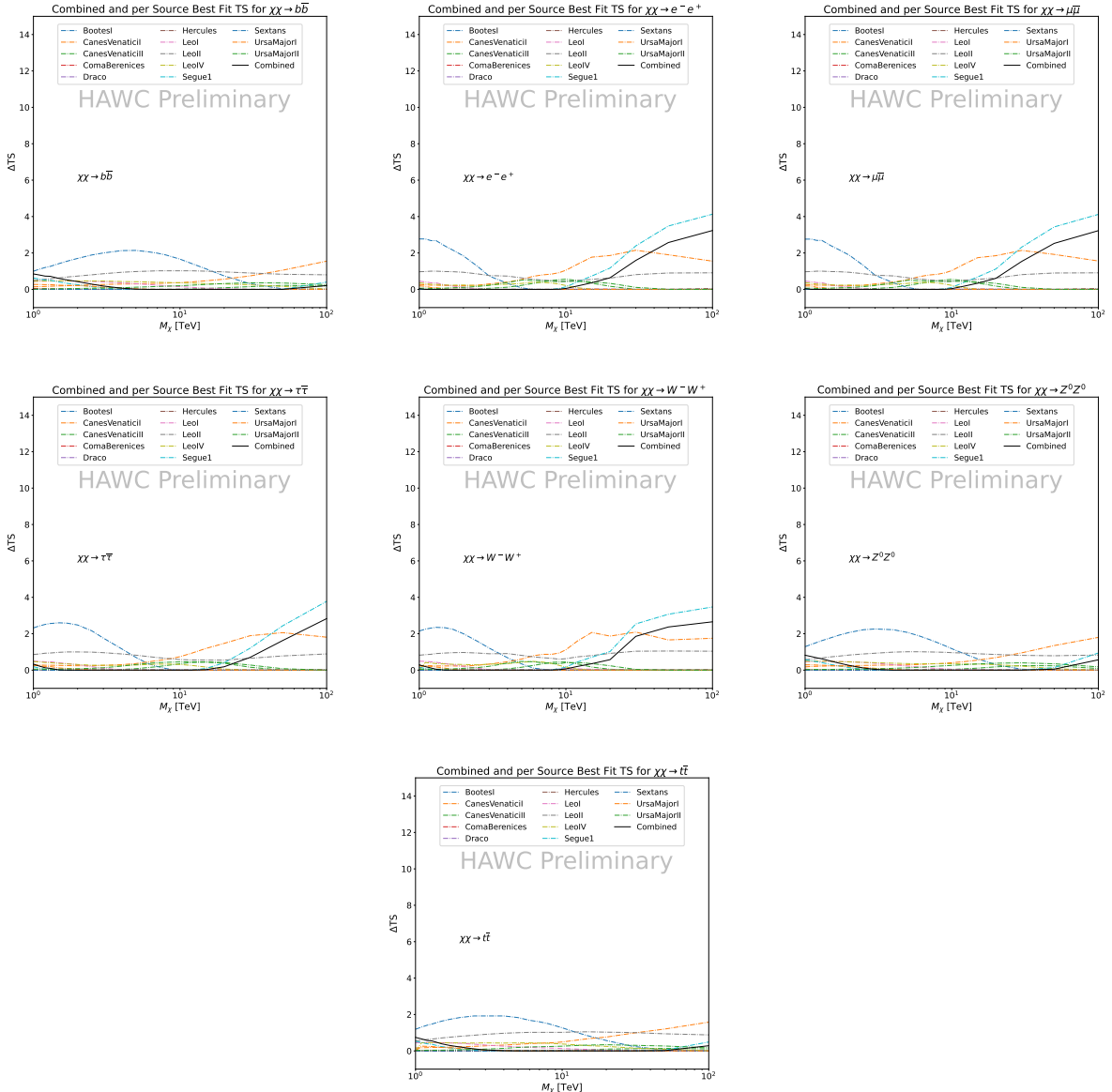


Figure 6.6 HAWC TS values for best fit $\langle \sigma v \rangle$ versus m_χ for seven SM annihilation channels with J factors from \mathcal{GS} . The solid black line shows the combined best fit TS values. The colored, dashed lines are the TS values for each of the 13 sources HAWC studied.

and Coma Berenices. The remaining 11 dSphs do not contribute significantly to the limit because they are at high zenith and/or have much smaller J factors. Even though some remaining dSphs have large J factors, they are towards the edge of HAWC's field of view where HAWC analysis is less sensitive.

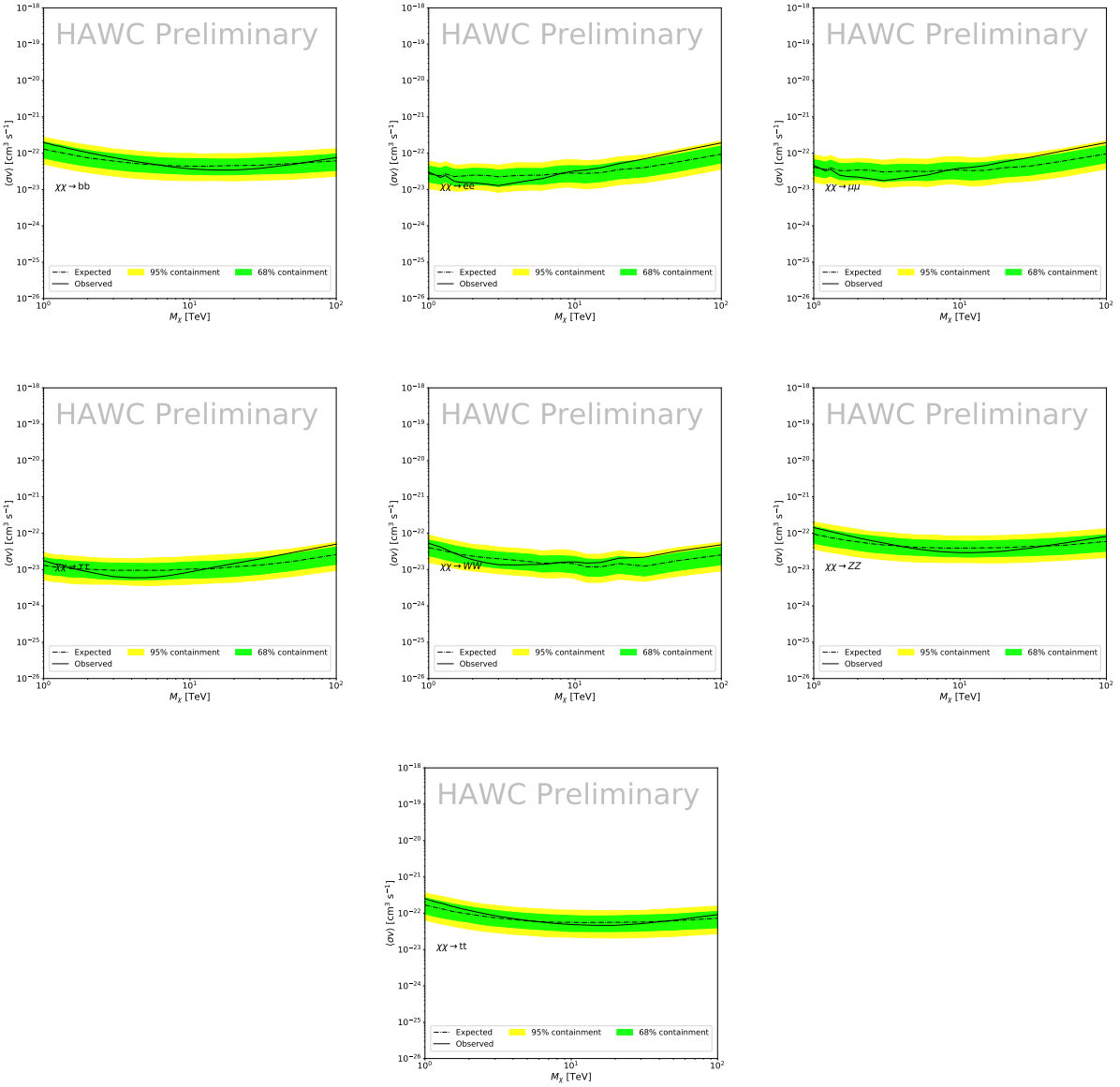


Figure 6.7 HAWC Brazil bands at 95% confidence level on $\langle\sigma v\rangle$ versus DM mass for seven annihilation channels with J -factors from \mathcal{GS} [53]. The solid line represents the combined limit from 13 dSphs. The dashed line is the expected limit. The green band is the 68% containment. The yellow band is the 95% containment.

894 6.6 Glory Duck Combined Results

895 The crux of this analysis is that HAWC's results are combined with 4 other gamma-ray observa-
 896 tories: Fermi-LAT, H.E.S.S., MAGIC, and VERITAS. No significant DM emission was observed
 897 by any of the five instruments. We present the upper limits on $\langle\sigma v\rangle$ assuming seven independent
 898 DM self annihilation channels, namely W^+W^- , Z^+Z^- , $b\bar{b}$, $t\bar{t}$, e^+e^- , $\mu^+\mu^-$, and $\tau^+\tau^-$. The 68%

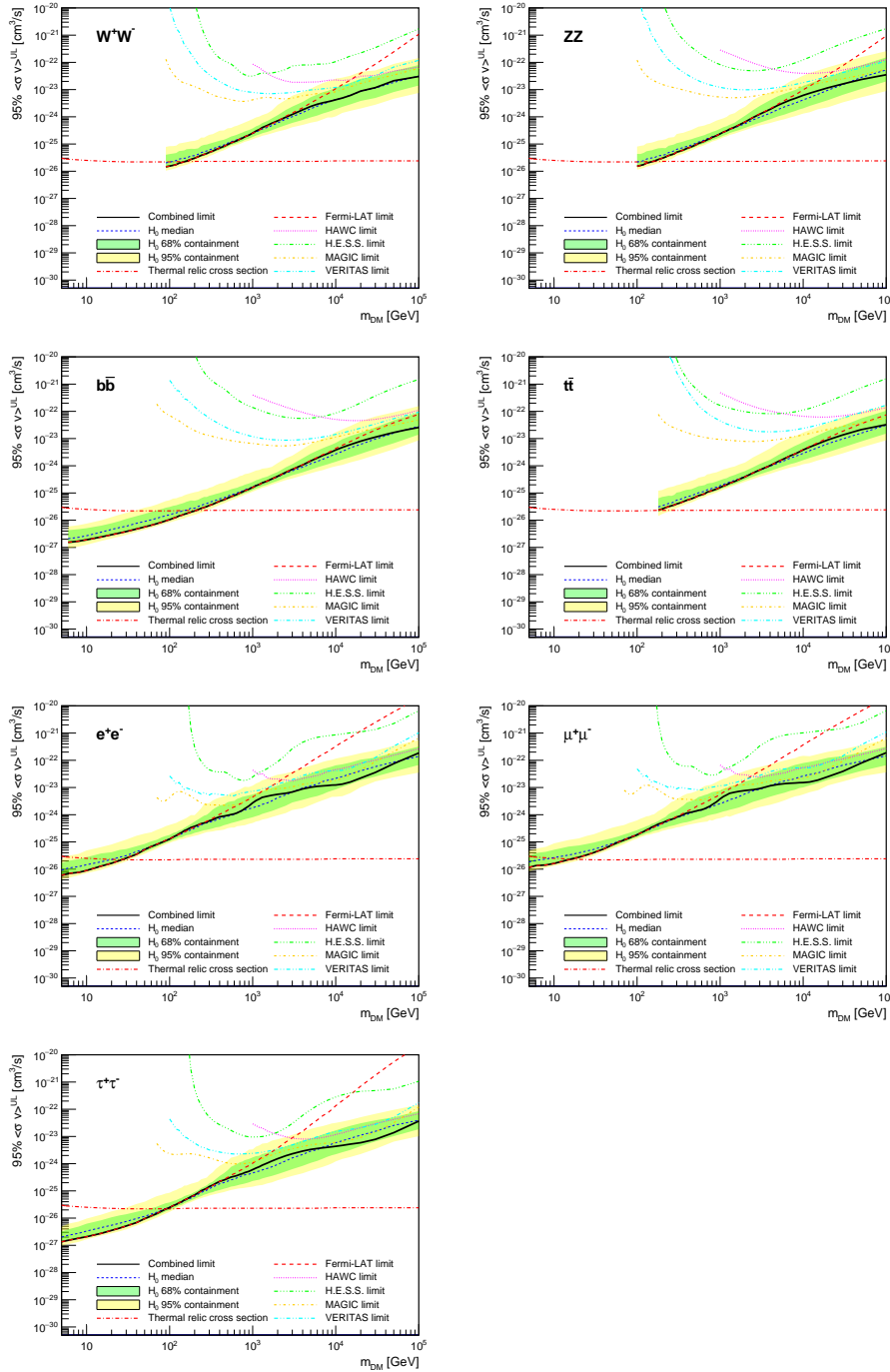


Figure 6.8 Upper limits at 95% confidence level on $\langle\sigma v\rangle$ in function of the DM mass for eight annihilation channels, using the set of J factors from Ref. [53] (\mathcal{GS} set in Table 6.1). The black solid line represents the observed combined limit, the black dashed line is the median of the null hypothesis corresponding to the expected limit, while the green and yellow bands show the 68% and 95% containment bands. Combined upper limits for each individual detector are also indicated as solid, colored lines. The value of the thermal relic cross-section in function of the DM mass is given as the red dotted-dashed line [54].

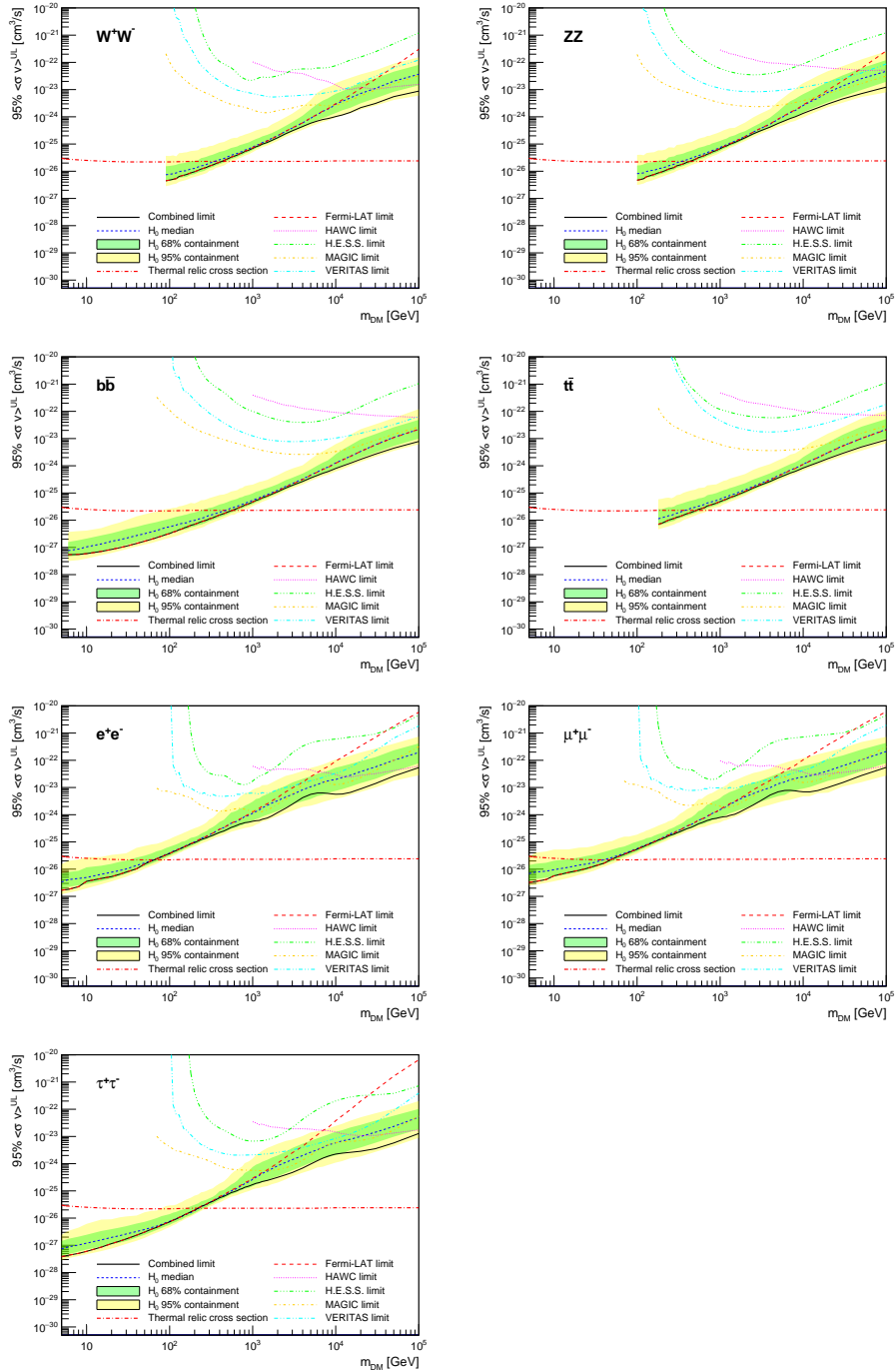


Figure 6.9 Same as Fig. 6.8, using the set of J factors from Ref. [47, 55] (\mathcal{B} set in Table 6.1).

and 95% containment bands are produced from 300 Poisson realizations of the null hypothesis corresponding to each of the combined datasets. These 300 realizations are combined identically to dSph observations. The containment bands and the median are extracted from the distribution of resulting limits on the null hypothesis. These 300 realizations are obtained either by fast simu-

903 lations of the OFF observations, for H.E.S.S., MAGIC, VERITAS, and HAWC, or taken from real
904 observations of empty fields of view in the case of Fermi-LAT [48, 56, 57].

905 The obtained limits are shown in Figure 6.8 for the $\mathcal{G}\mathcal{S}$ set of J -factors [53] and in Figure 6.9
906 for the \mathcal{B} set of J -factors [47, 55]. The combined limits are presented with their 68% and 95%
907 containment bands, and are expected to be close to the median limit when no signal is present.
908 We observe agreement with the null hypothesis for all channels, within 2σ standard deviations,
909 between the observed limits and the expectations given by the median limits. Limits obtained from
910 each detector are also indicated in the figures, where limits for all dSphs observed by the specific
911 instrument have been combined.

912 Below ~ 300 GeV, the *Fermi*-LAT dominates the DM limits for all annihilation channels. From
913 ~ 300 GeV to ~ 2 TeV, *Fermi*-LAT continues to dominate for the hadronic and bosonic DM channels,
914 yet the IACTs (H.E.S.S., MAGIC, and VERITAS) and *Fermi*-LAT all contribute to the limit for
915 leptonic DM channels. For DM masses between ~ 2 TeV to ~ 10 TeV, the IACTs dominate leptonic
916 DM annihilation channels, whereas both the *Fermi*-LAT and the IACTs dominate bosonic and
917 hadronic DM annihilation channels. From ~ 10 TeV to ~ 100 TeV, both the IACTs and HAWC
918 contribute significantly to the leptonic DM limit. For hadronic and bosonic DM, the IACTs and
919 *Fermi*-LAT both contribute strongly.

920 We notice that the limits computed using the \mathcal{B} set of J -factor are always better compared to the
921 ones calculated with the $\mathcal{G}\mathcal{S}$ set. For the W^+W^- , Z^+Z^- , $b\bar{b}$, and $t\bar{t}$ channels, the ratio between the
922 limits computed with the two sets of J -factor is varying between a factor of ~ 3 and ~ 5 depending
923 on the energy, with the largest ratio around 10 TeV. For the channels e^+e^- , $\mu^+\mu^-$, and $\tau^+\tau^-$, the
924 ratio lies between ~ 2 to ~ 6 , being maximum around 1 TeV. Examining Figure 6.16 and Figure 6.17
925 in Section 6.8, these differences are explained by the fact that the \mathcal{B} set provides higher J -factors
926 for the majority of the studied dSphs, with the notable exception of Segue I. The variation on the
927 ratio of the limits for the two sets is due to different dSph dominating the limits depending on the
928 energy. This pushes the range of thermal cross-section which can be excluded to higher mass. This
929 comparison demonstrates the magnitude of systematic uncertainties associated with the choice of

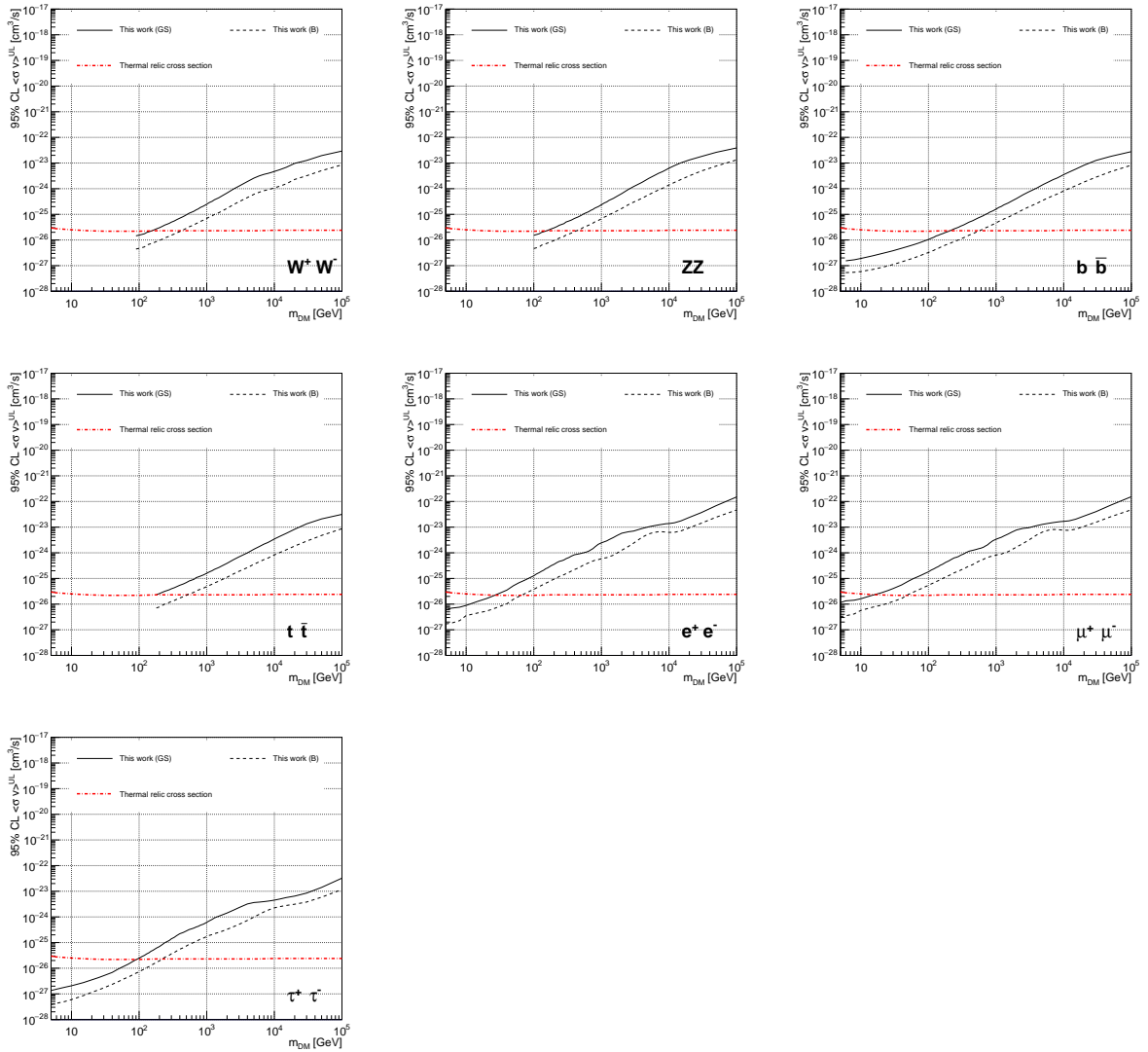


Figure 6.10 Comparisons of the combined limits at 95% confidence level for each of the eight annihilation channels when using the J factors from Ref. [53] (\mathcal{GS} set in Table 6.1), plain lines, and the J factor from Ref. [47, 55] (\mathcal{B} set in Table 6.1), dashed lines. The cross-section given by the thermal relic is also indicated [54].

930 the J -factor

931 This comparison demonstrates the magnitude of systematic uncertainties associated with the
 932 choice of the J -factor calculation. The \mathcal{GS} and \mathcal{B} sets present a difference in the limits for all
 933 channels of about This difference is explained, see Figure 6.16 and Figure 6.17 in Appendix, by the
 934 fact that the \mathcal{B} set provides higher J factors for all dSph except for Segue I. This pushes the range
 935 of thermal cross-section which can be excluded to higher mass.

936 **6.7 HAWC Systematics**

937 **6.7.1 Inverse Compton Scattering**

938 The DM-DM annihilation channels produce many high energy electrons regardless of the
939 primary annihilation channel. These high energy electrons can produce high energy gamma-rays
940 through Inverse Compton Scattering (ICS). If this effect is strong, it would change the morphology
941 of the source and increase the total expected gamma-ray counts from any source. The PPPC [44]
942 provides tools in Mathematica for calculating the impact of ICS for an arbitrary location in the
943 sky for a specified annihilation channel. We calculated the change in gamma-ray counts for DM
944 annihilation to primary $e\bar{e}$ for RA and Dec corresponding to Segue1 and Coma Berenices. These
945 dSphs were chosen because they are the strongest contributors to the limit. $e\bar{e}$ was selected because
946 it would have the largest number of high energy electrons. The effect was found to be on the order
947 of 10^{-7} on the gamma-ray spectrum. As a result, this systematic is not considered in our analysis.

948 **6.7.2 Point Source Versus Extended Source Limits**

949 The previous DM search toward dSph approximated the dSphs as point sources [46]. In
950 this analysis, the dSphs are implemented as extended with J-factor distributions following those
951 produced by [53]. The resolution of the cited map is much finer than HAWC's angular resolution.
952 The vast majority of the J-factor distribution is represented on the central HAWC pixel of the dSph
953 spatial map. However, the neighboring 8 pixels are not negligible and contribute to our limit.

954 Figure 6.11 shows a substantial improvement to the limit for Segue1. Fig. 6.12 however showed
955 identical limits. These disparities are best explained by the relative difference in their J-Factors.
956 Both dSphs pass almost overhead the HAWC detector, however Segue1 has the larger J-Factor
957 between the two. Adjacent pixels to the central pixel will therefore contribute to the limits. This is
958 the case for other dSph that are closer to overhead the HAWC detector.

959 Comparison plots for all sources and the combined limit can be found in the sandbox for the
960 Glory Duck project.

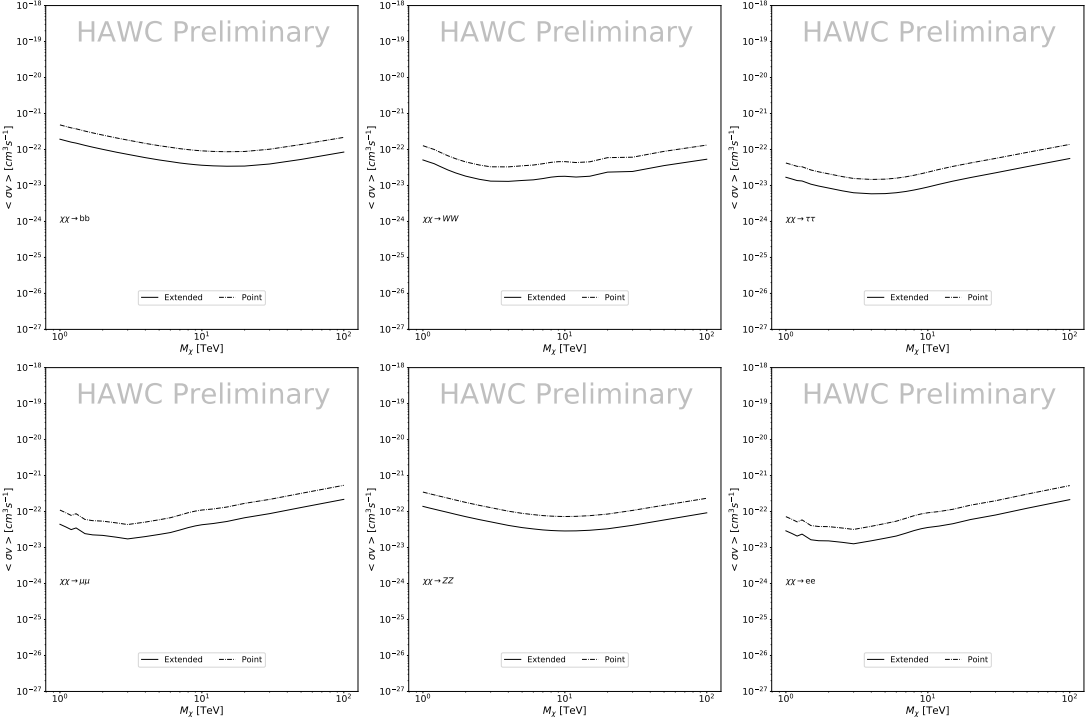


Figure 6.11 Comparisons of the combined limits at 95% confidence level for a point source analysis and extended source using [53] \mathcal{GS} J-factor distributions and PPPC [44] annihilation spectra. Shown are the limits for Segue1 which will have the most significant impact on the combined limit. 6 of the 7 DM annihilation channels are shown. Solid lines are extended source studies. Dashed lines are point source studies. Overall, the extended source analysis improves the limit by a factor of 2.

6.7.3 Impact of Pointing Systematic

During the analysis it was discovered that reconstruction of gamma-rays. Slides describing this systematic can be found [here](#). Shown on the presentation is dependence on the pointing systematic on declination. New spatial profiles were generated for every dSph and limits were computed for the adjusted declination.

Section 6.7.3 demonstrates the impact of this systematic for all DM annihilation channels studied by HAWC. The impact is a tiny improvement, yet mostly identical, to the combined limits.

6.8 J-factor distributions

6.8.1 Numerical integration of \mathcal{GS} maps

It was discovered well after the HAWC analysis was completed that the published tables from \mathcal{GS} [45] quoted median J-factors were computed in a non-trivial manner. The assumption myself

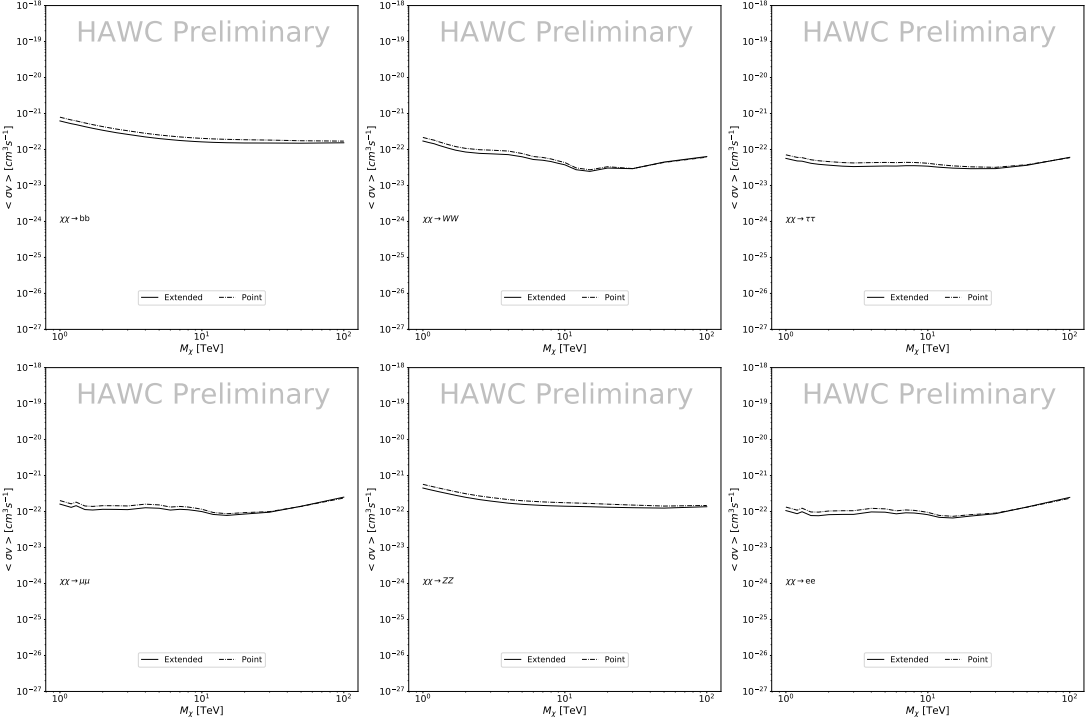


Figure 6.12 Same as Fig. 6.11 on Coma Berenices. This dSph also contributes significantly to the limit. The limits are identical in this case.

and collaborators had been that the published tables represented the J -factor as a function of θ for the best global fit model on a per-source basis. However, this is not the case. Instead, what is published are the best fit model for each dwarf that only considers stars up to the angular separation θ . Therefore, the model is changing for each value of θ for each dwarf. Yet, the introduced features from unique models at each θ are much smaller than the angular resolution of HAWC. It is not expected for these effects to impact the limits and TS greatly as a result.

Median J -factor model profiles were provided by the authors. New maps were generated and analyzed for Segue1 and Coma Berenices. Figure 6.14 shows the differential between maps generated with the method from Section 6.8.1 and from the authors of [45]. These maps were reanalyzed for all SM DM annihilation channels. Upper limits for these channels are shown in Figure 6.15

From Figure 6.15, we can see that the impact of these model difference was no substantial. The observed impact was a fractional effect which is much smaller than the impact from selecting another DM spatial distribution model as was shown in Figure 6.10.

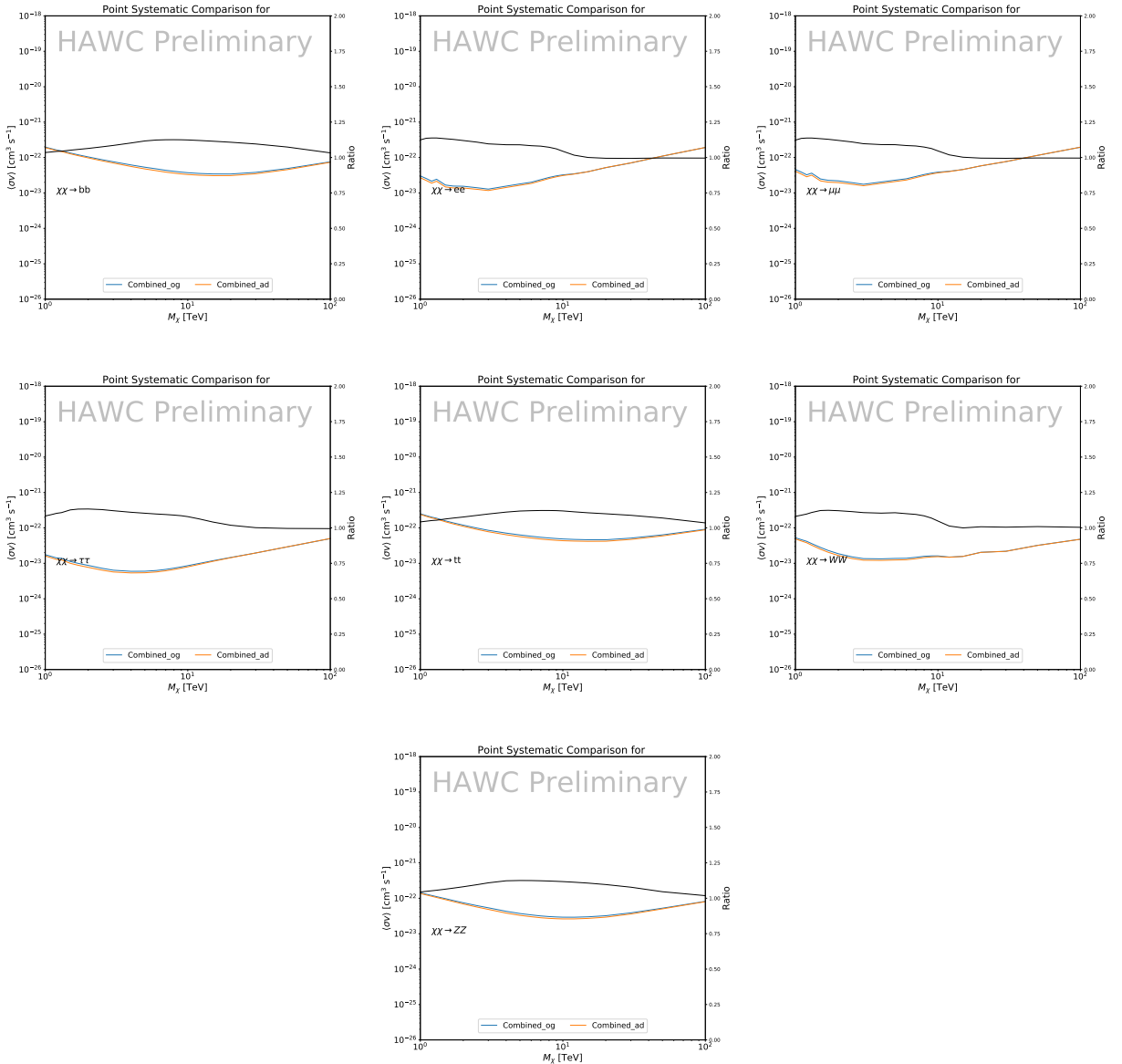


Figure 6.13 Comparison of combined limits when correcting for HAWC's pointing systematic. All DM annihilation channels are shown. The solid black line is the ratio between published limit to the declination corrected limit. The blue solid line or "Combined_og" represented the limits computed for Glory Duck. The solid orange line or "Combined_ad" represented the limits computed after correcting for the pointing systematic.

986 6.8.2 $\mathcal{G}\mathcal{S}$ Versus \mathcal{B} spatial models

987 We show in this appendix a comparison between the J -factors computed by Geringer-Sameth
 988 *et al.* [53] (the $\mathcal{G}\mathcal{S}$ set) and the ones computed by Bonnivard *et al.* [47, 55] (the \mathcal{B} set). The
 989 $\mathcal{G}\mathcal{S}$ J -factors are computed through a Jeans analysis of the kinematic stellar data of the selected

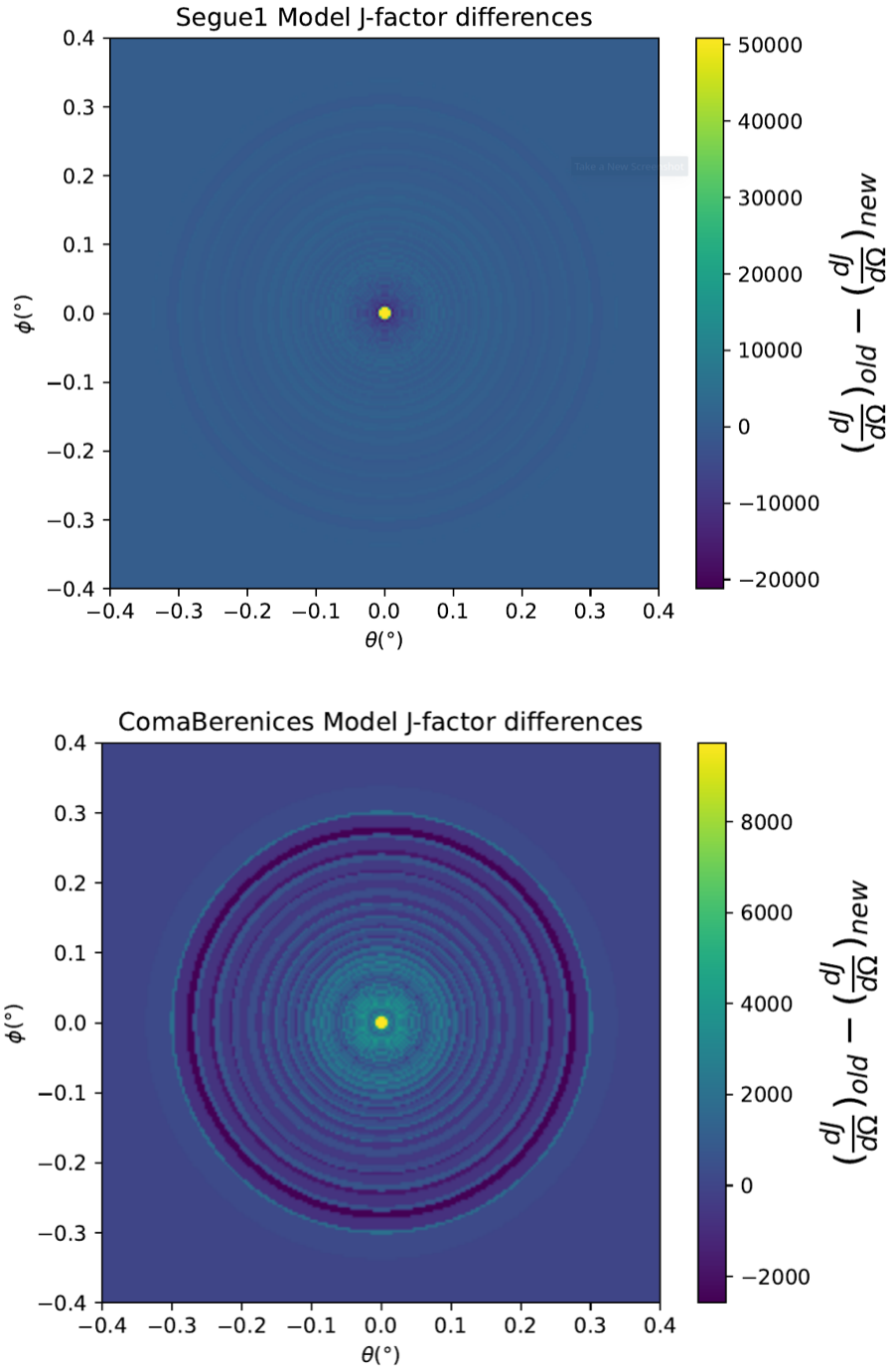


Figure 6.14 Differential map of dJ/Ω from model built in Section 6.8.1 and profiles provided directly from authors. (Top) Differential from Segue1. (bottom) Differential from Coma Berenices. Note that their scales are not the same. Segue1 shows the deepest discrepancies which is congruent with its large uncertainties. Both models show anuli where unique models become apparent.

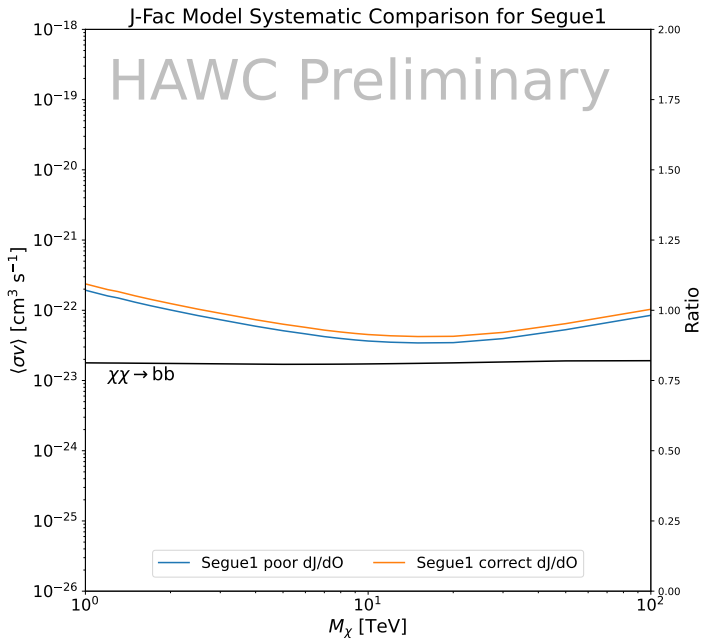
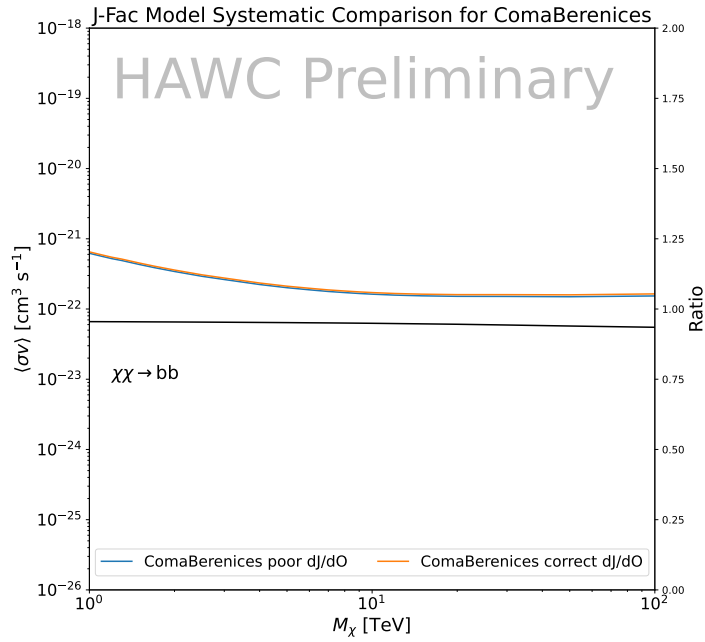


Figure 6.15 HAWC limits for Coma Berenices (top) and Segue1 (bottom) for two different map sets. Blue lines are limits calculated on maps with poor model representation. Orange lines are limits calculated on spatial profiles provided by the authors of [45]. Black line is the ratio of the poor spatial model limits to the corrected spatial models. The left y-axis measures $\langle \sigma v \rangle$ for the blue and orange lines. The right y-axis measures the ratio and is unitless.

990 dSphs, assuming a dynamic equilibrium and a spherical symmetry for the dSphs. They adopted
991 the generalized DM density distribution, known as Zhao-Hernquist, introduced by [58], carrying
992 three additional index parameters to describe the inner and outer slopes, and the break of the
993 density profile. Such a profile parametrization allows the reduction of the theoretical bias from
994 the choice of a specific radial dependency on the kinematic data. In other words, the increase of
995 free parameters with the use of the Zhao-Hernquist profile allows a better description of the mass
996 density distribution of dark matter.

997 In addition, a constant velocity anisotropy profile and a Plummer light profile [59] for the stellar
998 distribution were assumed. The velocity anisotropy profile depends on the radial and tangential
999 velocity dispersion. However, its determination remains challenging since only the line-of-sight
1000 velocity dispersion can be derived from velocity measurements. Therefore, the parametrization of
1001 the anisotropy profile is obtained from simulated halos (see [60] for more details). They provide the
1002 values of the J -factors of regions extending to various angular radius up to the outermost member
1003 star.

1004 The \mathcal{B} J -factors were computed through a Jeans analysis taking into account the systematic
1005 uncertainties induced by the DM profile parametrization, the radial velocity anisotropy profile, and
1006 the triaxiality of the halo of the dwarf galaxies. They performed a more complete study of the dSph
1007 kinematics and dynamics than \mathcal{GS} for the determination of the J -factor. Conservative values of the
1008 J -factors where obtained using an Einasto DM density profile [61], a realistic anisotropy profile
1009 known as the Baes & Van Hese profile [62] which takes into account that the inner regions can be
1010 significantly non-isotropic, and a Zhao-Hernquist light profile [58].

1011 For both sets, J -factor values are provided for all dSphs as a function of the radius of the
1012 integration region [53, 47, 55]. Table 6.1 shows the heliocentric distance and Galactic coordinates
1013 of the twenty dSphs, together with the two sets of J -factor values integrated up to the outermost
1014 observed star for \mathcal{GS} and the tidal radius for \mathcal{B} . Both J -factor sets were derived through a Jeans
1015 analysis based on the same kinematic data, except for Draco where the measurements of [63] have
1016 been adopted in the computation of the \mathcal{B} value. The computations for producing the \mathcal{GS} and \mathcal{B}

1017 samples differ in the choice of the DM density, velocity anisotropy, and light profiles, for which the
1018 set \mathcal{B} takes into account some sources of systematic uncertainties.

1019 Figure 6.16 and Figure 6.17 show the comparisons for the J -factor versus the angular radius
1020 for each of the 20 dSphs used in this study. The uncertainties provided by the authors are also
1021 indicated in the figures. For the \mathcal{GS} set, the computation stops at the angular radius corresponding
1022 to the outermost observed star, while for the \mathcal{B} set, the computation stops at the angular radius
1023 corresponding to the tidal radius.

1024 6.9 Discussion and Conclusions

1025 In this multi-instrument analysis, we have used observations of 20 dSphs from the gamma-ray
1026 telescopes Fermi-LAT, H.E.S.S., MAGIC, VERITAS, and HAWC to perform a collective DM
1027 search annihilation signals. The data were combined across sources and detectors to significantly
1028 increase the sensitivity of the search. We have observed no significant deviation from the null, no
1029 DM hypothesis, and so present our results in terms of upper limits on the annihilation cross-section
1030 for seven potential DM annihilation channels.

1031 Fermi-LAT brings the most stringent constraints for continuum channels below approximately
1032 1 TeV. The remaining detectors dominate at higher energies. Overall, for multi-TeV DM mass,
1033 the combined DM constraints from all five telescopes are 2-3 times stronger than any individual
1034 telescope for multi-TeV DM.

1035 Derived from observations of many dSphs, our results produce robust limits given the DM
1036 content of the dSphs is relatively well constrained. The obtained limits span the largest mass
1037 range of any WIMP DM search. Our combined analysis improves the sensitivity over previously
1038 published results from each detector which produces the most stringent limits on DM annihilation
1039 from dSphs. These results are based on deep exposures of the most promising known dSphs with
1040 the currently most sensitive gamma-ray instruments. Therefore, our results constitute a legacy of
1041 a generation of gamma-ray instruments on WIMP DM searches towards dSphs. Our results will
1042 remain the reference in the field until a new generation of more sensitive gamma-ray instruments
1043 begin operations, or until new dSphs with higher J -factors are discovered.

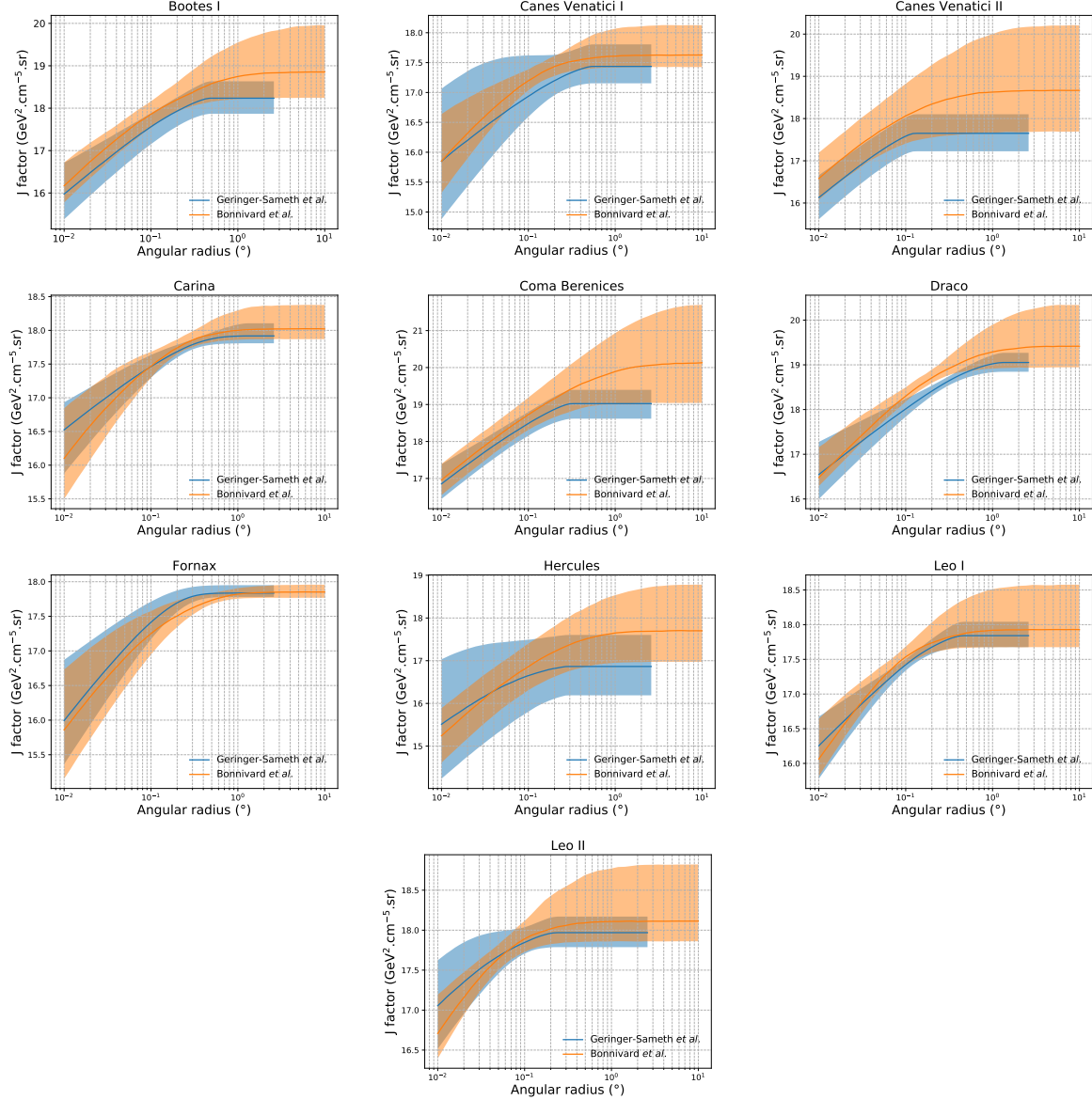


Figure 6.16 Comparisons between the J -factors versus the angular radius for the computation of J factors from Ref. [53] (\mathcal{GS} set in Table 6.1) in blue and for the computation from Ref. [47, 55] (\mathcal{B} set in Tab. 6.1) in orange. The solid lines represent the central value of the J -factors while the shaded regions correspond to the 1σ standard deviation.

This analysis serves as a proof of concept for future multi-instrument and multi-messenger combination analyses. With this collaborative effort, we have managed to sample over four orders in magnitude in gamma-ray energies with distinct observational techniques. Determining the nature of DM continues to be an elusive and difficult problem. Larger datasets with diverse measurement techniques could be essential to tackling the DM problem. A future collaboration using similar

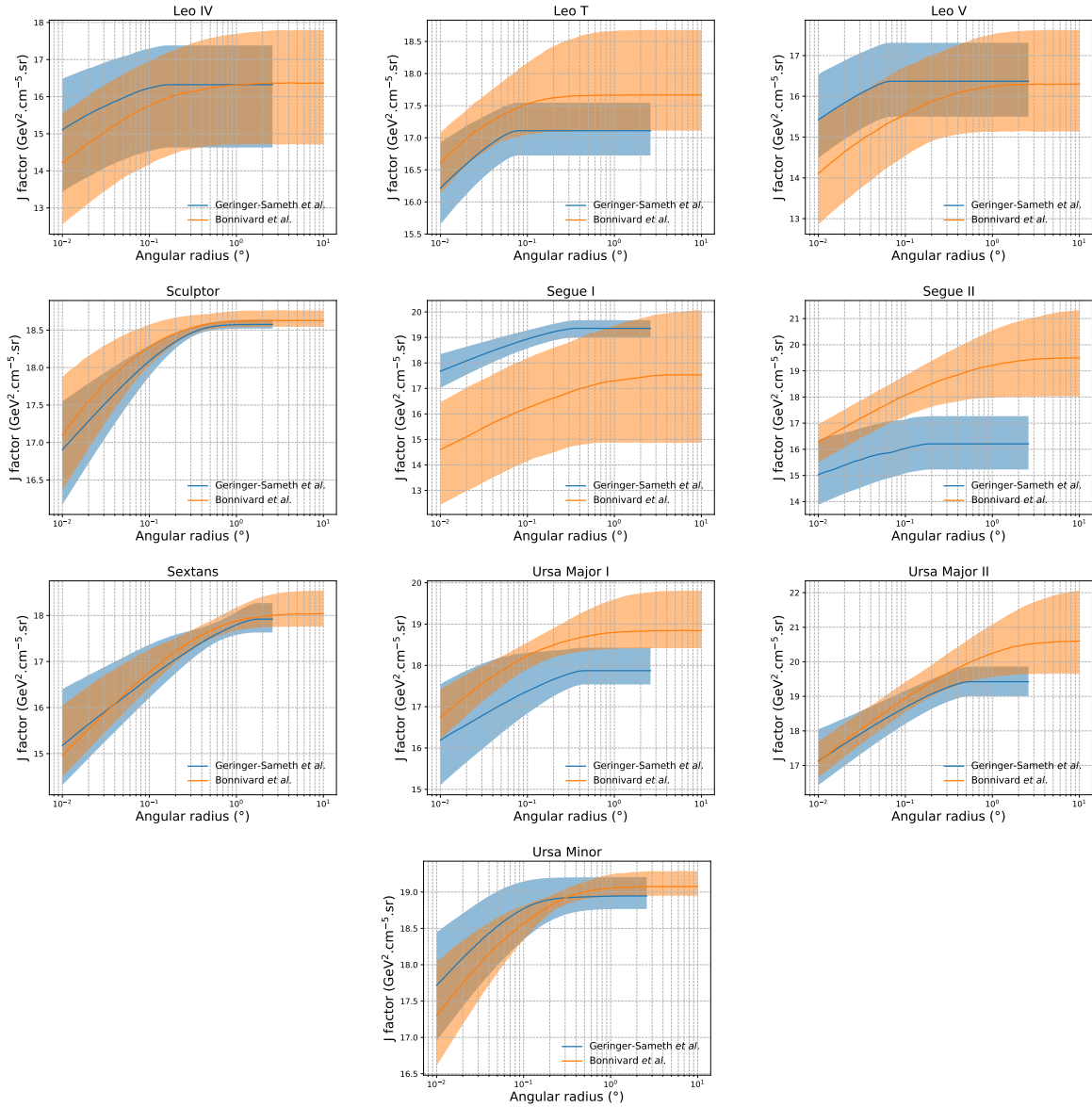


Figure 6.17 Comparisons between the J -factors versus the angular radius for the computation of J factors from Ref. [53] (\mathcal{GS} set in Tab. 6.1) in blue and for the computation from Ref. [47, 55] (\mathcal{B} set in Tab. 6.1) in orange. The solid lines represent the central value of the J -factors while the shaded regions correspond to the 1σ standard deviation.

1049 techniques as the ones described in this paper could grow even beyond gamma rays. The models we
 1050 used for this study include annihilation channels with neutrinos in the final state. Advanced studies
 1051 could aim to merge our results with those from neutrino observatories with large data sets. Efforts
 1052 are already underway to add data from the IceCube, ANTARES, and KM3NeT observatories to
 1053 these gamma-ray results.

1054 From this work, a selection of the best candidates for observations, according to the latest
1055 knowledge on stellar dynamics and modelling techniques for the derivation of the J -factors on
1056 the potential dSphs targets, is highly desirable at the time that new experiments are starting their
1057 dark matter programs using dSphs. Given the systematic uncertainty inherent to the derivation of
1058 the J -factors, an informed observational strategy would be to select both objects with the highest
1059 J -factors that could lead to DM signal detection, and objects with robust J -factor predictions, i.e.
1060 with kinematic measurements on many bright stars, which would strengthen the DM interpretation
1061 reliability of the observation outcome.

1062 This analysis combines data from multiple telescopes to produce strong constraints on astro-
1063 physical objects. From this perspective, these methods can be applied beyond just DM searches.
1064 Almost every astrophysical study can benefit from multi-telescope, multi-wavelength gamma-ray
1065 studies. We have enabled these telescopes to study the cosmos with greater precision and detail.
1066 Many astrophysical searches can benefit from multi-instrument gamma-ray studies, for which our
1067 analysis lays the foundation.

CHAPTER 7

1068 MULTITHREADING HAWC ANALYSES FOR DARK MATTER SEARCHES

1069 7.1 Introduction

1070 HAWC's current software suite, plugins to 3ML, does not fully utilize computational advancements of recent decades. Said advancements include the proliferation of Graphical Processing
1071 Units (GPUs), and multithreading on multi-core processors. The analysis described in chapter 6
1072 took up to 3 months of human time waiting for the full gambit of data analysis and simulation
1073 of background to run. Additionally, with the addition of a 2D binning scheme, f_{hit} and NN, the
1074 compute time is expected to grow. Although excessive computing time was, in part, from an intense
1075 use of a shared computing cluster, it was evident that there was room for improvement. In HAWC's
1076 next generation dSph DM search, I decided to develop codes that would utilize the multi-core
1077 processors on modern high performance computing clusters. The results of this work are featured
1078 in this chapter and brought a human timing improvement to computation that scales as $1/N$ where
1079 N is the number of threads.

1081 7.2 Dataset and Background

1082 This section enumerates the data and background methods used for HAWC's multi-threaded
1083 study of dSphs. Section 7.2.1 and Section 7.2.2 are most useful for fellow HAWC collaborators
1084 looking to replicate a multithreaded dSph DM search.

1085 7.2.1 Itemized HAWC files

- 1086 • Detector Resolution: `refit-Pass5-Final-NN-detRes-zenith-dependent.root`
- 1087 • Data Map: `Pass5-Final-NN-maptree-ch103-ch1349-zenith-dependent.root`
- 1088 • Spectral Dictionary: `HDMspectra_dict_gamma.npy`

1089 7.2.2 Software Tools and Development

1090 This analysis was performed using HAL and 3ML [42, 43] in Python version 3. I built software
1091 in collaboration with Michael Martin and Letrell Harris to implement the *Dark Matter Spectra from*

1092 *the Electroweak to the Planck Scale* (HDM) [64] and dSphs spatial model from [65] for HAWC
1093 analysis. A NumPy dictionary of HDM was made for Py3. The corresponding Python3 file is
1094 `HDMspectra_dict_gamma.npy`. These files can also be used for decay channels and tools are
1095 provided in HDM’s [git repository](#) [64]. The analysis was performed using the Neural Network
1096 energy estimator for Pass 5.F. A description of this estimator was provided in chapter 4. **TODO:**
1097 **define a subsection when it’s written** All other software used for data analysis, DM profile generation,
1098 and job submission to SLURM are also kept in my sandbox in the [Dark Matter HAWC](#) project.
1099 The above repository also incorporates the model inputs used previously in Glory Duck, described
1100 in chapter 6

1101 7.2.3 Data Set and Background Description

1102 The HAWC data maps used for this analysis contain 2565 days of data between runs 2104 (

1103 **TODO: Day start**) and 7476 (**TODO: day end**). They were generated from pass 4.0 reconstruction.

1104 The analysis is performed using the NN energy estimator with bin list:

1105 B1C0Ea, B1C0Eb, B1C0Ec, B1C0Ed, B1C0Ee, B2C0Ea, B2C0Eb, B2C0Ec, B2C0Ed, B2C0Ee,
1106 B3C0Ea, B3C0Eb, B3C0Ec, B3C0Ed, B3C0Ee, B3C0Ef, B4C0Eb, B4C0Ec, B4C0Ed, B4C0Ee,
1107 B4C0Ef, B5C0Ec, B5C0Ed, B5C0Ee, B5C0Ef, B5C0Eg, B6C0Ed, B6C0Ee, B6C0Ef, B6C0Eg,
1108 B6C0Eh, B7C0Ee, B7C0Ef, B7C0Eg, B7C0Eh, B7C0Ei, B8C0Ee, B8C0Ef, B8C0Eg, B8C0Eh,
1109 B8C0Ei, B8C0Ej, B9C0Ef, B9C0Eg, B9C0Eh, B9C0Ei, B9C0Ej, B10C0Eg, B10C0Eh,
1110 B10C0Ei, B10C0Ej, B10C0Ek, B10C0El

1111 Bin 0 was excluded as it has substantial hadronic contamination and poor angular resolution.

1112 Background considerations and source selection was identical to Section 6.2, and no additional
1113 arguments are provided here. Many of the HAWC systematics explored in Section 6.7 also apply
1114 for this DM search and are not added upon here.

1115 7.3 Analysis

1116 The analysis and its systematics are almost identical to Section 6.3. Importantly, we use the
1117 same Equation (6.1) and Equation (6.2) for estimating the gamma-ray flux at HAWC from our

sources. We add on to the previous study with a search for DM decay. The flux equations for DM decay are

$$\frac{d\Phi_\gamma}{dE_\gamma} = \frac{1}{4\pi\tau m_\chi} \frac{dN_\gamma}{dE_\gamma} \times \int_{\text{source}} d\Omega \int_{l.o.s} dl \rho_\chi dl(r, \theta') \quad (7.1)$$

with a new quantity, the D factor, defined as

$$D = \int d\Omega \int_{l.o.s} dl \rho_\chi(r, \theta') \quad (7.2)$$

Software was written to accomodate DM decay from dSphs, however decay profiles were not received from $\mathcal{L}\mathcal{S}$ by the time of writing this tehsis.

7.3.1 $\frac{dN_\gamma}{dE_\gamma}$ - Particle Physics Component

For these spectra, we import HDM with Electroweak (EW) corrections and additional corrections for neutrinos above the EW scale [64]. The spectrum is implemented as a model script in astromodels for 3ML. A comprehensive description of EW corrections and neutrino considerations are provided later in [TODO: refeance MM nu duck](#).

Figure 7.1 demonstrates the impact of changes from HDM on DM annihilation to W bosons. A class in astromodels was developed to include HDM and is aptly named `HDMspectra` within `DM_models.py`. The SM DM annihilation channels studied here are $\chi\chi \rightarrow:$

$$e^+e^-, \mu^+\mu^-, \tau^+\tau^-, b\bar{b}, t\bar{t}, gg, W^+W^-, ZZ, c\bar{c}, u\bar{u}, d\bar{d}, s\bar{s}, \nu_e\bar{\nu}_e, \nu_\mu\bar{\nu}_\mu, \nu_\tau\bar{\nu}_\tau, \gamma\gamma, hh.$$

For $\gamma\gamma$ and ZZ , a substantial fraction of the signal photons are expected to have total energy equal m_χ [64]. This introduces a δ -function that is much narrower than the energy resolution of the HAWC detector. To ensure that this feature is not lost in the likelihood fits, the 'line' feature is convolved with a gaussian kernel with a 1σ width of $0.05 \cdot m_\chi$ and total kernel window of $\pm 4\sigma$. This differs from HAWC's previous line study where 30% of HAWC's energy resolution was used for the kernel [66]. The NN energy estimator's strength compared to f_{hit} at low gamma-ray energy enables smaller resolutions in addition to low energy tails in the spectral models [64]. $\chi\chi \rightarrow \gamma\gamma$ and ZZ spectral hypotheses are shown in Figure 7.2. Spectral models for the remaining annihilation channels are plotted for each m_χ in Figure B.1.

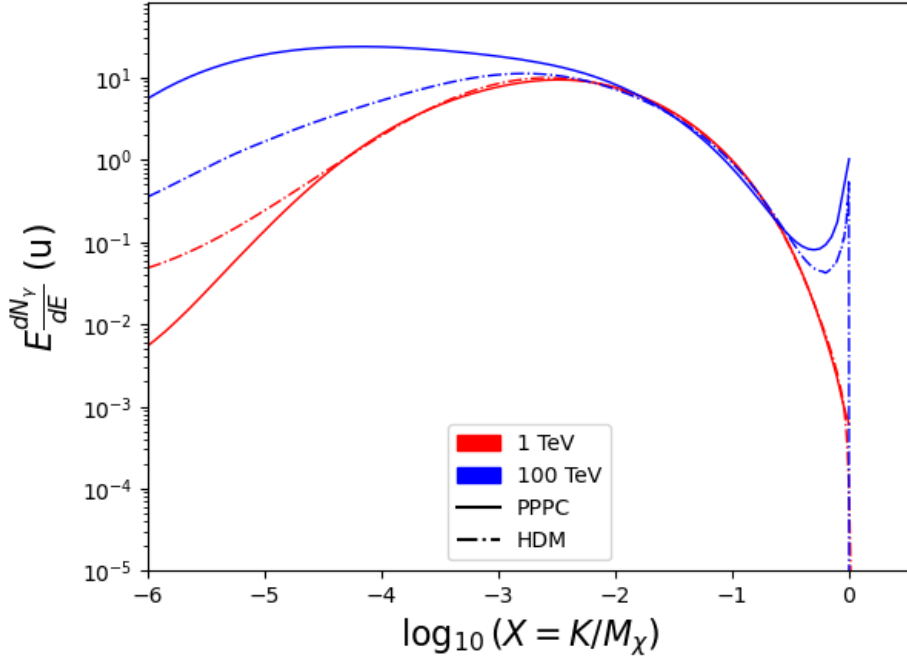


Figure 7.1 Difference between spectral hypotheses from PPPC [44] and HDM [64]. Shown is the expected DM annihilation spectrum for $\chi\chi \rightarrow W^-W^+$. Solid lines are spectral models with EW corrections from the PPPC. Dash-dot lines are spectral models from HDM. Red lines are models for $M_\chi = 1$ TeV. Blue lines represent models for $M_\chi = 100$ TeV.

1141 7.3.2 *J* and *D*- Astrophysical Components

1142 The J-factor profiles for each source are imported from Louis Strigari et al. (referred to with
 1143 \mathcal{LS}) [65]. Profiles in $\frac{dJ}{d\Omega}(\theta)$ up to $\theta = 0.5^\circ$ were provided directly from the authors. Map generation
 1144 from these profiles were almost identical to Section 6.3.2 except that a higher order trapezoidal
 1145 integral was used for the normalization of the square, uniformly-spaced map:

$$p^2 \cdot \sum_{i=0}^N \sum_{j=0}^M w_{i,j} \frac{d\mathcal{K}}{d\Omega}(\theta_{i,j}, \phi_{i,j}) \quad (7.3)$$

1146 \mathcal{K} is either *J* or *D* for the spatial distributions of annihilation or decay respectively. *p* is the angular
 1147 side of one pixel in the map. $w_{i,j}$ is a weight assigned the following ways:

1148 $w_{i,j} = 1$ if $(\theta_{i,j}, \phi_{i,j})$ is fully within the region of integration

1149 $w_{i,j} = 1/2$ if $(\theta_{i,j}, \phi_{i,j})$ is on an edge of the region of integration

1150 $w_{i,j} = 1/4$ if $(\theta_{i,j}, \phi_{i,j})$ is on a corner of the region of integration

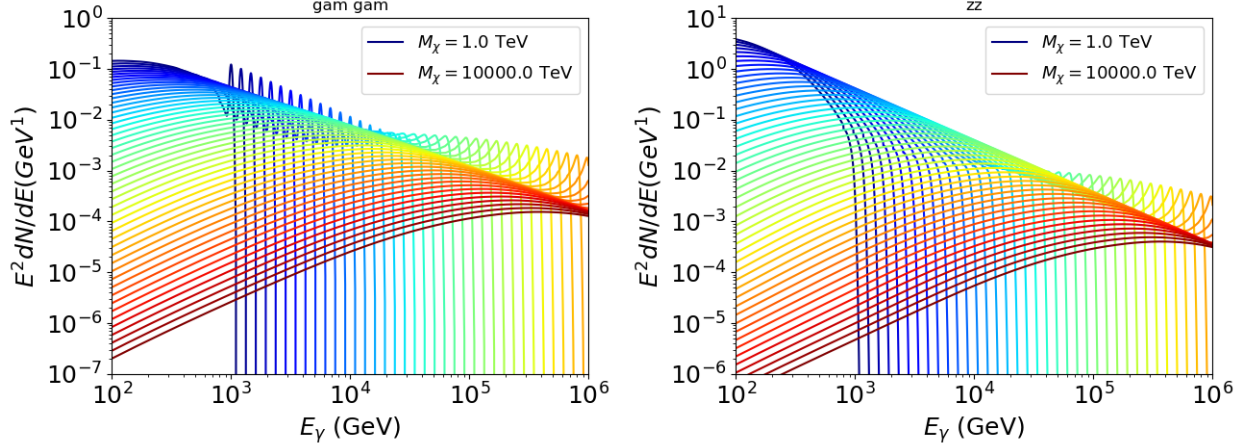


Figure 7.2 Photon spectra for $\chi\chi \rightarrow \gamma\gamma$ (left) and $\chi\chi \rightarrow ZZ$ (right) after gaussian convolution of line features. Both spectra have δ -features at photon energies equal to the DM mass. Bluer lines are annihilation spectra with lower DM mass. Redder lines are spectra from larger DM mass. All Spectral models are sourced from the Heavy Dark Matter models [64]. Axes are drawn roughly according to the energy sensitivity of HAWC.

1151 Figure 7.3 shows the median and $\pm 1\sigma$ maps used as input for DM annihilation studied by \mathcal{LS} .

1152 7.3.3 Source Selection and Annihilation Channels

1153 HAWC's sources for this multithreaded analysis include Coma Berenices, Draco, Segue 1, and
 1154 Sextans. \mathcal{LS} observes up to 43 sources in its publication, however only 4 of the best fit profiles were
 1155 provided at the time this thesis was written. A full description of each source used in this analysis
 1156 is found in Table 7.1.

1157 This analysis improves on chapter 6 in the following ways. Previously, the particle physics

Name	Distance (kpc)	l, b ($^\circ$)	$\log_{10} J$ (\mathcal{LS} set) $\log_{10}(\text{GeV}^2 \text{cm}^{-5} \text{sr})$
Coma Berenices	44	241.89, 83.61	$19.00^{+0.36}_{-0.35}$
Draco	76	86.37, 34.72	$18.83^{+0.12}_{-0.12}$
Segue I	23	220.48, 50.43	$19.12^{+0.49}_{-0.58}$
Sextans	86	243.50, 42.27	$17.73^{+0.13}_{-0.12}$

Table 7.1 Summary of the relevant properties of the dSphs used in the present work. Column 1 lists the dSphs. Columns 2 and 3 present their heliocentric distance and galactic coordinates, respectively. Column 4 reports the J -factors of each source given from the \mathcal{LS} studies and estimated $\pm 1\sigma$ uncertainties. The values $\log_{10} J$ (\mathcal{LS} set) [65] correspond to the mean J -factor values for a source extension truncated at 0.5° .

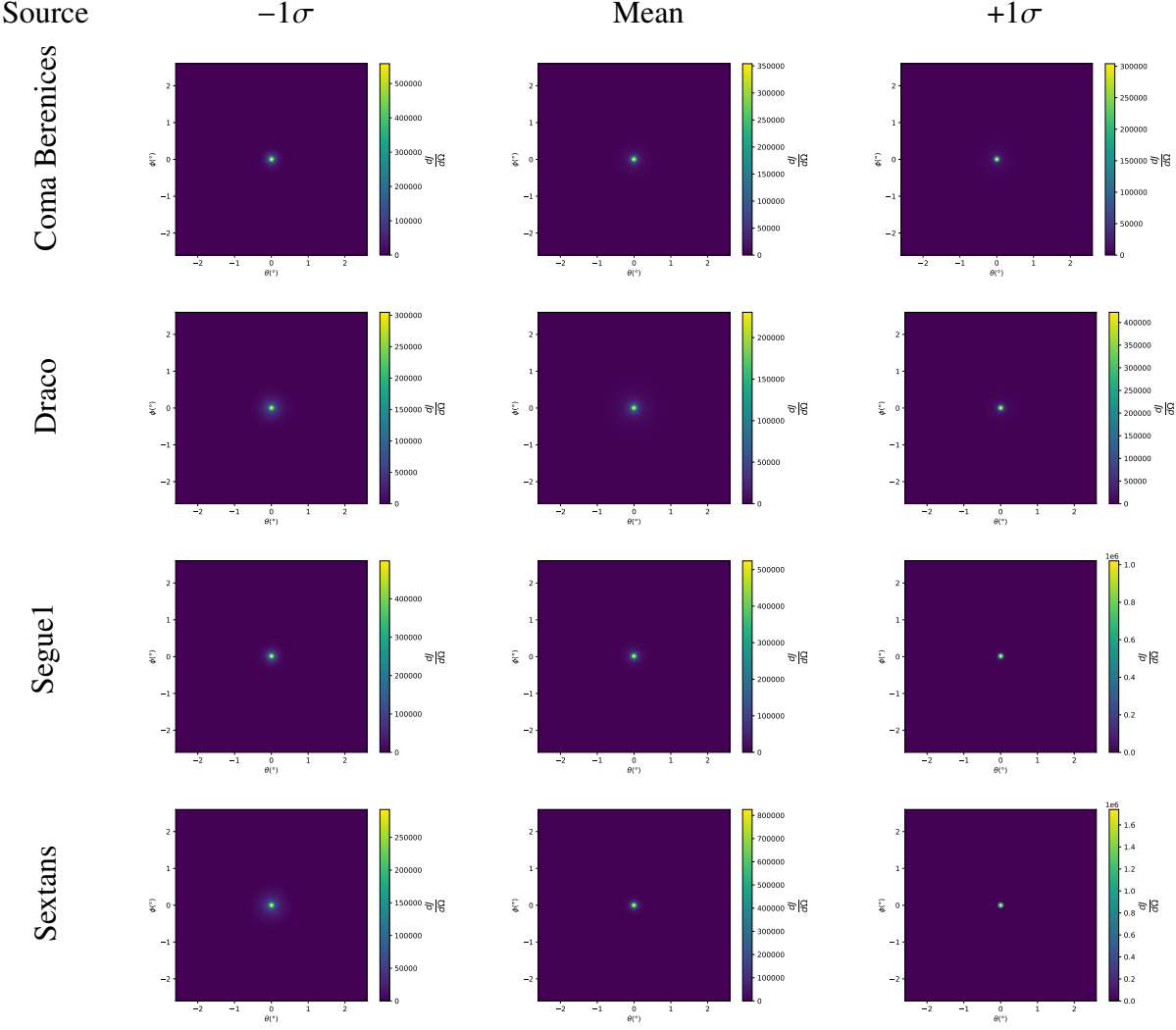


Figure 7.3 $\frac{dJ}{d\Omega}$ maps for Coma Berenices, Draco, Segue1, and Sextans. Columns are divided for the $\pm 1\sigma$ uncertainties in $dJ/d\Omega$ around the mean value from \mathcal{LS} [65]. Origin is centered on the specific dwarf spheroidal galaxies (dSph). θ and ϕ axes are the angular separation from the center of the dwarf

model used for gamma-ray spectra from DM annihilation was from the PPPC [44] which missed important considerations relevant for the neutrino sector. HDM is used to account for this shortfall [64]. HDM also models DM to the Planck scale which permits HAWC to probe PeV scale DM. For this study, we sample DM masses: 1 TeV - 10 PeV with 6 mass bins per decade in DM mass. In the case of line spectra ($\chi\chi \rightarrow \gamma\gamma$, or ZZ), we double the mass binning to 12 DM mass bins per decade in DM mass. A larger source catalog is used that uses a Navarro–Frenk–White (NFW) spatial DM distribution from \mathcal{LS} [65]. Because NFW has fewer parameters than what is used

1165 for \mathcal{GS} , \mathcal{LS} is able to fit ultra-faint dwarves, expanding the number of sources available for DM
1166 searches. Finally, the gamma-ray ray dataset is much larger. The study performed here analyzes
1167 2565 days of data compared to 1017 days analyzed in chapter 6.

1168 **7.4 Likelihood Methods**

1169 These are identical to Section 6.4.1 and no additional changes are made to the likelihood. Bins
1170 in this analysis are expanded to include HAWC’s NN energy estimator.

1171 **7.5 Computational Methods: Multithreading**

1172 Previously, as in Section 6.3, the likelihood was minimized for one model at a time. One
1173 model in this case representing a DM annihilation channel, DM mass, and dSph. In an effort
1174 to conserve human and CPU time, jobs submitted for high performance computing contained a
1175 list of DM masses to iterate over for likelihood fitting. Jobs were then trivially parallelized for
1176 each permutation of the two lists: CHANS (SM annihilation channel) and SOURCES (dSph spatial
1177 templates). The lists for CHANS and SOURCES are found in Section 7.3.1 and Table 7.1, respectively.
1178 Initially, 11 DM mass bins were serially sampled for one job defined by a [SM channel, dSph] set.
1179 Computing the likelihoods would take between 1.5 to 2 hrs, stocastically, for a job. We expect to
1180 compute likelihoods for data and 300 Poisson background trials. The estimated CPU time based on
1181 the above for all SM annihilation channels (17) and 25 sources (all \mathcal{LS} sources withing HAWC’s
1182 field of view) amounted to 127,925 jobs. In total, 1,407,175 likelihood fits and profiles would be
1183 computed for the 11 mass bins we wished to study. The estimated CPU time ranged between 10k
1184 CPU days - 8k CPU days. Human time is more challenging to estimate as job allocation is stochastic
1185 and highly dependant on what other users are submitting, yet it is unlikely that all jobs would run
1186 simultaneously. Therefore we can expect human time to be about as long as was seen in chapter 6
1187 which was on the order of months to fully compute on a smaller analysis. A visual aid to describe
1188 how jobs were organized is provided in Figure 7.4.

1189 The computational needs for this next generation DM analysis are extreme and is unlike other
1190 analyses performed on HAWC. It became clear that there was a lot to gain from optimzing how the
1191 likelihoods are computed. This section discusses how multi-threading was applied to solved and

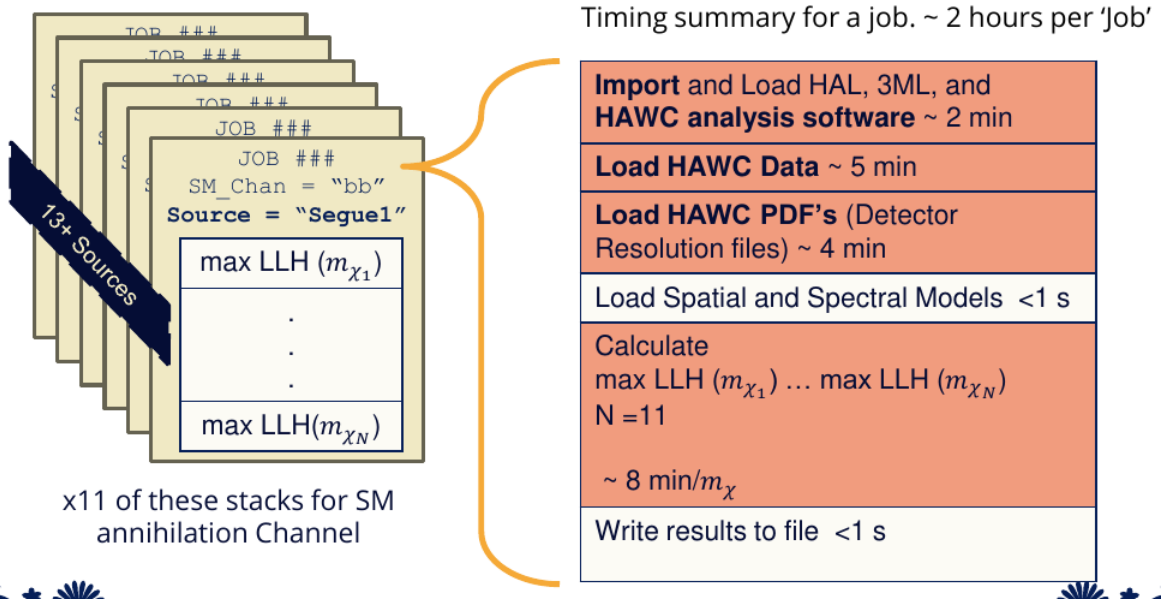


Figure 7.4 Infographic on how jobs and DM computation was organized in Section 6.3. Jobs were built for each permutation of CHANS and SOURCES shown by the left block in the figure. Each job, which took on the order 2 hrs to compute, had the following work flow: 1. Import HAWC analysis software, 2 min to run. 2. Load HAWC count maps, 5 min to run. 3. Load HAWC energy and spatial resolutions, 4 min. 5. Load DM spatial source templates and spectral models, less than 1 s. 6. Perform likelihood fit on data and model, about 8 min per DM mass. 7. Write results to file, less than 1s.

1192 reduce HAWC's computing of likelihoods for large parameter spaces like in DM searches.

CHAPTER 8

1193 **HEAVY DARK MATTER ANNIHILATION SEARCH WITH ICECUBE'S NORTH SKY**
1194 **TRACK DATA**

CHAPTER 9

NU DUCK

1195

MULTI-EXPERIMENT SUPPLEMENTARY FIGURES

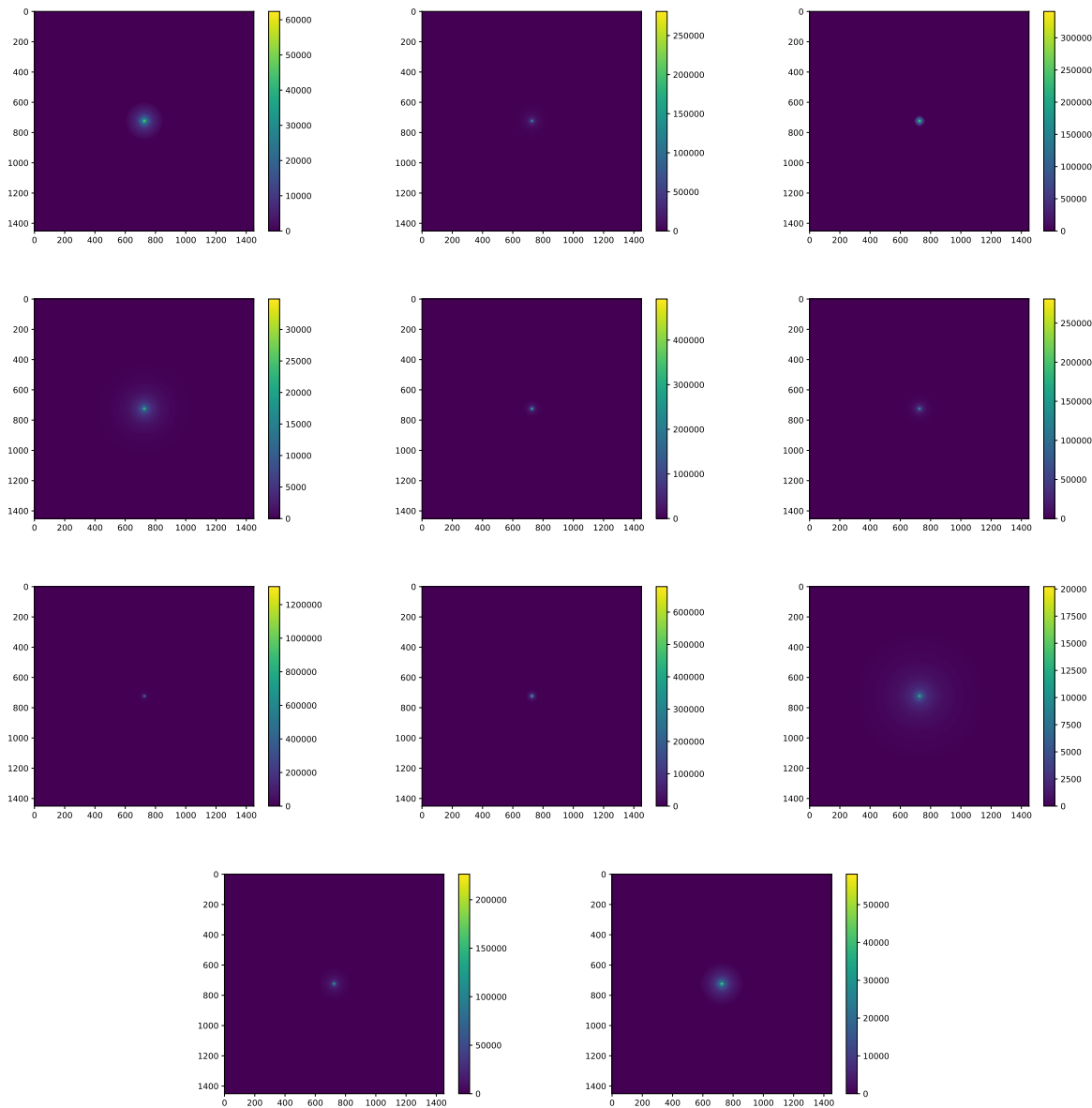


Figure A.1 Sister figure to Figure 6.3. Sources in the first row from left to right: Bootes I, Canes Venatici I, II. In second row: Draco, Hercules, Leo I. In the first row: Leo II, Leo IV, Sextans. In the final row: Ursa Major I, Ursa Major II.

APPENDIX B

MULTITHREADING SUPPLEMENTARY FIGURES

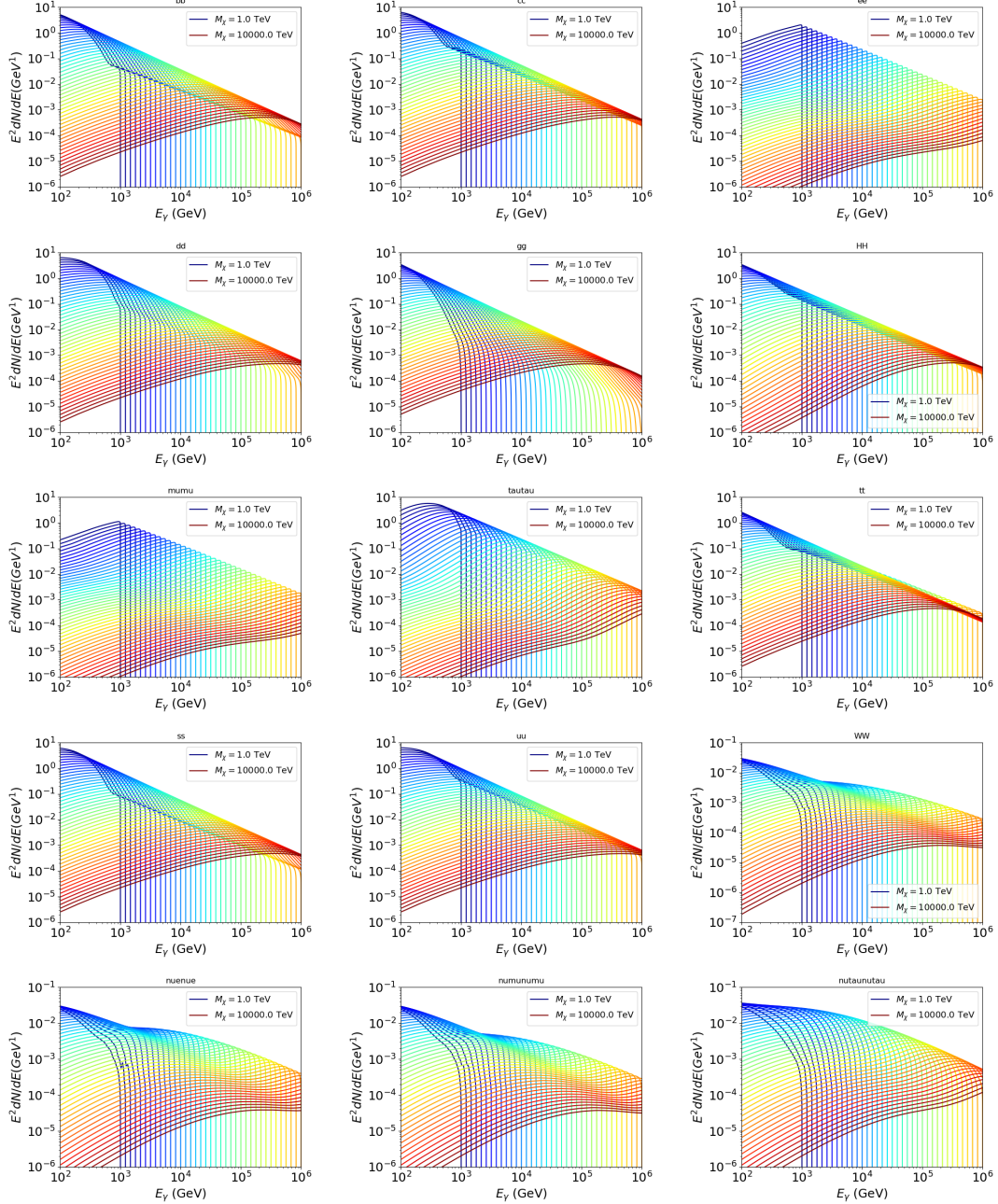


Figure B.1 Sister figure to Figure 7.2 for remaining SM primary annihilation channels studied for this thesis. These did not require any post generation smoothing and so are directly pulled from [64] with a binning scheme most helpful for a HAWC analysis.

BIBLIOGRAPHY

- [1] Anne M. Green. “Dark matter in astrophysics/cosmology”. In: *SciPost Phys. Lect. Notes* (2022), p. 37. doi: [10.21468/SciPostPhysLectNotes.37](https://doi.org/10.21468/SciPostPhysLectNotes.37). URL: <https://scipost.org/10.21468/SciPostPhysLectNotes.37>.
- [2] Bing-Lin Young. “A survey of dark matter and related topics in cosmology”. In: *Frontiers of Physics* 12 (Oct. 2016). doi: <https://doi.org/10.1007/s11467-016-0583-4>. URL: <https://doi.org/10.1007/s11467-016-0583-4>.
- [3] Gianfranco Bertone, Dan Hooper, and Joseph Silk. “Particle dark matter: evidence, candidates and constraints”. In: *Physics Reports* 405.5 (2005), pp. 279–390. issn: 0370-1573. doi: <https://doi.org/10.1016/j.physrep.2004.08.031>. URL: <https://www.sciencedirect.com/science/article/pii/S0370157304003515>.
- [4] Gianfranco Bertone and Dan Hooper. “History of dark matter”. In: *Rev. Mod. Phys.* 90 (4 Aug. 2018), p. 045002. doi: [10.1103/RevModPhys.90.045002](https://doi.org/10.1103/RevModPhys.90.045002). URL: <https://link.aps.org/doi/10.1103/RevModPhys.90.045002>.
- [5] Fritz Zwicky. “The Redshift of Extragalactic Nebulae”. In: *Helvetica Physica Acta* 6. (1933), pp. 110–127. doi: [10.5169/seals-110267](https://doi.org/10.5169/seals-110267).
- [6] Vera C. Rubin and Jr. Ford W. Kent. “Rotation of the Andromeda Nebula from a Spectroscopic Survey of Emission Regions”. In: *ApJ* 159 (Feb. 1970), p. 379. doi: [10.1086/150317](https://doi.org/10.1086/150317).
- [7] K. G. Begeman, A. H. Broeils, and R. H. Sanders. “Extended rotation curves of spiral galaxies: dark haloes and modified dynamics”. In: *Monthly Notices of the Royal Astronomical Society* 249.3 (Apr. 1991), pp. 523–537. issn: 0035-8711. doi: [10.1093/mnras/249.3.523](https://doi.org/10.1093/mnras/249.3.523). eprint: <https://academic.oup.com/mnras/article-pdf/249/3/523/18160929/mnras249-0523.pdf>. URL: <https://doi.org/10.1093/mnras/249.3.523>.
- [8] *Different types of gravitational lenses*. website. Feb. 2004. URL: <https://esahubble.org/images/heic0404b/>.
- [9] Douglas Clowe et al. “A Direct Empirical Proof of the Existence of Dark Matter”. In: *apjl* 648.2 (Sept. 2006), pp. L109–L113. doi: [10.1086/508162](https://doi.org/10.1086/508162). arXiv: [astro-ph/0608407 \[astro-ph\]](https://arxiv.org/abs/astro-ph/0608407).
- [10] Planck Collaboration and N. et. al. Aghanim. “Planck 2018 results I. Overview and the cosmological legacy of Planck”. In: *A&A* 641 (2020). doi: [10.1051/0004-6361/201833880](https://doi.org/10.1051/0004-6361/201833880). URL: <https://doi.org/10.1051/0004-6361/201833880>.
- [11] Wayne Hu. *Matter Density Animation*. web. 2024. URL: <http://background.uchicago.edu/~whu/animbut/anim2.html>.

- 1232 [12] Wenlong Yuan et al. “A First Look at Cepheids in a Type Ia Supernova Host with JWST”. in:
1233 *The Astrophysical Journal Letters* 940.1 (Nov. 2022). doi: [10.3847/2041-8213/ac9b27](https://doi.org/10.3847/2041-8213/ac9b27).
1234 URL: <https://dx.doi.org/10.3847/2041-8213/ac9b27>.
- 1235 [13] Wendy L. Freedman. “Measurements of the Hubble Constant: Tensions in Perspective”. In:
1236 *The Astrophysical Journal* 919.1 (Sept. 2021), p. 16. doi: [10.3847/1538-4357/ac0e95](https://doi.org/10.3847/1538-4357/ac0e95).
1237 URL: <https://dx.doi.org/10.3847/1538-4357/ac0e95>.
- 1238 [14] Jodi Cooley. “Dark Matter direct detection of classical WIMPs”. In: *SciPost Phys. Lect.
1239 Notes* (2022), p. 55. doi: [10.21468/SciPostPhysLectNotes.55](https://doi.org/10.21468/SciPostPhysLectNotes.55). URL: <https://scipost.org/10.21468/SciPostPhysLectNotes.55>.
1240
- 1241 [15] “Search for new phenomena in events with an energetic jet and missing transverse momentum
1242 in pp collisions at $\sqrt{s} = 13$ TeV with the ATLAS detector”. In: *Phys. Rev. D* 103
1243 (11 July 2021), p. 112006. doi: [10.1103/PhysRevD.103.112006](https://doi.org/10.1103/PhysRevD.103.112006). URL: <https://link.aps.org/doi/10.1103/PhysRevD.103.112006>.
1244
- 1245 [16] *Jetting into the dark side: a precision search for dark matter*. website. July 2020. URL:
1246 <https://atlas.cern/updates/briefing/precision-search-dark-matter>.
- 1247 [17] Celine Armand et. al. “Combined dark matter searches towards dwarf spheroidal galaxies
1248 with Fermi-LAT, HAWC, H.E.S.S., MAGIC, and VERITAS”. in: *Proceedings of Science*.
1249 Vol. 395. Mar. 2022. doi: <https://doi.org/10.22323/1.395.0528>.
- 1250 [18] Tracy R. Slatyer. “Les Houches Lectures on Indirect Detection of Dark Matter”. In: *SciPost
1251 Phys. Lect. Notes* (2022), p. 53. doi: [10.21468/SciPostPhysLectNotes.53](https://doi.org/10.21468/SciPostPhysLectNotes.53). URL:
1252 <https://scipost.org/10.21468/SciPostPhysLectNotes.53>.
- 1253 [19] Christian W Bauer, Nicholas L. Rodd, and Bryan R. Webber. “Dark matter spectra from
1254 the electroweak to the Planck scale”. In: *Journal of High Energy Physics* 2021.1029-8479
1255 (June 2021). doi: [https://doi.org/10.1007/JHEP06\(2021\)121](https://doi.org/10.1007/JHEP06(2021)121).
- 1256 [20] Riccardo Catena and Piero Ullio. “A novel determination of the local dark matter density”.
1257 In: *Journal of Cosmology and Astroparticle Physics* 2010.08 (Aug. 2010), p. 004. doi:
1258 [10.1088/1475-7516/2010/08/004](https://doi.org/10.1088/1475-7516/2010/08/004). URL: <https://dx.doi.org/10.1088/1475-7516/2010/08/004>.
1259
- 1260 [21] B. P. Abbott et al. “Observation of Gravitational Waves from a Binary Black Hole Merger”.
1261 In: *Phys. Rev. Lett.* 116 (6 Feb. 2016), p. 061102. doi: [10.1103/PhysRevLett.116.061102](https://doi.org/10.1103/PhysRevLett.116.061102). URL: <https://link.aps.org/doi/10.1103/PhysRevLett.116.061102>.
1262
- 1263 [22] R. Abbasi et. al. “Observation of high-energy neutrinos from the Galactic plane”. In: *Science*
1264 380.6652 (June 2023), pp. 1338–1343.
- 1265 [23] NASA Goddard Space Flight Center. *Fermi’s 12-year view of the gamma-ray sky*. website.

- 1266 2022. URL: <https://svs.gsfc.nasa.gov/14090>.
- 1267 [24] Marco Cirelli et al. “PPPC 4 DM ID: a poor particle physicist cookbook for dark matter
1268 indirect detection”. In: *Journal of Cosmology and Astroparticle Physics* 2011.03 (Mar.
1269 2011), p. 051. doi: [10.1088/1475-7516/2011/03/051](https://doi.org/10.1088/1475-7516/2011/03/051). URL: <https://dx.doi.org/10.1088/1475-7516/2011/03/051>.
- 1270
- 1271 [25] Javier Rico. “Gamma-Ray Dark Matter Searches in Milky Way Satellites—A Comparative
1272 Review of Data Analysis Methods and Current Results”. In: *Galaxies* 8.1 (Mar. 2020), p. 25.
1273 doi: [10.3390/galaxies8010025](https://doi.org/10.3390/galaxies8010025). arXiv: [2003.13482](https://arxiv.org/abs/2003.13482) [astro-ph.HE].
- 1274 [26] W. B. Atwood et al. “The Large Area Telescope on the Fermi Gamma-Ray Space Telescope
1275 Mission”. In: *apj* 697.2 (June 2009), pp. 1071–1102. doi: [10.1088/0004-637X/697/2/1071](https://doi.org/10.1088/0004-637X/697/2/1071). arXiv: [0902.1089](https://arxiv.org/abs/0902.1089) [astro-ph.IM].
- 1276
- 1277 [27] M. Ackermann et al. “Searching for Dark Matter Annihilation from Milky Way Dwarf
1278 Spheroidal Galaxies with Six Years of Fermi Large Area Telescope Data”. In: *prl* 115.23,
1279 231301 (Dec. 2015), p. 231301. doi: [10.1103/PhysRevLett.115.231301](https://doi.org/10.1103/PhysRevLett.115.231301). arXiv:
1280 [1503.02641](https://arxiv.org/abs/1503.02641) [astro-ph.HE].
- 1281 [28] Mattia Di Mauro, Martin Stref, and Francesca Calore. “Investigating the effect of Milky
1282 Way dwarf spheroidal galaxies extension on dark matter searches with Fermi-LAT data”.
1283 In: *Phys. Rev. D* 106 (12 Dec. 2022), p. 123032. doi: [10.1103/PhysRevD.106.123032](https://doi.org/10.1103/PhysRevD.106.123032).
1284 URL: <https://link.aps.org/doi/10.1103/PhysRevD.106.123032>.
- 1285 [29] F. et al. Aharonian. “Observations of the Crab Nebula with H.E.S.S.”. In: *Astron. Astrophys.*
1286 457 (2006), pp. 899–915. doi: [10.1051/0004-6361:20065351](https://doi.org/10.1051/0004-6361:20065351). arXiv: [astro-ph/0607333](https://arxiv.org/abs/astro-ph/0607333).
- 1287
- 1288 [30] J. Albert et al. “VHE γ -Ray Observation of the Crab Nebula and its Pulsar with the MAGIC
1289 Telescope”. In: *The Astrophysical Journal* 674.2 (Feb. 2008), p. 1037. doi: [10.1086/525270](https://doi.org/10.1086/525270). URL: <https://dx.doi.org/10.1086/525270>.
- 1289
- 1290
- 1291 [31] N. Park. “Performance of the VERITAS experiment”. In: *Proceedings, 34th International
1292 Cosmic Ray Conference (ICRC2015): The Hague, The Netherlands, July, 30th July - 6th
1293 August*. Vol. 34. 2015, p. 771. arXiv: [1508.07070](https://arxiv.org/abs/1508.07070) [astro-ph.IM].
- 1294
- 1295 [32] A. Abramowski et al. “H.E.S.S. constraints on Dark Matter annihilations towards the Sculptor
1296 and Carina Dwarf Galaxies”. In: *Astropart. Phys.* 34 (2011), pp. 608–616. doi: [10.1016/j.astropartphys.2010.12.006](https://doi.org/10.1016/j.astropartphys.2010.12.006). arXiv: [1012.5602](https://arxiv.org/abs/1012.5602) [astro-ph.HE].
- 1296
- 1297 [33] A. Abramowski et al. “Search for dark matter annihilation signatures in H.E.S.S. observations
1298 of Dwarf Spheroidal Galaxies”. In: *Phys. Rev. D* 90 (2014), p. 112012. doi: [10.1103/PhysRevD.90.112012](https://doi.org/10.1103/PhysRevD.90.112012). arXiv: [1410.2589](https://arxiv.org/abs/1410.2589) [astro-ph.HE].
- 1299

- 1300 [34] H. Abdalla et al. “Searches for gamma-ray lines and ‘pure WIMP’ spectra from Dark
1301 Matter annihilations in dwarf galaxies with H.E.S.S”. in: *JCAP* 11 (2018), p. 037. doi:
1302 [10.1088/1475-7516/2018/11/037](https://doi.org/10.1088/1475-7516/2018/11/037). arXiv: [1810.00995 \[astro-ph.HE\]](https://arxiv.org/abs/1810.00995).
- 1303 [35] J. Aleksić et al. “Optimized dark matter searches in deep observations of Segue 1 with
1304 MAGIC”. in: *JCAP* 1402 (2014), p. 008. doi: [10.1088/1475-7516/2014/02/008](https://doi.org/10.1088/1475-7516/2014/02/008).
1305 arXiv: [1312.1535 \[hep-ph\]](https://arxiv.org/abs/1312.1535).
- 1306 [36] V.A. Acciari et al. “Combined searches for dark matter in dwarf spheroidal galaxies observed
1307 with the MAGIC telescopes, including new data from Coma Berenices and Draco”. In: *Physics of the Dark Universe* (2021), p. 100912. issn: 2212-6864. doi: <https://doi.org/10.1016/j.dark.2021.100912>. URL: <https://www.sciencedirect.com/science/article/pii/S2212686421001370>.
- 1311 [37] M. L. Ahnen et al. “Indirect dark matter searches in the dwarf satellite galaxy Ursa Major II
1312 with the MAGIC Telescopes”. In: *JCAP* 1803.03 (2018), p. 009. doi: [10.1088/1475-7516/2018/03/009](https://doi.org/10.1088/1475-7516/2018/03/009). arXiv: [1712.03095 \[astro-ph.HE\]](https://arxiv.org/abs/1712.03095).
- 1314 [38] S. et al. Archambault. “Dark matter constraints from a joint analysis of dwarf Spheroidal
1315 galaxy observations with VERITAS”. in: *prd* 95.8 (Apr. 2017). doi: [10.1103/PhysRevD.95.082001](https://doi.org/10.1103/PhysRevD.95.082001). arXiv: [1703.04937 \[astro-ph.HE\]](https://arxiv.org/abs/1703.04937).
- 1317 [39] Louise Oakes et al. “Combined Dark Matter searches towards dwarf spheroidal galaxies with
1318 Fermi-LAT, HAWC, HESS, MAGIC and VERITAS”. in: *Proceedings of Science*. 2019.
- 1319 [40] Celine Armand et al. on behalf of the Fermi-LAT, HAWC, HESS, MAGIC, VERITAS.
1320 “Combined Dark Matter searches towards dwarf spheroidal galaxies with Fermi-LAT,
1321 HAWC, HESS, MAGIC and VERITAS”. in: *Proceedings of Science*. 2021.
- 1322 [41] Daniel Kerszberg et al. on behalf of the Fermi-LAT, HAWC, HESS, MAGIC, and VER-
1323 TIAS collaborations. “Search for dark matter annihilation with a combined analysis of
1324 dwarf spheroidal galaxies from Fermi-LAT, HAWC, H.E.S.S., MAGIC and VERITAS”. in:
1325 *Proceedings of Science*. 2023.
- 1326 [42] A. U. Abeysekara et al. “Observation of the Crab Nebula with the HAWC Gamma-Ray
1327 Observatory”. In: *The Astrophysical Journal* 843.1 (June 2017), p. 39. doi: [10.3847/1538-4357/aa7555](https://doi.org/10.3847/1538-4357/aa7555). URL: <https://doi.org/10.3847/1538-4357/aa7555>.
- 1329 [43] Giacomo Vianello et al. *The Multi-Mission Maximum Likelihood framework (3ML)*. 2015.
1330 arXiv: [1507.08343 \[astro-ph.HE\]](https://arxiv.org/abs/1507.08343).
- 1331 [44] Marco Cirelli et al. “PPPC 4 DM ID: a poor particle physicist cookbook for dark matter
1332 indirect detection”. In: *Journal of Cosmology and Astroparticle Physics* 2011.03 (Mar.
1333 2011). issn: 1475-7516. doi: [10.1088/1475-7516/2011/03/051](https://doi.org/10.1088/1475-7516/2011/03/051). URL: <http://dx.doi.org/10.1088/1475-7516/2011/03/051>.

- 1335 [45] Alex Geringer-Sameth, Savvas M. Koushiappas, and Matthew Walker. “DWARF GALAXY
 1336 ANNIHILATION AND DECAY EMISSION PROFILES FOR DARK MATTER EXPERI-
 1337 MENTS”. in: *The Astrophysical Journal* 801.2 (Mar. 2015), p. 74. ISSN: 1538-4357. doi:
 1338 [10.1088/0004-637X/801/2/74](https://doi.org/10.1088/0004-637X/801/2/74). URL: <http://dx.doi.org/10.1088/0004-637X/801/2/74>.
- 1340 [46] A. Albert et al. “Dark Matter Limits from Dwarf Spheroidal Galaxies with the HAWC
 1341 Gamma-Ray Observatory”. In: *The Astrophysical Journal* 853.2 (Feb. 2018), p. 154. ISSN:
 1342 1538-4357. doi: [10.3847/1538-4357/aaa6d8](https://doi.org/10.3847/1538-4357/aaa6d8). URL: <http://dx.doi.org/10.3847/1538-4357/aaa6d8>.
- 1344 [47] V. Bonnivard et al. “Spherical Jeans analysis for dark matter indirect detection in dwarf
 1345 spheroidal galaxies - Impact of physical parameters and triaxiality”. In: *Mon. Not. Roy.
 1346 Astron. Soc.* 446 (2015), pp. 3002–3021. doi: [10.1093/mnras/stu2296](https://doi.org/10.1093/mnras/stu2296). arXiv:
 1347 [1407.7822 \[astro-ph.HE\]](https://arxiv.org/abs/1407.7822).
- 1348 [48] M. Ackermann et al. “Searching for Dark Matter Annihilation from Milky Way Dwarf
 1349 Spheroidal Galaxies with Six Years of Fermi Large Area Telescope Data”. In: *prl* 115.23,
 1350 231301 (Dec. 2015), p. 231301. doi: [10.1103/PhysRevLett.115.231301](https://doi.org/10.1103/PhysRevLett.115.231301). arXiv:
 1351 [1503.02641 \[astro-ph.HE\]](https://arxiv.org/abs/1503.02641).
- 1352 [49] M. L. Ahnen et al. “Limits to Dark Matter Annihilation Cross-Section from a Combined
 1353 Analysis of MAGIC and Fermi-LAT Observations of Dwarf Satellite Galaxies”. In: *JCAP*
 1354 1602.02 (2016), p. 039. doi: [10.1088/1475-7516/2016/02/039](https://doi.org/10.1088/1475-7516/2016/02/039). arXiv: [1601.06590](https://arxiv.org/abs/1601.06590)
 1355 [astro-ph.HE].
- 1356 [50] Javier Rico et al. *gLike: numerical maximization of heterogeneous joint
 1357 likelihood functions of a common free parameter plus nuisance parameters*.
<https://doi.org/10.5281/zenodo.4601451>. Version v0.09.03. Mar. 2021. doi: [10.5281/zenodo.4601451](https://doi.org/10.5281/zenodo.4601451). URL: <https://doi.org/10.5281/zenodo.4601451>.
- 1360 [51] Tjark Miener and Daniel Nieto. *LklCom: Combining likelihoods from different experiments*.
<https://doi.org/10.5281/zenodo.4597500>. Version v0.5.3. Mar. 2021. doi: [10.5281/zenodo.4597500](https://doi.org/10.5281/zenodo.4597500). URL: <https://doi.org/10.5281/zenodo.4597500>.
- 1363 [52] T. Miener et al. “Open-source Analysis Tools for Multi-instrument Dark Matter Searches”.
 1364 In: *arXiv e-prints*, arXiv:2112.01818 (Dec. 2021), arXiv:2112.01818. arXiv: [2112.01818](https://arxiv.org/abs/2112.01818)
 1365 [astro-ph.IM].
- 1366 [53] Alex Geringer-Sameth and Matthew Koushiappas Savvas M. and Walker. “Dwarf galaxy
 1367 annihilation and decay emission profiles for dark matter experiments”. In: *Astrophys.
 1368 J.* 801.2 (2015), p. 74. doi: [10.1088/0004-637X/801/2/74](https://doi.org/10.1088/0004-637X/801/2/74). arXiv: [1408.0002](https://arxiv.org/abs/1408.0002)
 1369 [astro-ph.CO].
- 1370 [54] Gianfranco Bertone, Dan Hooper, and Joseph Silk. “Particle dark matter: evidence, can-

- 1371 didates and constraints”. In: *Physics Reports* 405.5-6 (Jan. 2005), pp. 279–390. ISSN:
1372 0370-1573. doi: [10.1016/j.physrep.2004.08.031](https://doi.org/10.1016/j.physrep.2004.08.031). URL: <http://dx.doi.org/10.1016/j.physrep.2004.08.031>.
- 1374 [55] V. Bonnivard et al. “Dark matter annihilation and decay in dwarf spheroidal galaxies: The
1375 classical and ultrafaint dSphs”. In: *Mon. Not. Roy. Astron. Soc.* 453.1 (2015), pp. 849–867.
1376 doi: [10.1093/mnras/stv1601](https://doi.org/10.1093/mnras/stv1601). arXiv: [1504.02048 \[astro-ph.HE\]](https://arxiv.org/abs/1504.02048).
- 1377 [56] A. et al. Albert. “Searching for Dark Matter Annihilation in Recently Discovered Milky Way
1378 Satellites with Fermi-LAT”. in: *Astrophys. J.* 834.2 (2017), p. 110. doi: [10.3847/1538-4357/834/2/110](https://doi.org/10.3847/1538-4357/834/2/110). arXiv: [1611.03184 \[astro-ph.HE\]](https://arxiv.org/abs/1611.03184).
- 1380 [57] Mattia Di Mauro and Martin Wolfgang Winkler. “Multimessenger constraints on the dark
1381 matter interpretation of the Fermi-LAT Galactic Center excess”. In: *prd* 103.12, 123005
1382 (June 2021), p. 123005. doi: [10.1103/PhysRevD.103.123005](https://doi.org/10.1103/PhysRevD.103.123005). arXiv: [2101.11027 \[astro-ph.HE\]](https://arxiv.org/abs/2101.11027).
- 1384 [58] HongSheng Zhao. “Analytical models for galactic nuclei”. In: *Mon. Not. Roy. Astron. Soc.*
1385 278 (1996), pp. 488–496. doi: [10.1093/mnras/278.2.488](https://doi.org/10.1093/mnras/278.2.488). arXiv: [astro-ph/9509122 \[astro-ph\]](https://arxiv.org/abs/astro-ph/9509122).
- 1387 [59] H. C. Plummer. “On the Problem of Distribution in Globular Star Clusters: (Plate 8.)”
1388 In: *Monthly Notices of the Royal Astronomical Society* 71.5 (Mar. 1911), pp. 460–470.
1389 ISSN: 0035-8711. doi: [10.1093/mnras/71.5.460](https://doi.org/10.1093/mnras/71.5.460). eprint: <https://academic.oup.com/mnras/article-pdf/71/5/460/2937497/mnras71-0460.pdf>. URL:
1391 <https://doi.org/10.1093/mnras/71.5.460>.
- 1392 [60] Daniel R. Hunter. “Derivation of the anisotropy profile, constraints on the local velocity
1393 dispersion, and implications for direct detection”. In: *JCAP* 02 (2014), p. 023. doi:
1394 [10.1088/1475-7516/2014/02/023](https://doi.org/10.1088/1475-7516/2014/02/023). arXiv: [1311.0256 \[astro-ph.CO\]](https://arxiv.org/abs/1311.0256).
- 1395 [61] Barun Kumar Dhar and Liliya L. R. Williams. “Surface mass density of the Einasto family
1396 of dark matter haloes: are they Sersic-like?” In: *Mon. Not. Roy. Astron. Soc.* (2010). doi:
1397 [10.1111/j.1365-2966.2010.16446.x](https://doi.org/10.1111/j.1365-2966.2010.16446.x).
- 1398 [62] M. Baes and E. Van Hese. “Dynamical models with a general anisotropy profile”. In:
1399 *Astron. Astrophys.* 471 (2007), p. 419. doi: [10.1051/0004-6361:20077672](https://doi.org/10.1051/0004-6361:20077672). arXiv:
1400 [0705.4109 \[astro-ph\]](https://arxiv.org/abs/0705.4109).
- 1401 [63] Matthew G. Walker, Edward W. Olszewski, and Mario Mateo. “Bayesian analysis of re-
1402 solved stellar spectra: application to MMT/Hectochelle observations of the Draco dwarf
1403 spheroidal”. In: *mnras* 448.3 (Apr. 2015), pp. 2717–2732. doi: [10.1093/mnras/stv099](https://doi.org/10.1093/mnras/stv099).
1404 arXiv: [1503.02589 \[astro-ph.GA\]](https://arxiv.org/abs/1503.02589).
- 1405 [64] Nicholas L. Rodd et al. “Dark matter spectra from the electroweak to the Planck scale”. In:

- 1406 *J. High Energy Physics* 121.10.1007 (June 2021).
- 1407 [65] Pace, Andrew B and Strigari, Louis E. “Scaling relations for dark matter annihilation and
1408 decay profiles in dwarf spheroidal galaxies”. In: *Monthly Notices of the Royal Astronomical
1409 Society* 482.3 (Oct. 2018), pp. 3480–3496. ISSN: 0035-8711. doi: [10.1093/mnras/sty2839](https://doi.org/10.1093/mnras/sty2839).
- 1411 [66] Albert, A. et al. “Search for gamma-ray spectral lines from dark matter annihilation in
1412 dwarf galaxies with the High-Altitude Water Cherenkov observatory”. In: *Phys. Rev. D* 101 (10 May 2020), p. 103001. doi: [10.1103/PhysRevD.101.103001](https://doi.org/10.1103/PhysRevD.101.103001). URL:
1413 <https://link.aps.org/doi/10.1103/PhysRevD.101.103001>.
1414